ISSN 2518-7198 (Print)
ISSN 2663-5089 (Online)

BULLETIN
OF THE KARAGANDA UNIVERSITY

PHYSICS
Series

2026 • Volume 31 • Issue 1(121)

ISSN 2663-5089 (Online)
ISSN-L 2518-7198 (Print)
Индексі 74616
Индекс 74616

ҚАРАҒАНДЫ УНИВЕРСИТЕТІНІҢ ХАБАРШЫСЫ

ВЕСТНИК КАРАГАНДИНСКОГО УНИВЕРСИТЕТА

BULLETIN OF THE KARAGANDA UNIVERSITY

ФИЗИКА сериясы

Серия ФИЗИКА

PHYSICS Series

2026

31-том • 1(121)-шығарылым
Том 31 • Выпуск 1(121)
Volume 31 • Issue 1(121)

1996 жылдан бастап шығады
Издается с 1996 года
Founded in 1996

Жылына 4 рет шығады
Выходит 4 раза в год
Published 4 times a year

Қарағанды / Караганда / Karaganda
2026

Баспагер: **«Академик Е.А. Бөкетов атындағы Қарағанды ұлттық зерттеу университеті» КеАҚ**

Мекенжайы: 100024, Қазақстан, Қарағанды қ., Университет к-сі, 28

E-mail: vestnikku@gmail.com; karabekova71@mail.ru. *Web-site*: https://phs.buketov.edu.kz

Қарағанды университетінің хабаршысы. «Физика» сериясы. — 2026. — 31-т., 1(121)-шығ. — 89 б. — ISSN-L 2518-7198 (Print). ISSN 2663-5089 (Online).

Меншік иесі: «Академик Е.А. Бөкетов атындағы Қарағанды ұлттық зерттеу университеті» КеАҚ.

Қазақстан Республикасы Мәдениет және ақпарат министрлігінде тіркелген. 05.12.2025 ж. № KZ56VPY00135985 қайта есепке қою туралы куәлігі.

Басуға 30.03.2026 ж. қол қойылды. Пішімі 60×84 1/8. Қағазы офсеттік. Көлемі 11,12 б.т. Таралымы 200 дана. Бағасы келісім бойынша. Тапсырыс № 19.

«Академик Е.А. Бөкетов атындағы Қарағанды ұлттық зерттеу университеті» КеАҚ баспасының баспаханасында басылып шықты.

100024, Қазақстан, Қарағанды қ., Университет к-сі, 28. Тел. (7212) 35-63-16.

E-mail: printed@karnu-buketov.edu.kz

Издатель: **НАО «Карагандинский национальный исследовательский университет имени академика Е.А. Букетова»**

Адрес: 100024, Казахстан, г. Караганда, ул. Университетская, 28
E-mail: vestnikku@gmail.com; karabekova71@mail.ru. *Web-site*: https://phs.buketov.edu.kz

Вестник Карагандинского университета. Серия «Физика». — 2026. — Т. 31, вып. 1(121). — 89 с. — ISSN-L 2518-7198 (Print). ISSN 2663-5089 (Online).

Собственник: НАО «Карагандинский национальный исследовательский университет имени академика Е.А. Букетова».

Зарегистрирован Министерством культуры и информации Республики Казахстан. Свидетельство о постановке на переучет № KZ56VPY00135985 от 05.12.2025 г.

Подписано в печать 30.03.2026 г. Формат 60×84 1/8. Бумага офсетная. Объем 11,12 п.л. Тираж 200 экз. Цена договорная. Заказ № 19.

Отпечатано в типографии издательства НАО «Карагандинский национальный исследовательский университет им. акад. Е.А. Букетова». 100024, Казахстан, г. Караганда, ул. Университетская, 28.
Тел. (7212) 35-63-16. E-mail: printed@karnu-buketov.edu.kz

Publisher: **NLC “Karaganda National Research University named after academician Ye.A. Buketov”**
Postal address: 28, Universitetskaya Str., Karaganda, 100024, Kazakhstan
E-mail: vestnikku@gmail.com; karabekova71@mail.ru. *Web-site*: https://phs.buketov.edu.kz

Bulletin of the Karaganda University. “Physics” Series. — 2026. — Vol. 31, Iss. 1(121). — 89 p. — ISSN-L 2518-7198 (Print). ISSN 2663-5089 (Online).

Proprietary: NLC “Karaganda National Research University named after academician Ye.A. Buketov”.

Registered by the Ministry of Culture and Information of the Republic of Kazakhstan. Rediscount certificate No. KZ56VPY00135985 dated 05.12.2025.

Signed in print 30.03.2026. Format 60×84 1/8. Offset paper. Volume 11,12 p.sh. Circulation 200 copies. Price upon request. Order № 19.

Printed in the Publishing house of NLC “Karaganda National Research University named after academician Ye.A. Buketov”. 28, University Str., Karaganda, 100024, Kazakhstan. Tel. (7212) 35-63-16.
E-mail: printed@karnu-buketov.edu.kz

МАЗМҰНЫ – СОДЕРЖАНИЕ – CONTENTS

КОНДЕНСАЦИЯЛАНҒАН КҮЙДІҢ ФИЗИКАСЫ
ФИЗИКА КОНДЕНСИРОВАННОГО СОСТОЯНИЯ
PHYSICS OF THE CONDENSED MATTER

ТЕХНИКАЛЫҚ ФИЗИКА
ТЕХНИЧЕСКАЯ ФИЗИКА
TECHNICAL PHYSICS

ЖЫЛУФИЗИКАСЫ ЖӘНЕ ТЕОРИЯЛЫҚ ЖЫЛУТЕХНИКАСЫ
ТЕПЛОФИЗИКА И ТЕОРЕТИЧЕСКАЯ ТЕПЛОТЕХНИКА
THERMOPHYSICS AND THEORETICAL THERMOENGINEERING

КОНДЕНСАЦИЯЛАНҒАН КҮЙДІҢ ФИЗИКАСЫ
ФИЗИКА КОНДЕНСИРОВАННОГО СОСТОЯНИЯ
PHYSICS OF THE CONDENSED MATTER

Article

UDC 621.785.6

https://doi.org/10.31489/2026PH1/6-12

Received: 26.11.2025
Accepted: 29.12.2025

Zh.B. Sagdoldina[1], L.G. Sulyubaeva[1], D.B. Buitkenov[1],
A.B. Nabioldina[1], S.D. Bolatov[1]✉, D.K. Sarzhanov[2]

[1]*Research Center Surface Engineering and Tribology,*
Sarsen Amanzholov East Kazakhstan University, Ust-Kamenogorsk, Kazakhstan;
[2]*Academy of Public Administration under the President of the Republic of Kazakstan, Astana, Kazakhstan*

The Effect of Detonation Spraying Mode on the Structure and Tribological Properties of WC–Co Coatings

The article presents the results of research into the structure and tribological testing of WC-Co detonation coatings with a barrel filling volume of 64 % and 74 %. X-ray diffraction analysis of the WC-Co coating revealed that undesirable Co and W_2C peaks disappear after detonation spraying. Morphological analysis showed that with 64 % and 74 % detonation barrel filling, the coatings had a dense structure with a thickness of 136 μm and 161 μm, respectively. EDS mapping showed a uniform distribution of elements. Tribological tests of the coating revealed that the friction coefficient of the samples ranged from 0.48 to 0.53 for 74 % and 0.55–0.57 for 64 %. Based on the results obtained, the optimal technological regime for obtaining wear-resistant WC-Co coatings by detonation spraying was established.

Keywords: detonation spraying, WC-Co coatings, tribology, coatings, microstructure.

✉*Corresponding author*: Bolatov, Sanzhar, sanzharbolatov94@gmail.com

Introduction

Nowadays WC–Co based coatings are widely used to improve wear resistance, as well as corrosion and erosion resistance of engineering components, including valves, drill bits and downhole tool components used in the mining, oil and gas industries [1]. Due to their excellent wear resistance and mechanical stability, WC–Co coatings are commonly used for steel rolls, zinc bath rolls, corrugated rolls, pump housings, impeller shafts, compressor stators, and aircraft flap guides. Additionally, these coatings find application in cams and expansion joints operating under severe service conditions [2].

It has been established that the wear resistance of WC–Co coatings is significantly affected by various factors, such as the morphology, chemical and phase composition of the initial powder, the size and distribution of WC particles, and spraying parameters [3-4]. During thermal spraying of WC–Co, undesirable phenomena associated with the decomposition of carbide phases can occur. As a result, the content of the solid WC phase decreases, and decomposition products such as W_2C, metallic W, and amorphous or nanocrystalline Co–WC phases are formed instead. Therefore, to obtain hard alloys with high mechanical properties, it is necessary to minimize the decomposition of the WC phase.

Despite the widespread use of WC–Co coatings, numerous studies have shown that thermal spraying results in decarburization of WC particles. As noted by Ahmed et al. in their review, high temperatures and prolonged exposure of particles to the flame zone lead to the formation of W_2C, metallic W, and η-phases (M_6C and $M_{12}C$). This complicates the coating microstructure and reduces its mechanical properties [5].

Detonation spraying represents a very promising direction in the field of thermal spray technology, offering a viable solution for the production of high-quality wear-resistant coatings. Research by Du et al. showed that even at high oxygen-fuel ratios, the degree of WC decarburization remains low, allowing for the production of coatings with high density and strength [6]. This contrasts with plasma spraying methods, where WC decomposition is significantly more pronounced.

Yuan et al. showed that the introduction of submicron WC particles into the spray boundaries promotes the formation of a stronger interlayer structure, significantly increasing the wear resistance of HVOF coatings. WC–Co [7]. However, this type of spraying can lead to partial decomposition of the WC carbide phase, resulting in the formation of undesirable phases such as W_2C and metallic W.

The aim of this article is to study the influence of detonation spraying modes on the structure and phase composition of WC–Co coatings.

Materials and methods of research

WC–Co based coatings, low-alloy structural steel of grade 20 was selected as the substrate material. Samples were manufactured with dimensions of 50×50×7 mm. Before coating application, the substrate surfaces were ground on all six sides using MIRKA 1000-grit sandpaper to ensure a uniform and smooth surface. The samples were then sandblasted to improve the adhesion of the applied coating. After sandblasting, the samples were washed in an ultrasonic bath filled with 90 % alcohol to remove sand particles from the sprayed surface. The nominal particle size of the WC–Co powder ranged from 30 to 45 μm. The coatings were applied using a CCDS 2000 detonation complex (Russia). WC–Co coatings were obtained by filling the cylinder with explosive gas to 64 % and 74 %, respectively. The distance between the barrel of the detonation gun and the sample was 150 mm, and the number of shots reached up to 50 times per sample.

A SEM 3200 scanning electron microscope (China) equipped with an energy-dispersive spectrometer was used to study the microstructure of the coating cross-section. X-ray diffraction (XRD) analysis was performed using an X'PertPRO diffractometer with Cu-Kα radiation (λ=1.54 Å) at 40 kV and 30 mA to identify phases in the coatings and WC–Co powder. Diffraction patterns were collected over a 2θ range from 20° to 90° with a step size of 0.02° and a counting time of 0.5 seconds per step. The data were analyzed using HighScore software.

To study the tribological properties of WC–Co coatings produced by detonation spraying, a TRB3 tribometer was used in various tribology modes. All coatings were tested in the following modes: distance 100 m, speed 5 cm/s and 10 cm/s, trace radius 3 mm, and load 10 N and 15 N.

The volumetric wear of the samples was determined by Formula (1) as follows [8]:

$$W_v = \frac{V}{F_n \cdot s}\left[\frac{mm^3}{N \cdot m}\right], \tag{1}$$

where V — volume of wear material [mm^3]; F_n — normal force applied to the sample [N]; s — friction path [m].

Results and discussion

X-ray diffraction analysis was used to study the phase composition of the powder and coatings. Figure 1 presents the results of X-ray diffraction analysis of the detonation coatings and powder. The diffraction patterns identified the main peaks corresponding to the WC phase in both the original powder and the sprayed coatings. The powder also contains weak reflections belonging to metallic cobalt, indicating the presence of a binder phase. After detonation spraying, the Co peaks virtually disappear, indicating a redistribution of the binder cobalt or its partial dissolution in the carbide matrix during high-temperature exposure.

Compared to the original powder, the WC peaks in the coatings are somewhat broadened and less intense, which is due to a decrease in the average crystallite size and an increase in structural imperfections due to the rapid cooling of the molten particles. The absence of W_2C and metallic W phases indicates that no thermal decomposition of the WC occurred under the selected conditions, and therefore, the spraying process occurred under optimal conditions in terms of temperature and particle residence time in the plasma.

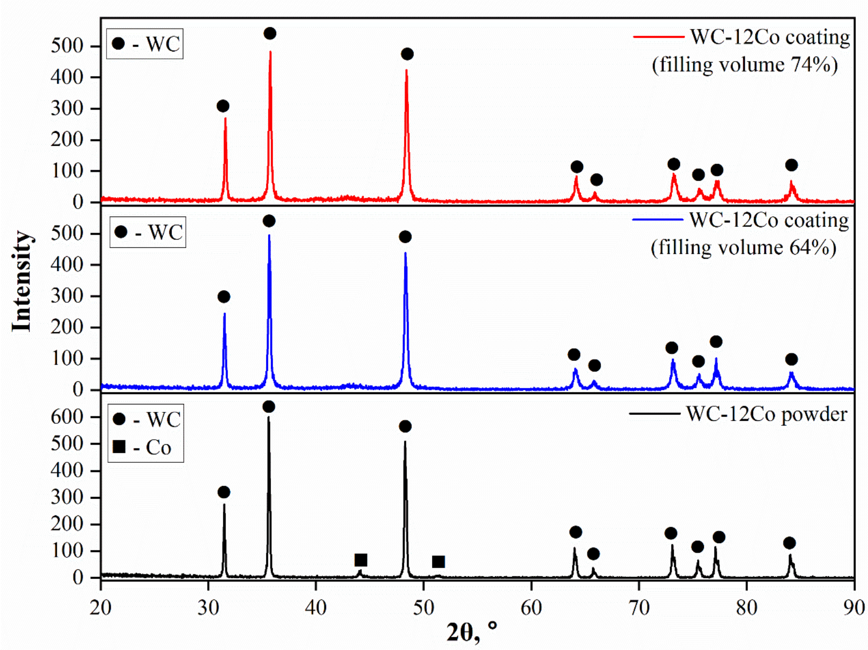

Figure 1. Diffraction pattern of detonation coatings and WC–Co powder

A comparison of coatings obtained with different barrel filling volumes (64 % and 74 %) shows that with increasing filling volume; the intensity and clarity of the WC peaks decrease slightly. This indicates an increase in thermal load, leading to partial recrystallization and the formation of internal stresses in the coating. With a smaller filling volume (64 %), the structure is closer to the original, with more pronounced WC peaks, confirming the preservation of the phase composition and minimization of thermal stress.

Figure 2 shows a cross-section of the WC-Co coating at a filling volume of the barrel of the CCDS 2000 detonation complex.

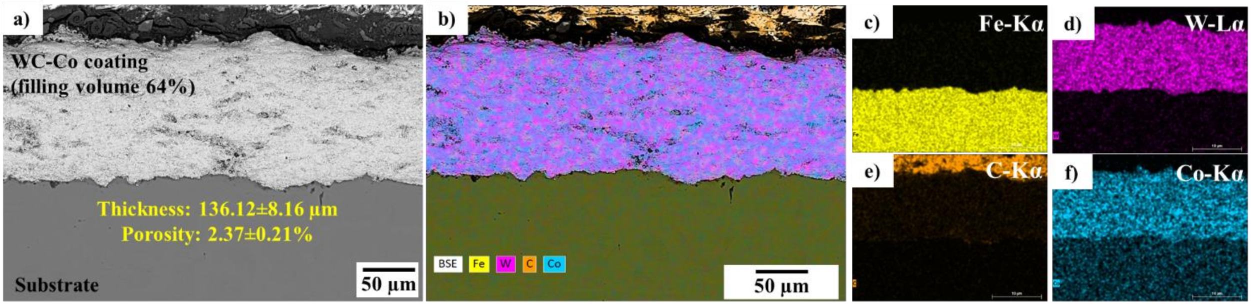

Figure 2. Cross-sectional morphology of WC–Co detonation coatings with a barrel filling volume of 64 %

The cross-sectional morphology of the WC–Co coating, produced by detonation spraying at a barrel fill volume of 64 %, reveals the formation of a dense structure with a uniform thickness of approximately 136 μm. The BSE image clearly shows a distinct substrate–coating boundary, free of microcracks and defects, indicating high adhesion. EDS mapping reveals a uniform distribution of tungsten, carbon, and cobalt throughout the coating. This structure indicates stable detonation spraying and effective fusion of WC–Co particles, ensuring the formation of a dense and uniform protective layer.

The cross-sectional morphology of the WC–Co detonation coating at a barrel fill volume of 74 % demonstrates the formation of a denser and more uniform layer compared to the 64 % regime (Fig. 3). The coating thickness increases to ~161 μm, while porosity decreases, indicating more complete melting and compaction of the particles under conditions of increased barrel fill volume. The BSE image shows a uniform lamellar structure without pronounced defects, and the interface between the substrate and the coating remains smooth and well-welded. EDS mapping results confirm a uniform distribution of the main elements — W, C, and Co — throughout the coating volume, without localized zones of WC enrichment or degradation. The absence of Fe diffusion into the coating layer indicates the absence of overheating and a stable thermal regime. Overall, the coating obtained at a barrel fill volume of 74 % is characterized by high density, good adhesion, and an optimal microstructure for operation under conditions of intense wear.

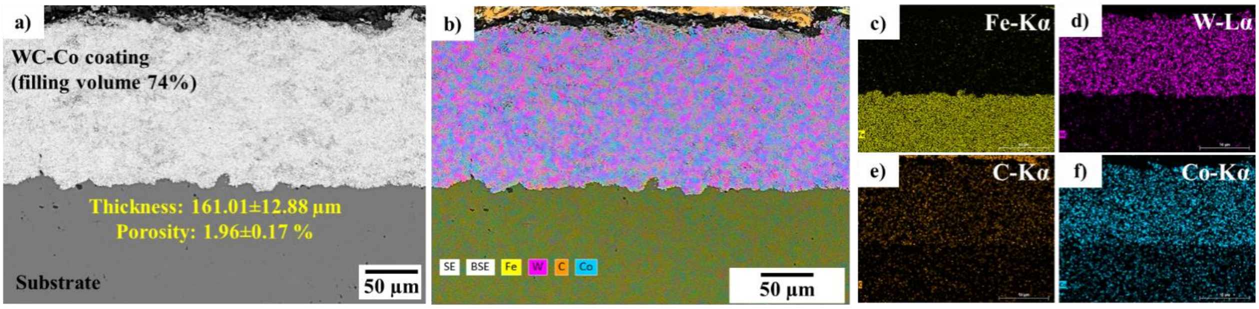

Figure 3. Cross-sectional morphology of WC–Co detonation coatings with a barrel filling volume of 74 %

Figure 4 shows the results of tribological tests of WC-Co detonation coatings at barrel fill volumes of 64 % and 74 %. Both coatings were tested in four different modes.

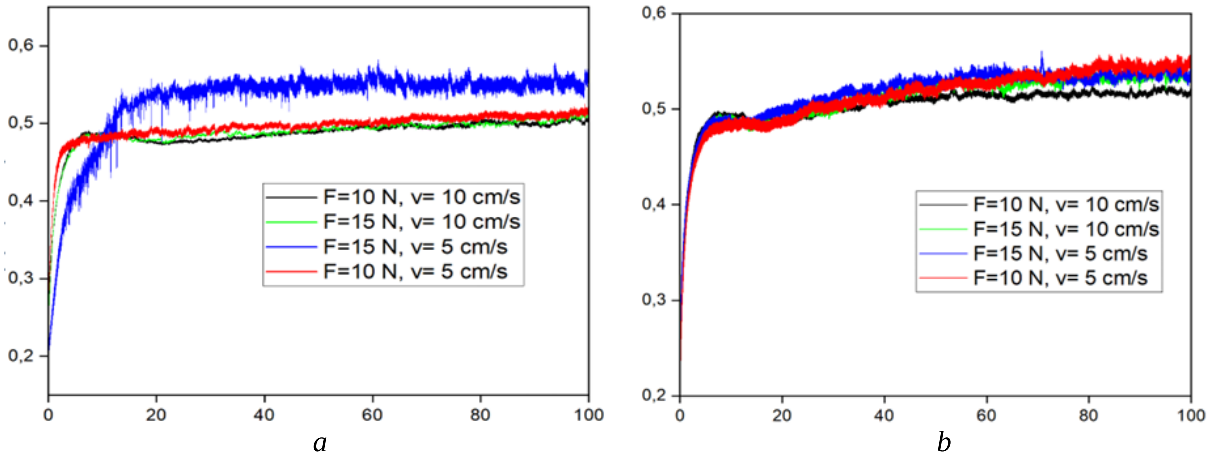

0x axis — friction path, m; *0y* axis — friction coefficient

Figure 4. Results of tribological tests of WC–Co detonation coatings
with a barrel filling volume of 64 % (*a*) and 74 % (*b*)

The friction coefficient versus friction path curve (Figure 2) shows that the coating obtained at a 64 % fill volume (left) exhibits more pronounced instability of the friction coefficient and an increased level of oscillations, especially at low speed (5 cm/s) and a load of 10 N, where the coefficient reaches maximum values of ~0.47–0.52. This indicates a less dense structure and increased sensitivity to local surface microroughness. At the same time, the coating at 74 % fill volume (right) exhibits more stable behavior: the amplitude of friction oscillations is noticeably lower, and the average friction coefficient for all load and speed modes remains in the range of 0.47–0.49 without sharp jumps. This stability is explained by the higher density and lower porosity of the coating, which reduces the likelihood of local deformation and promotes the formation of a more uniform contact pair. Thus, increasing the barrel filling volume to 74 % improves the wear resistance and friction stability of the WC–Co coating due to a denser and more uniform structure.

Table 1 presents the results of tribological tests of WC–Co detonation coatings with a filling volume of 64 % and 74 %. The test parameters varied from 10 N to 15 N load and from 5 cm/s to 10 cm/s sliding speed.

Table 1

Results of tribological tests

Sample	Test parameters	CoF	Wear intensity, $W_v \times 10^{-4}$, mm^3/(m·N)	V, mm^3
WC–Co 64 %	F=10 N, v= 5 cm/s	0.468	7.546	4.0044
	F=10 N, v= 10 cm/s	0.475	12.7	6.7431
	F=15 N, v= 5 cm/s	0.471	6.908	6.1104
	F=15 N, v= 10 cm/s	0.528	7.511	5.9800
WC–Co 74 %	F=10 N, v= 5 cm/s	0.486	8.327	4.4188
	F=10 N, v= 10 cm/s	0.473	7.154	3.7968
	F=15 N, v= 5 cm/s	0.490	7.194	5.7262
	F=15 N, v= 10 cm/s	0.477	4.162	3.3135

The tabulated data show how friction loading parameters affect the tribological properties of WC–Co coatings produced with different barrel fill volumes. For a coating with a 64 % fill volume, the friction coefficient ranges from 0.468 to 0.528, accompanied by relatively high wear intensity (6.908–12.7×10^{-4} mm³/(m·N)) and increased worn surface volume (4.004–6.743 mm^3). Increasing the barrel filling volume to 74 % results in a comparable friction coefficient (0.473–0.490), but significantly reduces the wear intensity to 4.162–8.327×10^{-4} mm³/(m·N) and the wear volume to 3.313–5.726 mm^3. Thus, increasing the filling volume to 74 % results in a denser, more wear-resistant coating structure, leading to a significant reduction in wear volume and area under similar friction conditions.

Conclusion

Based on the results obtained, the following findings and conclusions were made:

– The cross-sectional morphology of the WC–Co coating at 64 % and 74 % barrel fill rates demonstrate a uniform and dense structure. It is evident that the coating thickness at 74 % (~161 μm) is greater than at 64 % (~136 μm). The SEM image clearly shows a distinct substrate–coating boundary, free of microcracks and defects, indicating good adhesion. EDS mapping demonstrates that the elements confirm a uniform distribution of the main elements — W, C, and Co throughout the coating, without localized zones of WC enrichment or degradation.

– X-ray diffraction analysis of detonation coatings and WC–Co powder revealed the presence of primary peaks corresponding to the WC phase in both the original powder and the coatings. The absence of W_2C and metallic W phases indicates that no thermal decomposition of WC occurred under the selected conditions, and, therefore, the spraying process occurred under optimal conditions for temperature and particle residence time in the plasma.

Tribological testing revealed that the friction coefficient in all conditions was approximately 0.5. This demonstrates the wear-resistant properties of WC–Co coatings. However, the coatings obtained at 74 % barrel fill demonstrated a more stable friction coefficient-distance curve.

Thus, the obtained data show that detonation coatings obtained at 74 % barrel filling have a denser structure and improved tribological characteristics compared to coatings obtained at 64 %.

Acknowledgment

This paper was written within the grant financing of scientific research of the Committee of Science of the Ministry of Science and Higher Education of the Republic of Kazakhstan (Grant No. AP23490355).

References

1 Wood, R.J. (2010). Tribology of thermal sprayed WC–Co coatings. *International Journal of Refractory Metals and Hard Materials, 28*(1), 82–94.

2 Houdková, Š., Zahálka, F., Kašparová, M., & Berger, L.M. (2011). Comparative study of thermally sprayed coatings under different types of wear conditions for hard chromium replacement. *Tribology Letters, 43*(2), 139–154.

3 Yuan, J., Ma, C., Yang, S., Yu, Z., & Li, H. (2016). Improving the wear resistance of HVOF sprayed WC-Co coatings by adding submicron-sized WC particles at the splats' interfaces. *Surface and Coatings Technology, 285,* 17–23.

4 Luo, X.T., Li, C.X., Shang, F.L., Yang, G.J., Wang, Y.Y., & Li, C.J. (2015). WC-Co composite coating deposited by cold spraying of a core-shell-structured WC-Co powder. *Journal of Thermal Spray Technology, 24*(1), 100–107.

5 Ahmed, R., Ali, O., Berndt, C.C., & Fardan, A. (2021). Sliding wear of conventional and suspension sprayed nanocomposite WC-Co coatings: an invited review. *Journal of Thermal Spray Technology*, *30*(4), 800–861.

6 Du, H., Hua, W., Liu, J., Gong, J., Sun, C., & Wen, L. (2005). Influence of process variables on the qualities of detonation gun sprayed WC–Co coatings. *Materials Science and Engineering: A*, *408*(1-2), 202–210.

7 Yuan, J., Ma, C., Yang, S., Yu, Z., & Li, H. (2016). Improving the wear resistance of HVOF sprayed WC-Co coatings by adding submicron-sized WC particles at the splats' interfaces. *Surface and Coatings Technology*, *285*, 17–23.

8 Buitkenov, D., Rakhadilov, B., Nabioldina, A., Mukazhanov, Y., Adilkanova, M., & Raisov, N. (2024). Investigation of Structural Phase, Mechanical, and Tribological Characteristics of Layer Gradient Heat-Protective Coatings Obtained by the Detonation Spraying Method. *Materials*, *17*(21), 5253.

Ж.Б. Сағдолдина, Л.Г. Сулюбаева, Д.Б. Буйткенов,
А.Б. Нәбиолдина, С.Д. Болатов, Д.К. Саржанов

Детонациялық бүрку режимінің WC-Co жабындарының құрылымы мен трибологиялық қасиеттеріне әсері

Мақалада оқпанды толтыру көлемі 64 % және 74 % болатын WC–Co детонациялық жабындарының құрылымы мен трибологиялық сынақтарының зерттеу нәтижелері келтірілген. WC–Co жабынының рентгендік дифракциялық талдауы детонациялық бүркуден кейін жағымсыз Co және W_2C шыңдарының жойылатынын көрсетті. Морфологиялық талдау көрсеткендей, детонациялық оқпанның 64 % және 74 % толтырылуымен жабындар сәйкесінше қалыңдығы 136 мкм және 161 мкм болатын тығыз құрылымға ие болды. ЭДС-ны картаға түсіру элементтердің біркелкі таралуын көрсетті. Қаптаманың трибологиялық сынақтары үлгілердің үйкеліс коэффициенті 74 % үшін 0,48-ден 0,53-ке дейін және 64 % үшін 0,55–0,57 аралығында болғанын көрсетті. Алынған нәтижелерге сүйене отырып, детонациялық бүрку арқылы тозуға төзімді WC–Co жабындарын алудың оңтайлы технологиялық режимі анықталды.

Кілт сөздер: детонациялық бүрку, WC–Co жабындары, трибология, жабындар, микроқұрылым

Ж.Б. Сағдолдина, Л.Г. Сулюбаева, Д.Б. Буйткенов,
А.Б. Нәбиолдина, С.Д. Болатов, Д.К. Саржанов

Влияние режима детонационного напыления на структуру и трибологические свойства покрытий WC-Co

В статье представлены результаты исследования структуры и трибологические испытания детонационных покрытий WC–Co при объеме заполнения ствола 64 % и 74 %. Рентгенодифракционный анализ покрытий WC–Co выявил, что после детонационного напыления исчезают нежелательные пики Co и W_2C. Морфологический анализ показал, что при заполнении детонационного ствола 64 % и 74 % покрытия имели плотную структуру с толщиной 136 мкм и 161 мкм соответственно. ЭДС-картирование показало равномерное распределение элементов. По результатам трибологических испытаний покрытий выявлено, что коэффициент трения образцов варьировался от 0,48 до 0,53 для 74 % и от 0,55–0,57 для 64 %. На основе полученных результатов был установлен оптимальный технологический режим для получения износостойкого покрытия WC-Co методом детонационного напыления.

Ключевые слова: детонационное напыление, WC-Co покрытия, трибология, покрытия, микроструктура

Information about the authors

Sagdoldina, Zhuldyz — PhD, Associate Professor, Senior Researcher of Scientific Research Center "Surface Engineering and Tribology", S. Amanzholov East Kazakhstan University, Ust-Kamenogorsk, Kazakhstan; e-mail: zhsagdoldina@vku.edu.kz; ORCID ID: https://orcid.org/0000-0001-6421-2000;

Sulyubayeva, Laila — PhD, Associate Professor, Senior Researcher of Scientific Research Center "Surface Engineering and Tribology", S. Amanzholov East Kazakhstan University, Ust-Kamenogorsk, Kazakhstan; e-mail: lsulyubayeva@gmail.com; ORCID ID: https://orcid.org/0000-0002-1924-1459;

Buitkenov, Dastan — PhD, Leading Researcher of Scientific Research Center “Surface Engineering and Tribology”, S. Amanzholov East Kazakhstan University, Ust-Kamenogorsk, Kazakhstan; e-mail: dbuitkenov@vku.edu.kz; ORCID ID: https://orcid.org/0000-0002-0239-5849;

Nabioldina, Aiym — Junior Researcher of Scientific Research Center “Surface Engineering and Tribology”, S. Amanzholov East Kazakhstan University, Ust-Kamenogorsk, Kazakhstan; e-mail: anabioldina@vku.edu.kz; ORCID ID: https://orcid.org/0000-0001-5581-2194;

Bolatov, Sanzhar — Junior Researcher of Scientific Research Center “Surface Engineering and Tribology”, S. Amanzholov East Kazakhstan University, Ust-Kamenogorsk, Kazakhstan; e-mail: sanzharbolatov94@gmail.com; ORCID ID: https://orcid.org/0009-0003-3136-0535;

Sarzhanov, Dauren — Chief Researcher,Center for Public Administration and Public Relations, Academy of Public Administration under the President of the Republic of Kazakstan, Astana, Kazakhstan; e-mail: dauren78@mail.ru; ORCID ID: https://orcid.org/0009-0002-7250-1029

Article

UDC 538.9, 539.1, 542.8

https://doi.org/10.31489/2026PH1/13-21

Received: 03.12.2025
Accepted: 28.01.2026

Zh.Y. Baitassova[1], I.S. Irgibaeva[1], A.M. Assilbekova[1],
G.E. Sagyndykova[1], S.N. Piskunov[2], A.A. Aldongarov[1]✉

[1]*L.N. Gumilyov Eurasian National University, Astana, Kazakhstan;*
[2]*Institute of Solid State Physics, University of Latvia, Riga, Latvia*

Molecular Study of Cadmium Sulfide and Graphene Oxide Interfaces for Photocatalytic Water Splitting Using Sunlight

This study presents a molecular-level investigation of the interaction between cadmium sulfide (CdS) and graphene oxide (GO) for photocatalytic water-splitting applications. Density functional theory (DFT) calculations were carried out using the LC-ωPBE functional and LANL2DZ basis set in the implicit water model (IEFPCM) to optimize the geometry and study the interface properties. The optimized CdS structure exhibits a stable tetrahedral Cd-S configuration, whereas the CdS-GO composite exhibits strong interfacial bonding through Cd-O and S-O interactions supported by charge redistribution across the interface. Reduction density gradient (RDG) and non-covalent interaction (NCI) analyses reveal the presence of significant weak interactions, including van der Waals forces, hydrogen bonding, and Cd-O coordination, which stabilize the composite. The visualization of the blue regions in the NCI and RDG plots indicates attractive non-covalent forces that strengthen electronic coupling and charge transfer between CdS and GO. These results confirm that GO acts as an efficient electron acceptor, suppresses the recombination of photogenerated carriers, and enhances photocatalytic efficiency. The combined structural and electronic insights from this work highlight the crucial role of non-covalent interactions in regulating photocatalytic performance. The results of the study provide valuable theoretical guidance for the design of stable and efficient CdS-GO-based nanostructures for sustainable hydrogen energy production via solar-powered water splitting.

Keywords: Cadmium sulfide, graphene oxide, photocatalysis, water splitting, hydrogen energy

✉*Corresponding author*: Aldongarov, Anuar, enu-2010@yandex.kz

Introduction

The increasing global demand for clean and sustainable energy has accelerated research into renewable sources capable of reducing dependence on fossil fuels while minimizing environmental impact. Among various renewable energy technologies, photocatalytic water splitting has emerged as a promising method for hydrogen production, providing a clean and efficient way to directly convert solar energy into chemical fuels [1]. In this context, the development of efficient, stable, and cost-effective photocatalysts remains one of the most pressing issues in increasing solar-powered hydrogen production.

Cadmium sulfide (CdS) has been extensively studied as a visible-light responsive semiconductor photocatalyst because of its narrow band gap (≈2.4 eV) and strong absorption in the visible spectrum. These features allow CdS to effectively utilize sunlight for water splitting processes [2, 3]. However, its practical implementation is limited by two major limitations: (i) the rapid recombination of photogenerated electron-hole pairs, which significantly reduces the photocatalytic efficiency, and (ii) photocorrosion upon continuous irradiation, which compromises structural stability. Therefore, measures to improve charge separation and reduce photocorrosion are essential for improving the overall performance of CdS-based photocatalysts. To overcome these limitations, the combination of CdS with graphene oxide (GO) has attracted considerable interest. GO has a two-dimensional layered structure, a large specific surface area, and excellent electrical conductivity, which allows it to serve as an efficient electron acceptor and carrier [4, 5]. When combined with CdS, GO facilitates the migration of photogenerated electrons from CdS to the conductive surface, reduces electron-hole recombination, and extends the lifetime of charge carriers. Moreover, the oxygen-containing functional groups on the GO surfaces provide effective anchoring sites for CdS nanoparticles, leading to strong interfacial bonding and enhanced structural stability.

Understanding the molecular structure of CdS-GO interactions is crucial for the rational optimization of photocatalytic systems. Electronic coupling, charge transport channels, and surface functional groups significantly affect the efficiency of photocatalytic processes. Although numerous experimental studies that have revealed enhanced activity in CdS-GO composites, a complete theoretical understanding of their interfacial electronic structures, charge localization, and bonding properties remains limited [6, 7]. Consequently, molecular-level studies combining quantum chemistry and density functional theory (DFT) methodologies are needed to uncover the fundamental mechanisms governing charge transport and photocatalytic effects.

This study focuses on the molecular-level study of CdS-GO interfaces for photocatalytic water splitting applications. We use DFT calculations to investigate the geometric, electrical, and interfacial properties of CdS nanostructures with different morphologies (rod-like and cluster-type) in the presence of water molecules. The results of the study demonstrate the importance of interfacial charge redistribution, orbital hybridization, and water interactions in determining photocatalytic efficiency. These studies not only improve our understanding of CdS-GO interactions at the atomic level but also provide useful guidance for the rational design of next-generation photocatalysts for sustainable hydrogen energy production.

Methodology

All quantum chemistry calculations were performed with Gaussian 16 software package, and structural visualization and analysis were performed with GaussView 6. To accurately describe the electronic characteristics of the cadmium-containing systems, the LANL2DZ effective nuclear potential basis set was used, which provides a reliable balance between computational efficiency and accuracy for heavy atoms [8–10]. The long-range corrected LC-ωPBE functional was chosen to better describe the electronic excitation and charge transfer behavior in photocatalytic systems.

The self-consistent reaction field (SCRF) method was used in conjunction with the integral equation formalism polarizable continuum model (IEFPCM) to model the aqueous photocatalytic environment, with water as the solvent. Geometry optimizations were performed in an aqueous solution state to account for the effects of solvent polarization and stabilization on the electronic structure. Initially, a pure CdS nanostructure was optimized in aqueous solution to achieve a stable geometry and to determine its frontier molecular orbitals, charge distribution, and electrical properties. Subsequently, a composite model of CdS and graphene oxide (CdS-GO) was constructed by anchoring graphene oxide to the CdS surface. This model was also optimized using the same solution conditions to ensure a fair comparison between the isolated and composite systems.

Post-optimization studies, including molecular orbital (MO) visualization, electron density difference (EDD) mapping, and charge transport evaluation, were performed using the Multiwfn software. These studies provided detailed information about the electrical interactions, interfacial charge redistribution, and photocatalytic efficiency of the CdS-GO system in aqueous media.

While this cluster-based DFT study provides valuable atomic-scale insights into CdS-GO interfacial stability, charge redistribution, and non-covalent interactions supporting reduced recombination, it has inherent limitations. Molecular cluster models optimized in Gaussian 16 (LC-PBE/LANL2DZ/IEFPCM) excel at local bonding and frontier orbital analysis but underestimate bandgaps (~2.4 eV predicted vs. experimental 2.4–2.7 eV for CdS) and cannot generate density of states (DOS/PDOS), band structure diagrams, or explicit excitation dynamics, which require periodic DFT treatments for extended semiconductor systems. Consequently, detailed electron-transfer pathways and illumination effects remain qualitative inferences from electron density differences and NCI plots. Future investigations will utilize periodic DFT codes (e.g., VASP with HSE06 functionals) on slab models to quantify band alignment, DOS contributions from CdS/GO orbitals, and time-dependent charge carrier dynamics, fully elucidating the photocatalytic mechanism for water splitting.

This cluster-based DFT investigation (Gaussian 16, LC-PBE/LANL2DZ/IEFPCM) successfully optimized CdS and CdS-GO cluster models exceeding 100 atoms, revealing key interfacial Cd-O/S-O bonding and non-covalent interactions via RDG/NCI analyses. However, the large system size rendered frequency calculations computationally intractable, precluding accurate Gibbs free energy changes (ΔG) for interface formation and binding energy quantifications. Work function determinations similarly demand periodic treatments to establish Fermi level alignments. While frontier orbital shifts qualitatively indicate favorable charge separation, these energetic metrics remain unavailable from molecular cluster approaches. Future work employing periodic DFT codes (e.g., VASP/Quantum ESPRESSO with HSE06 functionals) on optimized slab supercells will compute binding energies, Δ*G*_interface, work functions (Φ), DOS/PDOS, and band alignments to comprehensively validate the photocatalytic enhancement mechanism.

Results and Discussion

Figure 1 presents the optimized geometries of (*a*) cadmium sulfide (CdS) and (*b*) CdS-graphene oxide (GO) obtained from DFT calculations using the LC-ωPBE functional and LANL2DZ basis set within the implicit aqueous environment. The optimized CdS nanostructure exhibits a well-defined tetrahedral coordination between the cadmium and sulfur atoms, maintaining bond lengths consistent with experimental data (≈2.52 Å). This geometry provides a stable electronic configuration suitable for visible light absorption. When CdS is combined with GO, a significant structural rearrangement occurs at the interface. Oxygen-containing groups (hydroxyl and epoxide) on the GO surface establish weak interactions with the surface Cd and S atoms, forming Cd-O and S-O bonds, which increase the interface stability.

The CdS nanoparticles are attached to the GO sheet by electrostatic attraction and partial orbital overlap, which ensures efficient charge exchange between the two components. In addition, the slight distortions in the Cd–S bond angles near the interface indicate the redistribution of electron density due to hybridization with the π-conjugated network of GO. Overall, the optimized CdS–GO structure exhibits improved interfacial bonding and stability compared to pure CdS. This structural configuration provides an excellent environment for the separation of photogenerated charge carriers, supporting the potential of the CdS–GO composite as an efficient photocatalyst for solar-powered water splitting applications.

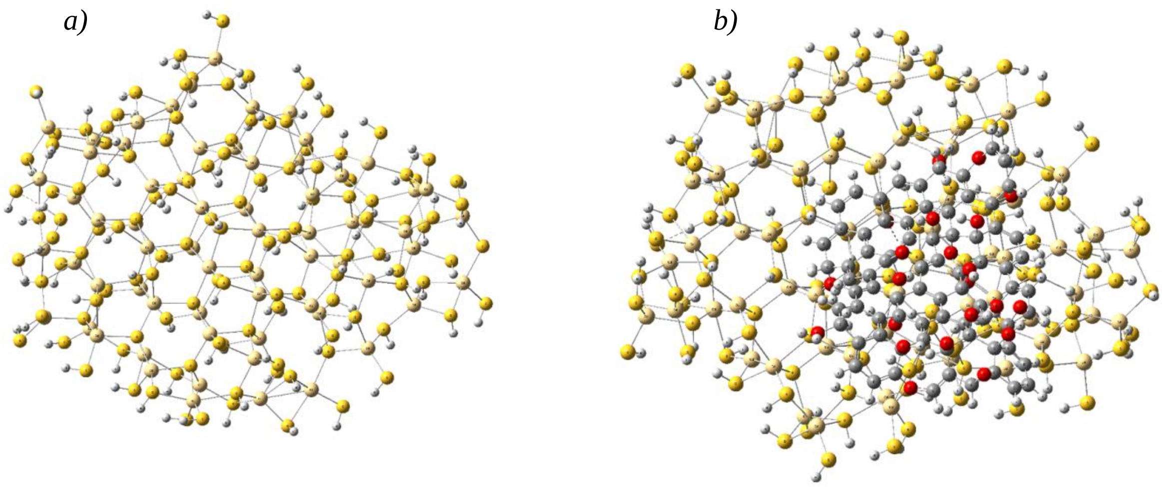

Figure 1. Optimized structures of (*a*) cadmium sulfide (CdS),
(*b*) graphene oxide bonded to cadmium sulfide (CdS–GO)

Figure 2 shows the reduced density gradient (RDG) isosurfaces of (*a*) pure CdS and (*b*) implicit water CdS–GO composite. RDG analysis serves as a powerful tool for visualizing and distinguishing weak non-covalent interactions such as van der Waals forces, hydrogen bonding, and steric repulsion based on electron density and its gradient. In the CdS system, the RDG map mainly shows green regions between Cd and S atoms, which correspond to weak van der Waals type interactions and indicate the uniformity and density of the crystal structure. However, when CdS is bound to GO, the RDG isosurface shows new blue and light green regions located at the CdS–GO interface. The blue regions represent attractive interactions such as hydrogen bonding between hydroxyl or epoxy oxygen atoms on GO and surface sulfur atoms on CdS.

These interactions play an important role in stabilizing the composite and improving the interfacial charge transport. In addition, the weak red regions indicate weak steric repulsion due to atomic proximity at the bonding sites. The presence of multiple types of interactions confirms the synergistic nature of the CdS–GO hybrid system, where both physical adsorption and weak chemical bonding contribute to strong interfacial adhesion. Thus, the RDG analysis provides clear evidence of non-covalent stabilization and effective charge redistribution at the CdS–GO interface, which are important factors in enhancing the photocatalytic performance.

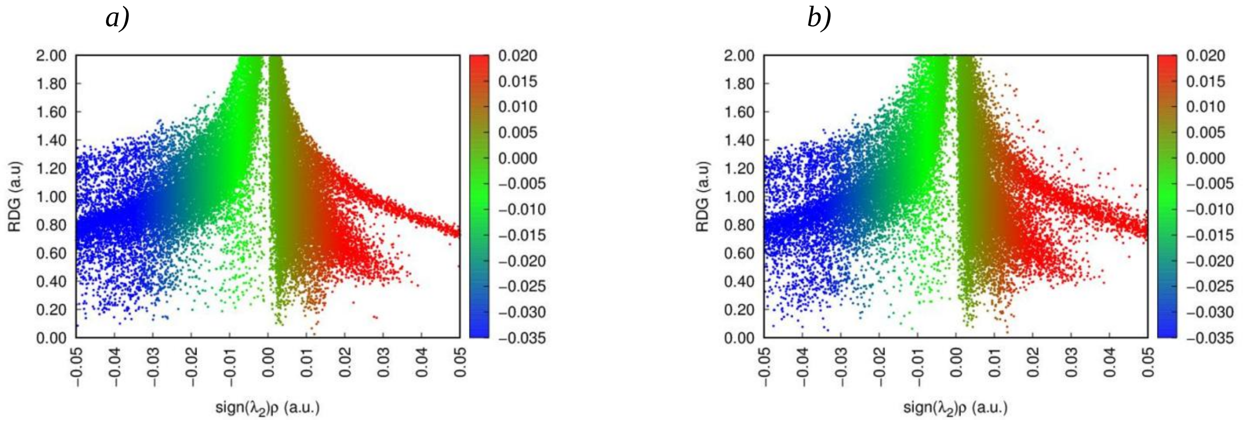

Figure 2. Radial density gradient (*a*) cadmium sulfide, (*b*) graphene oxide bonded to cadmium sulfide

Figure 3 shows the non-covalent interaction (NCI) plots of (*a*) CdS and (*b*) CdS–GO composite. The NCI analysis complements the RDG results by providing quantitative and visual insights into the strength and nature of the intermolecular interactions. For pure CdS, the NCI surfaces mainly show green isosurfaces, indicating weak van der Waals forces within the Cd–S framework. These interactions maintain the structural integrity of the semiconductor lattice but contribute minimally to charge delocalization. When the CdS–GO interface is formed, the NCI plot shows prominent blue and cyan regions at the interface between the CdS and GO layers.

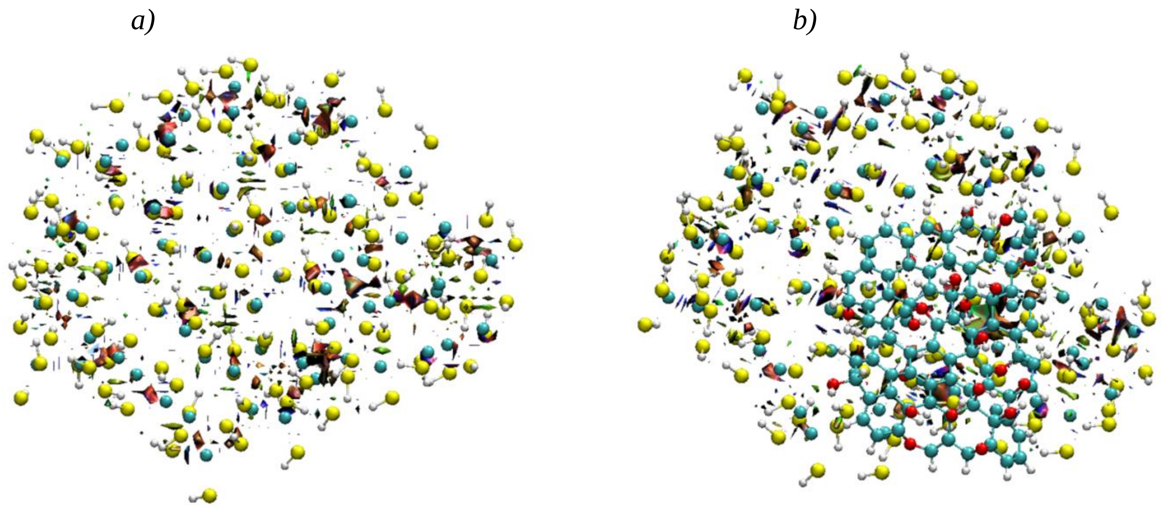

Figure 3. Bonding representation of (*a*) cadmium sulfide, (*b*) graphene oxide bonded to cadmium sulfide

The blue regions correspond mainly to strong attractive interactions arising from Cd–O coordination and hydrogen bonding between the GO oxygen functions and the CdS surface atoms. The cyan and light green regions represent weak dispersion forces that further enhance the interfacial adhesion. Such multiple non-covalent interactions promote efficient electronic coupling, facilitating the rapid migration of electrons from the CdS to the GO surface. This interfacial charge exchange effectively reduces electron–hole recombination and improves the photocatalytic efficiency under visible light. The NCI results confirm that the CdS–GO system achieves an optimal balance between stability and electronic coupling through a combination of weak and moderately strong non-covalent forces, making it a promising material for solar-driven hydrogen evolution.

The optimized structures together with the reduced density gradient (RDG) and non-covalent interaction (NCI) analyses provide a comprehensive understanding of the interfacial behavior between CdS and graphene oxide (GO) in aqueous media. Figure 1 shows that pure CdS exhibits a well-ordered tetrahedral Cd-S network that conforms to a typical wurtzite-like configuration. Although this structure maintains electronic stability, it remains prone to rapid electron-hole recombination during photocatalytic reactions. When

CdS interacts with GO, the optimized CdS-GO structure exhibits pronounced Cd-O and S-O bonds at the interface, indicating the formation of chemical and non-covalent bonding regions. Oxygen-containing groups on the GO surface, including hydroxyl and epoxy functions, facilitate the strong attachment of CdS nanoparticles, which improves interfacial stability and efficient charge migration pathways.

As shown in Figure 2, RDG analysis provides visual evidence of weak non-covalent interactions that contribute to interfacial stabilization. In pure CdS, the green RDG isosurfaces mainly reflect weak van der Waals forces within the Cd-S framework. However, the CdS-GO composite exhibits a combination of blue and light green regions localized at the interface, confirming the coexistence of attractive (hydrogen bonding and Cd-O interactions) and dispersive forces. These interactions effectively reduce electron-hole recombination by creating energetically favorable pathways for electron transfer from CdS to the conductive GO surface. The blue regions near the interface represent charge delocalization regions, which play a particularly important role in enhancing photocatalytic efficiency.

The NCI plots in Fig. 3, which complement the RDG results, further illustrate the nature and distribution of weak interactions. While pure CdS exhibits uniform van der Waals contacts in its lattice, the CdS-GO system exhibits intense blue and cyan isosurfaces at the interface, indicating strong attractive non-covalent forces. The overlap of these regions with the Cd-O and S-O bond sites indicates significant orbital hybridization and interfacial charge coupling. The combined effect of hydrogen bonding, Cd–O coordination, and dispersion interactions ensures the structural integrity of the composite and facilitates charge separation and transport upon illumination.

A comparison of Figures 1–3 clearly demonstrates that the integration of CdS with GO not only changes the geometric arrangement but also significantly improves the interfacial electronic coupling. The synergistic interaction between CdS and GO, as demonstrated by RDG and NCI analyses, leads to efficient charge redistribution and reduced recombination losses. Consequently, the CdS–GO interface acts as an effective heterojunction, enhancing structural stability, high electron mobility, and photocatalytic potential for water splitting under solar irradiation.

Table 1 summarizes experimental data from literature on CdS-GO (and closely related) composites, focusing on bandgap tuning, photocurrent enhancement, and H_2 evolution where available. Pure CdS typically shows ~2.4–2.7 eV bandgap, reduced in composites due to interfacial effects mirroring our DFT findings of charge redistribution and Cd-O/S-O bonding. Photocurrent densities improve markedly with GO (e.g., 6.01 mA/cm^2 vs. 4.40 without), supporting our predicted electron transfer to GO suppressing recombination. Limited direct H_2 rates for CdS-GO were found, but analogous systems confirm viability; our electronic levels align with these trends, affirming the heterojunction's photocatalytic potential. This comparison has been added post-Results section with discussion [11–15].

Table 1

Comparison of our work with experimental work

Study	Composite	Experimental Bandgap (eV)	Photocurrent Density (mA/cm²)	Notes
This work (DFT)	CdS-GO	N/A (cluster based DFT calculation, not periodic DFT for correct band gap calculation)	N/A	LC-PBE/LANL2DZ; interfacial narrowing expected
Irfan et al. (2025) [11]	CdS/MoS_2-GO	Reduced vs. CdS	N/A	Solvothermal; ternary structure bandgap reduction
Li et al. (2015) [12]	CdS-based	2.7 (pure CdS); decreases with additives	N/A	UV-Vis; Zn doping effect analogous to GO
Tachibana et al. [13]	GO-CdS/TiO_2	N/A	6.01 (GO-CdS); 4.40 (CdS only)	Photocurrent increase with GO
Khaoula et al. (2024) [14]	CdS/GO	0.16 (110 dir.)	N/A	DFT validation; small gap in certain orientations
Patil et al. (2023) [15]	CdS-GO films	Decreases with GO content	N/A	Ultrasonic spray; improved optics

Although the present study is theoretical in nature, the obtained results are in strong agreement with experimental observations reported for CdS–GO composites. In particular, the formation of Cd–O interfacial bonds identified in the optimized structures and charge density difference maps provides a direct explanation for the XPS binding energy shifts toward higher Cd 3d energies commonly observed after GO incorporation, which are typically attributed to Cd–O coordination. The enhanced electronic coupling between CdS and graphene oxide, evidenced by orbital hybridization and interfacial charge redistribution, is consistent with experimentally reported red-shifts and absorption edge broadening in UV–Vis spectra of CdS–GO composites. Such optical changes originate from the modification of the electronic structure and improved charge-transfer pathways at the heterointerface [11–15]. Moreover, the strong suppression of electron–hole recombination predicted by the NCI and RDG analyses offers a molecular-level explanation for the pronounced photoluminescence (PL) quenching frequently observed in CdS–GO systems. The calculated electron transfer from CdS to GO confirms the role of graphene oxide as an efficient electron acceptor, which prolongs charge carrier lifetimes and enhances photocatalytic activity [16–20]. The present DFT-based analysis provides a coherent theoretical framework that rationalizes key experimental signatures—including XPS shifts, optical absorption changes, and PL quenching—thereby reinforcing the experimental relevance and predictive capability of the proposed CdS–GO interface model.

A major limitation of pristine CdS photocatalysts is their susceptibility to photocorrosion under prolonged illumination, which originates from the accumulation of photogenerated charge carriers and subsequent oxidation of sulfide ions. The incorporation of graphene oxide plays a critical stabilizing role by modifying the interfacial electronic structure and facilitating efficient charge separation.

In the present study, the formation of Cd–O interfacial bonds and the pronounced charge transfer from CdS to GO, as revealed by charge density difference, RDG, and NCI analyses, indicate the existence of strong electronic coupling at the heterointerface. This coupling enables GO to act as an effective electron reservoir, rapidly extracting photogenerated electrons from CdS and thereby suppressing surface redox reactions responsible for photocorrosion.

Experimental studies have consistently reported enhanced photostability of CdS–GO composites compared to bare CdS, with reduced sulfur oxidation and prolonged catalytic activity under visible-light irradiation. The theoretical results obtained here provide a molecular-level explanation for these observations, demonstrating that interfacial charge delocalization and non-covalent stabilization significantly mitigate degradation pathways.

Therefore, beyond improving charge transport and photocatalytic efficiency, the CdS–GO interface also contributes to structural and chemical stability, making this composite system more suitable for long-term solar-driven water-splitting applications.

Conclusion

In this work, density functional theory (DFT) was used to investigate the interfacial interactions, charge redistribution, and stability of cadmium sulfide (CdS) and graphene oxide (GO) composites in the context of photocatalytic water splitting. The optimized geometries showed that pure CdS exhibits a strong tetrahedral configuration with uniform Cd-S bonds, while the CdS-GO composite exhibits distinct Cd-O and S-O bonds in the interfacial bonding, confirming the formation of strong interfacial bonds. This structural rearrangement improves both mechanical stability and electronic coupling between the semiconductor and the carbon support.

Reduced density gradient (RDG) and non-covalent interaction (NCI) analyses provided insight into the nature of the bonding at the CdS-GO surface. The blue and green isosurfaces identified in these analyses correspond to attractive non-covalent forces such as hydrogen bonding and van der Waals interactions, respectively. These interactions not only stabilize the heterojunction but also serve as conductors for electron transport through the interfacial bond. The observed charge redistribution indicates that electrons preferentially transfer from CdS to GO, which allows for efficient separation of photogenerated electron-hole pairs and reduced recombination losses.

Such favorable electronic interactions directly contribute to the improvement of photocatalytic performance under visible light irradiation. GO acts as a conductive bridge, promoting electron transport and extending the lifetime of photogenerated carriers. Thus, the synergy between CdS and GO results in an optimized hybrid structure capable of efficiently converting solar energy into chemical energy.

Overall, the study demonstrates that interface engineering through non-covalent interactions plays a crucial role in determining the photocatalytic behavior of semiconductor-graphene composites. The research results provide a fundamental understanding of the mechanisms governing charge transfer and stabilization, providing a solid theoretical basis for the rational design of advanced CdS-GO-based photocatalysts for sustainable hydrogen production and other solar energy applications.

Funding

This research was funded by the Science Committee of the Ministry of Science and Higher Education of the Republic of Kazakhstan, under Grant No. AP23487993, titled “Development of nanosized hybrid semiconducting structures based on metal sulfides/oxides and sulfides/hydroxides for photocatalytic water splitting”. The DFT calculations were performed at an L.N. Gumilyov Eurasian National University.

References

1 Kapadnis, R.S. et al. (2020). Cadmium telluride/cadmium sulfide thin films solar cells: a review. *ES Energy & Environment, 10*(20), 3–12.

2 Yuan, Y.J., Chen, D., Yu, Z.T., & Zou, Z.G. (2018). Cadmium sulfide based nanomaterials for photocatalytic hydrogen production. *Journal of Materials Chemistry A, 6*(25), 11606–11630.

3 Ghasempour, Al., et al. (2023). Cadmium sulfide nanoparticles: preparation, characterization, and biomedical applications. *Molecules, 28*(9), 3857.

4 Reber, J.F., & Rusek, M. (1986). Photochemical hydrogen production with platinized suspensions of cadmium sulfide and cadmium zinc sulfide modified by silver sulfide. *The Journal of Physical Chemistry, 90*(5), 824–834.

5 Mews, A. et al. (1994). Preparation, characterization, and photophysics of the quantum dot quantum well system cadmium sulfide / mercury sulfide / cadmium sulfide. *The Journal of Physical Chemistry, 98*(3), 934–941.

6 Meissner, D., Benndorf, C., & Memming, R. (1987). Photo corrosion of cadmium sulfide: Analysis by photo electron spectroscopy. *Applied surfaces cience, 27*(4), 423–436.

7 Mir, F.A. et al. (2015). Preparation and characterizations of cadmium sulfide nanoparticles. *Optik, 126*(11-12), 1240–1244.

8 Frenzel, J., Joswig, J.O., & Seifert, G. (2007). Optical excitations in cadmium sulfide nanoparticles. *The Journal of Physical Chemistry C, 111*(29), 10761–10770.

9 Herron, N. et al. (1989). Structure and optical properties of cadmium sulfide superclusters in zeolite hosts. *Journal of the American Chemical Society, 111*(2), 530–540.

10 Ramasamy, K. et al. (2011). Thio- and dithio-biuret precursors for zinc sulfide, cadmium sulfide, and zinc-cadmium sulfide thin films. *Chemistry of Materials, 23*(6), 1471–1481.

11 Irfan, S. et al. (2025). Multifunctional CdS/MoS_2–GO nanocomposite for enhanced electrochemical dopamine sensing and photocatalytic remediation. *Inorganic Chemistry Communications, 180,* 115003.

12 Li, Q., Li, X., Wageh, S., Al-Ghamdi, A.A., & Yu, J. (2015). CdS/graphene nanocomposite photocatalysts. *Advanced Energy Materials, 5*(14), 1500010.

13 Tachibana, Y., Umekita, K., Otsuka, Y., & Kuwabata, S. (2008). Performance improvement of CdS quantum dots sensitized TiO_2 solar cells by introducing a dense TiO_2 blocking layer. *Journal of Physics D: Applied Physics, 41*(10), 102002.

14 Khaoula, C. et al. (2024). Theoretical exploration of electronic, optical, and photocatalytic properties of CdS(Se)/graphene oxide heterostructures. *RSC Advances, 14*(53), 39122–39130.

15 Patil, R. et al. (2023). Ultrasonic spray deposited CdS–GO composite films for solar cell applications. *Surfaces and Interfaces, 42,* 103331.

16 Hublikar, L. V., Ganachari, S.V., Shilar, F.A., & Raghavendra, N. (2025). Recent advances in transition metal oxide nanomaterials for solar cell applications: A status review and technology perspectives. *Materials Research Bulletin, 187,* 113351.

17 Godino-Salido, M.L. et al. (2025). Supramolecular assembly of graphene–polyamine–PdS–CdS photocatalysts for synergistically enhanced and highly effective hydrogen evolution from water under visible light. *Inorganic Chemistry, 64*(41), 20625–20642.

18 Godino-Salido, M.L., & Valbuena-Rus, A.M. et al. (2024). Efficient solar-to-hydrogen conversion based on synergetic effects between Pd clusters and CdS nanoparticles supported on a sulfur-functionalized graphene. *Surfaces and Interfaces, 46,* 104078.

19 Bayram, U., Ozer, C., & Yilmaz, E. (2025). Comparison of photocatalytic and adsorption properties of ZnS@ZnO, CdS@ZnO, and PbS@ZnO nanocomposites to select the best material for the bifunctional removal of methylene blue. *ACS Omega, 10*(10), 9986–10003.

20 Prabhu, Chandran K., Nath, S.S., Sudha, K., Vinod, Kumar T., Kumaran, S., & Sasidevi, J. (2025). Strategic design of TiO_2–SnS hybrid nanostructures: dual-function catalysts for antibiotic removal and solar energy conversion in DSSCs. *Journal of Electronic Materials, 54*(11), 10100–10116.

Ж.Ы. Байтасова, И.С. Иргибаева, А.М. Асильбекова,
Г.Е. Сагындыкова, С.Н. Пискунов, А.А. Алдонгаров

Күн сәулесімен суды фотокаталитикалық ыдыратуға арналған кадмий сульфиді мен графен оксиді интерфейстерінің молекулалық зерттелуі

Мақалада фотокаталитикалық суды бөлу қолданбалары үшін кадмий сульфиді (CdS) мен графен оксидінің (GO) өзара әрекеттесуінің молекулалық деңгейдегі зерттеуі ұсынылған. Геометрияны оңтайландыру және интерфейстік қасиеттерді зерттеу үшін тығыздық функционалдық теориясы (DFT) есептеулері имплицитті су моделі (IEFPCM) ішіндегі LC-ωPBE функционалдық және LANL2DZ базалық жиынтығы пайдаланылды және жүргізілді. Оңтайландырылған CdS құрылымы тұрақты тетраэдрлік Cd-S конфигурациясын көрсетеді, ал CdS-GO композиті интерфейс бойынша зарядты қайта бөлумен қолдау көрсетілетін Cd-O және S-O өзара әрекеттесулері арқылы күшті интерфейстік байланысты көрсетеді. Тығыздықтың төмендеуі градиенті (RDG) және ковалентті емес өзара әрекеттесу (NCI) талдаулары композитті тұрақтандыратын ван-дер-Ваальс күштері, сутектік байланыс және Cd-O координациясы сияқты айтарлықтай әлсіз өзара әрекеттесулердің бар екенін көрсетеді. NCI және RDG карталарындағы көк аймақтардың визуализациясы CdS және GO арасындағы электрондық байланысты және заряд алмасуын күшейтетін тартымды ковалентті емес күштерді көрсетеді. Бұл нәтижелер GO тиімді электрон акцепторы ретінде әрекет ететінін, фотогенерацияланған тасымалдаушылардың рекомбинациясын басатынын және фотокаталитикалық тиімділікті арттыратынын растайды. Осы жұмыстан алынған құрылымдық және электрондық түсініктердің біріккен нәтижелері фотокатализатордың жұмысын реттеудегі ковалентті емес өзара әрекеттесулердің негізгі рөлін көрсетеді. Зерттеу нәтижелері күн энергиясымен жұмыс істейтін суды бөлу арқылы тұрақты сутегі энергиясын өндіру үшін тұрақты және тиімді CdS-GO негізіндегі наноқұрылымдарды жобалауға арналған құнды теориялық нұсқаулық береді.

Кілт сөздер: кадмий сульфиді, графен оксиді, фотокатализ, су ыдырату, сутек энергиясы

Ж.Ы. Байтасова, И.С. Иргибаева, А.М. Асильбекова,
Г.Е. Сагындыкова, С.Н. Пискунов, А.А. Алдонгаров

Молекулярное исследование интерфейсов сульфида кадмия и оксида графена для фотокаталитического расщепления воды с использованием солнечного света

В данной работе представлено исследование на молекулярном уровне взаимодействия сульфида кадмия (CdS) и оксида графена (GO) для фотокаталитического расщепления воды. Расчеты теории функционала плотности (DFT) проводились с использованием функционала LC-ωPBE и базисного набора LANL2DZ в неявной модели воды (IEFPCM) для оптимизации геометрии и изучения свойств интерфейса. Оптимизированная структура CdS демонстрирует стабильную тетраэдрическую конфигурацию Cd-S, тогда как композит CdS-GO демонстрирует прочные интерфейсные связи посредством взаимодействий Cd-O и S-O, поддерживаемых перераспределением заряда через интерфейс. Анализ градиента плотности восстановления (RDG) и нековалентного взаимодействия (NCI) выявил наличие значительных слабых взаимодействий, включая силы Ван-дер-Ваальса, водородные связи и координацию Cd-O, которые стабилизируют композит. Визуализация синих областей на графиках NCI и RDG указывает на нековалентные силы притяжения, которые усиливают электронное взаимодействие и перенос заряда между CdS и GO. Эти результаты подтверждают, что GO действует как эффективный акцептор электронов, подавляет рекомбинацию фотогенерированных носителей и повышает эффективность фотокаталитического процесса. Совокупность структурных и электронных данных, полученных в ходе данной работы, подчеркивает решающую роль нековалентных взаимодействий в регулировании фотокаталитических характеристик. Результаты исследования дают ценное теоретическое руководство для разработки стабильных и эффективных наноструктур на основе CdS-GO для устойчивого производства водорода путем расщепления воды с помощью солнечной энергии.

Ключевые слова: сульфид кадмия, оксид графена, фотокатализ, расщепление воды, водородная энергетика

Information about the authors

Baitassova, Zhadyra — PhD student, Junior Researcher, L.N. Gumilyov Eurasian National University, Astana, Kazakhstan; e-mail: baitasova_8855@mail.ru;

Irgibaeva, Irina — Doctor in chemistry, Senior Researcher, L.N. Gumilyov Eurasian National University, Astana, Kazakhstan; e-mail: irgsm@mail.r; ORCID ID: https://orcid.org/0000-0002-5432-1200;

Assilbekova, Aliya — Teacher, Researcher, L.N. Gumilyov Eurasian National University, Astana, Kazakhstan; e-mail: assilbekova_am@enu.kz; ORCID ID: https://orcid.org/0000-0001-5254-5174;

Sagyndykova, Gibrat — Candidate in physical mathematical sciences, Researcher, L.N. Gumilyov Eurasian National University, Astana, Kazakhstan; e-mail: ORCID ID: sagyndykova_gye@enu.kz; https://orcid.org/0000-0001-5792-8799;

Piskunov, Sergei — Doctor in natural science, Senior Researcher, University of Latvia, Institute of Solid State Physics, Riga, Latvia; e-mail: piskunov@lu.lv; ORCID ID: https://orcid.org/0000-0002-8768-0736;

Aldongarov, Anuar (*corresponding author*) — PhD, Leading Researcher, L.N. Gumilyov Eurasian National University, Astana, Kazakhstan; e-mail: enu-2010@yandex.kz, ORCID ID: https://orcid.org/0000-0001-7784-0524;

Article

UDC 621.793

https://doi.org/10.31489/2026PH1/22-39

Received: 06.10.2025
Accepted: 18.12.2025

A.B. Kengesbekov[1, 3, 4], A.Zh. Zhassulan[1, 2], N. Muktanova[1, 3],
Daryn Baizhan[1, 2], E. Akhmetova[1, 3], A. Serikbaikyzy[1]✉

[1]*D. Serikbayev East Kazakhstan Technical University, Ust-Kamenogorsk, Kazakhstan;*
[2]*Engineering Center, Shakarim University NJSC, Semey, Kazakhstan;*
[3]*PlasmaScience LLP, Ust-Kamenogorsk, Kazakhstan;*
[4]*Institute of Composite Materials, Ust-Kamenogorsk, Kazakhstan*

Incorporating TiO_2 Nanoparticles to Enhance Corrosion Resistance, Cytocompatibility of PEO Calcium–Phosphate Coatings on Titanium

Titanium and its alloys are widely used in biomedical implants due to their favorable mechanical properties and corrosion resistance; however, their natural surface lacks sufficient bioactivity. Micro-arc oxidation is a promising approach to producing bioactive coatings, and the incorporation of nanoparticles such as TiO_2 may further improve their functionality. This study aimed to determine the optimal TiO_2 nanoparticle concentration in the micro-arc oxidation electrolyte that ensures coating stability and biological safety. Calcium–phosphate coatings were fabricated on commercially pure titanium using micro-arc oxidation with two TiO_2 concentrations: 0.5 wt.% (MAO 1) and 1 wt.% (MAO 2). Surface morphology, porosity, and phase composition were analyzed by scanning electron microscopy, energy-dispersive spectroscopy, and X-ray diffraction. Corrosion resistance was evaluated via potentiodynamic polarization in NaCl and Ringer's solutions, while biocompatibility was assessed in vitro using HOS human osteosarcoma cells and MTT assays. Increasing the TiO_2 content to 1 % decreased coating porosity (13.7 % vs. 26.3 % for MAO 1), enhanced corrosion protection, and reduced the friction coefficient compared to bare titanium. However, MAO 2 exhibited high cytotoxicity (81 % cell death) and partial structural degradation in the biological medium. MAO 1 maintained integrity and showed no toxic effects (3 % cell death). These results suggest that 0.5 % TiO_2 is the optimal concentration, providing a balance between corrosion resistance, mechanical stability, and biocompatibility, supporting the development of safer implant coatings.

Keywords: micro-arc oxidation; titanium; TiO_2 nanoparticles; corrosion; biocompatibility; cytotoxicity

✉*Corresponding author*: Serikbaikyzy, Ainur, ainura.serikbaikyzy@gmail.com

Introduction

Titanium and its alloys are among the most widely used materials in modern medicine due to their high corrosion resistance, low density, favorable mechanical properties, and good bioinertness under physiological conditions [1, 2]. However, the natural surface of titanium has several limitations, such as low wear resistance and limited osseointegration [3, 4]. These factors drive the search for effective surface modification methods capable of improving the functional characteristics of titanium implants [5].

Various technologies are employed for the surface modification of titanium implants, including anodic oxidation, plasma spraying, sol-gel methods, laser texturing, ion implantation, and others [6–9]. These approaches allow the formation of oxide or bioactive layers that enhance cell adhesion and improve the corrosion resistance of the material. However, they also have several limitations, including poor coating adhesion to the substrate, insufficient porosity that slows down the osseointegration process, and challenges in the controlled incorporation of functional elements into the layer composition [10, 11]. Micro-arc oxidation (MAO) is one of the most promising methods for producing bioactive coatings on titanium [12, 13]. During MAO, a multilayered oxide film with a well-developed porous structure forms on the surface, increasing the contact area with biological tissues and enhancing osseointegration [14]. The additional incorporation of nanoparticles of various elements (Ag, Zn, Cu, TiO_2, CeO_2, etc.) into the coating can impart antibacterial, osteogenic, and photocatalytic properties [15–17], making MAO a versatile tool for the development of medical implants.

Particular attention has been given to TiO_2 nanoparticles, which are widely used due to their bioinertness, photocatalytic activity, and ability to enhance the corrosion and mechanical resistance of coatings [18–20]. However, growing evidence indicates potential toxicological risks associated with the migration of TiO_2 nanoparticles from coatings into biological environments. In vivo and in vitro studies have demonstrated that nanoparticles can penetrate tissues and organs, accumulate in the liver, kidneys, and brain, and cause oxidative stress, cell membrane damage, and apoptosis [21–24]. These effects depend on the concentration, size, and degree of nanoparticle aggregation, as well as the stability of the coating in physiological media.

Recent review and experimental studies have confirmed the promising potential of MAO coatings while highlighting the need for precise control over the composition and dosage of incorporated ions. For instance, electrochemical modification of titanium with Zn, Cu, Ag, Sr, and Ce ions via MAO has been shown to enhance osteogenic, angiogenic, and antibacterial properties. However, systematic reviews emphasize the risk of uncontrolled ion release and coating instability during long-term exposure to physiological environments [25–29].

In vitro studies on cell cultures further underline the dose-dependent nature of TiO_2 toxicity: high nanoparticle concentrations can induce oxidative stress, DNA damage, and cell cycle disruptions, particularly in three-dimensional models that mimic in vivo conditions. This highlights the increased cellular sensitivity to nanoparticle dosage and morphology and underscores the need for a comprehensive analysis of both the physicochemical and biological properties of such coatings [30, 31].

Despite the widespread use of TiO_2-modified coatings in implantology, the mechanisms underlying their potential cytotoxicity at different nanoparticle concentrations remain unclear. A comprehensive study, combining physicochemical characterization and biological testing, is required to assess coating stability and safety for living cells.

The aim of this work is to provide a systematic evaluation of the influence of TiO_2 nanoparticle concentration in the MAO electrolyte on the morphology, phase composition, corrosion resistance, and cytotoxicity of calcium–phosphate coatings formed on titanium. The findings of this study are expected to help define optimal MAO processing conditions that ensure a balance between mechanical and corrosion stability and biological safety, which is essential for the development of next-generation implantable medical devices.

Materials and methods of experiments

Commercially pure titanium (grade VT1-0) samples with dimensions of 10×10×3 mm were used in this study. Prior to treatment, the sample surfaces were subjected to mechanical grinding, ultrasonic cleaning in ethanol, rinsing with deionized water, and sandblasting to remove the native oxide layer and level the surface. Calcium–phosphate coatings were produced by micro-arc oxidation (MAO) in an aqueous electrolyte containing 30 % phosphoric acid (H_3PO_4), 60 g L^{-1} hydroxyapatite (HA), and 90 g L^{-1} calcium carbonate ($CaCO_3$). To investigate the effect of TiO_2 nanoparticle concentration, two electrolyte compositions were prepared, containing 0.5 % and 1 % TiO_2 nanoparticles, respectively. Samples obtained under these conditions are hereafter designated as MAO 1 (0.5 % TiO_2) and MAO 2 (1 % TiO_2). In addition to the TiO_2-containing coatings, a control PEO coating was prepared in the same calcium–phosphate electrolyte without TiO_2 nanoparticles (denoted MAO 0) to provide a reference for comparison of the morphological and physicochemical properties. We used commercial titanium (IV) oxide nanopowder (anatase phase) purchased from Aldrich (catalogue No. 637254-50G, Lot No. MKCN0838). According to the manufacturer's specifications, the particles have an average size of <25 nm, a purity of 99.7 %, and the crystalline phase is anatase. The base electrolyte for micro-arc oxidation was a calcium–phosphate solution consisting of 30 % H_3PO_4, 60 g L^{-1} hydroxyapatite, and 90 g L^{-1} $CaCO_3$. For the MAO 1 and MAO 2 samples, this same calcium–

phosphate electrolyte was used, with the only difference being the addition of 0.5 wt.% or 1 wt.% of the TiO_2 nanopowder described above. The MAO process was performed using a KP-HI-F-40A600V pulsed power supply under the following parameters: voltage — 300 V, processing time — 600 s, frequency — 200 Hz, duty cycle — 15 %, and current density — 0.23–0.35 A/cm^2. After treatment, the samples were rinsed with deionized water and dried at room temperature.

The surface morphology and elemental composition of the coatings were analyzed using a Tescan scanning electron microscope equipped with an energy-dispersive spectroscopy (EDS) detector. Phase composition was determined by X-ray diffraction (X'Pert PRO, PANalytical, Almelo, The Netherlands). Porosity and average pore size were quantified based on SEM images using the ImageJ software.

Corrosion resistance was evaluated by potentiodynamic polarization using a CS350M potentiostat-galvanostat (Corrtest Instruments) with a flat-type corrosion cell (model CS936) in a standard three-electrode configuration. The working electrode was a coated or uncoated sample with an exposed area of 1 cm^2. A saturated Ag/AgCl electrode served as the reference, and a platinum mesh was used as the counter electrode. Tests were conducted in two media: 3.5 wt.% NaCl and Ringer's solution at 25 °C. Prior to polarization, the open-circuit potential (OCP) was stabilized for 30 min. The potential sweep was carried out from −0.25 V to 0.00 V versus Ag/AgCl at a scan rate of 0.5 mV/s. The open surface porosity and pore size were quantified from plan-view SEM micrographs in ImageJ. After scale calibration images were segmented (Otsu threshold) with watershed separation; edge-touching features and objects < 2 μm were excluded. For each condition, 5 random fields of view were analyzed; the results are reported as mean ± SD. Static water contact angles were measured using a goniometer SDA-100 contact goniometer (Qchaida, Dongguan, China, sessile-drop method (3 μL), at 23 ± 1 °C.

Tribological tests were performed using an Anton Paar TRB3 tribometer in a ball-on-disk configuration in Ringer's solution. As the counterbody, we used a 6 mm silicon–nitride (Si_3N_4) ceramic ball, supplied with the instrument, with an applied load of 2 N and a sliding distance of 100 m. The friction coefficient was recorded in real time. Si_3N_4 was chosen because it is chemically inert and does not corrode in Ringer's solution, allowing the tribological response of the coating itself to be evaluated without interference from the counterbody.

For cytotoxicity evaluation, 10 samples were prepared (5 from each coating group). The study was carried out using the HOS human osteosarcoma cell line in accordance with ISO 10993-5 [32]. The cell concentration was 10^5 cells/mL in culture medium (90 % DMEM, 10 % FBS, antibiotics, and L-glutamine). Samples were incubated with the cell culture for 24 h at 37 °C, 5 % CO_2, and 100 % humidity. A culture without samples served as the control. After incubation, samples were removed, and 0.5 % MTT solution (NeoFroxx, Germany) was added and incubated for an additional 4 h, followed by dissolution of the formazan crystals in 10 % dodecyl sulfate in 0.01 M HCl. Optical density was measured using a Multiskan FC spectrophotometer (Thermo Fisher Scientific, China) at 540 nm with a 630 nm reference. The cytotoxicity index (CI, %) was calculated using the following formula:

$$\mathrm{CI}\ (\%) = (K - O) / K \times 100\ \% \qquad (1)$$

where K is the absorbance of the control and O is the absorbance of the sample. Samples were considered non-cytotoxic when CI ≤ 30 %. Macro- and microscopic images of the surfaces before and after the experiments were taken using a Canon Power Shot A630 digital camera and an ADF I350 inverted metallographic microscope after staining fixed cells with a mixture of Azure II and eosin. Statistical analysis was performed in RStudio (R) using the Shapiro-Wilk test (with Royston's correction), Welch's ANOVA, the Brunner-Munzel test, and Games-Howell multiple comparisons, with a significance level of $p < 0.05$. Prior to cell contact, specimens were rinsed 3× with deionized water (and PBS), then air-dried; after MAO, all samples were rinsed and dried as described.

Results of the research

Surface Morphology of MAO Coatings

Figure 1 presents the surface morphology of the coatings produced in electrolytes with different TiO_2 nanoparticle contents. The MAO 0 surface, obtained without nanoparticle addition, exhibits the typical micro-arc oxidation (MAO) morphology: a porous layer with rounded discharge craters of various sizes and relatively smooth, dense pore walls. When 0.5 wt.% TiO_2 nanoparticles are introduced into the electrolyte (MAO 1, Figure 1*b*), the coating retains the characteristic MAO structure but shows a slightly denser arrangement of pores and more uniform pore distribution. Increasing the nanoparticle concentration to 1 wt.%

produces a surface with reduced total open porosity and partial closure of some discharge channels; the large craters remain but their number is lower, indicating a more compact oxide layer. XRD analysis confirms the presence of TiO_2 signals in both MAO 1 and MAO 2 coatings, demonstrating that the TiO_2 nanoparticles become incorporated into the MAO layer during plasma-electrolytic oxidation. The amount of incorporated TiO_2 increases with the nanoparticle content in the electrolyte, but no qualitative difference in the type of incorporated phase is observed. Thus, the main effect of increasing TiO_2 concentration is a denser, less porous microstructure with a higher level of TiO_2 incorporation, which can influence the subsequent corrosion resistance and biological response.

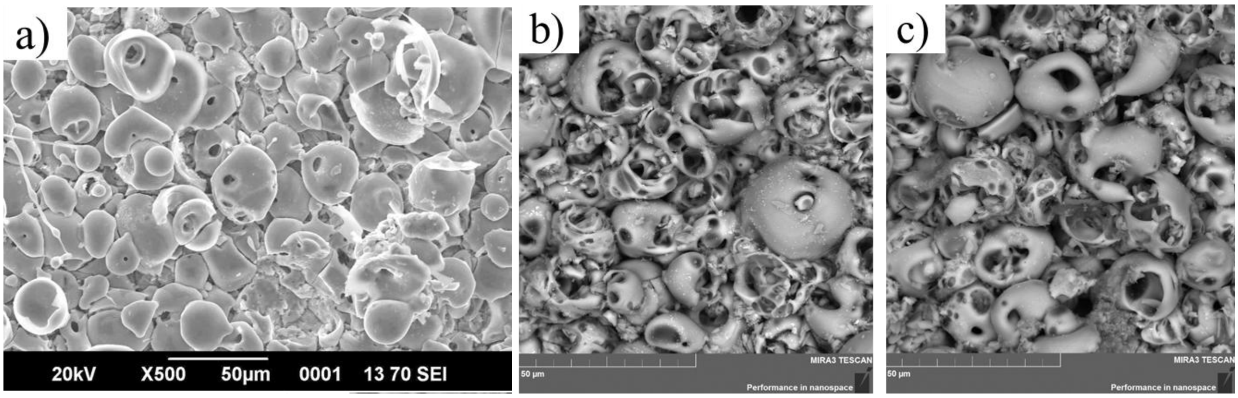

(*a*) MAO 0 — coating formed in the calcium–phosphate electrolyte without TiO_2 nanoparticles,
(*b*) MAO 1 — coating formed with 0.5 wt.% TiO_2, (*c*) MAO 2 — coating formed with 1 wt.% TiO_2

Figure 1. Surface SEM images of the coatings

Phase Composition

Figure 2 presents the X-ray diffraction (XRD) patterns of the untreated titanium surface and the MAO coatings produced with different TiO_2 nanoparticle concentrations.

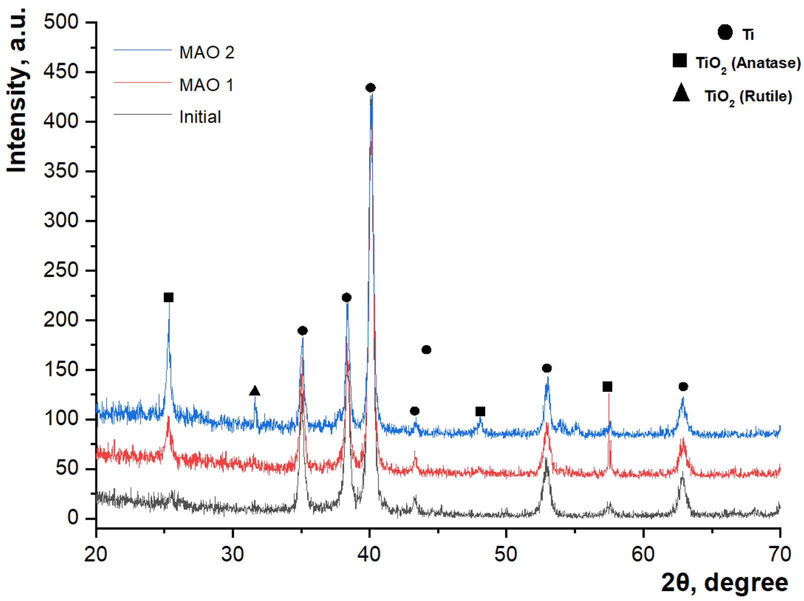

Figure 2. X-ray diffraction patterns of initial titanium and coatings containing TiO_2

For the uncoated titanium substrate, characteristic diffraction peaks of α-Ti are observed at $2\theta \approx 35°$, 38°, 40°, 53°, and 63°, corresponding to the hexagonal close-packed crystal structure of metallic titanium. After MAO treatment, additional diffraction peaks appear for both coating types (MAO 1 and MAO 2), which can be attributed to titanium dioxide phases. Distinct peaks of anatase TiO_2 are detected at approximately $2\theta \approx 25°$, 37°, 48°, and 55°, while rutile peaks are observed to a lesser extent near $2\theta \approx 27°$. This indicates the formation of an oxide film with a mixed polymorphic composition. Increasing the TiO_2 nanoparticle concentration in the electrolyte (MAO 2) results in a higher intensity of both anatase and rutile peaks compared to MAO 1, suggesting a greater amount of crystalline TiO_2 phases in the coating [33, 34]. The metallic titanium peaks remain visible, which is attributed to partial penetration of the X-ray beam through the porous coating layer to the underlying substrate. Thus, a higher TiO_2 nanoparticle content promotes the formation of a coating with enhanced crystallinity and enrichment in the anatase and rutile phases.

Porosity and Pore Size

In aqueous electrolytes, such particles can form loose agglomerates of several hundred nanometers, which is typical for unmodified TiO_2 suspensions in near-neutral or weakly alkaline solutions [35]. During micro-arc oxidation, the local plasma micro-discharges reach transient temperatures of 2000–10,000 K, but the residence time of individual nanoparticles in the discharge channel is extremely short (micro- to milliseconds) and rapid quenching occurs [36]. Numerous studies have shown that TiO_2 nanoparticles do not melt completely; instead, they become partially sintered and are incorporated into the growing calcium–phosphate/TiO_2 oxide layer as crystalline anatase/rutile phases [37]. Our own XRD and EDS analyses (Figures 2 and 12) confirm the presence of anatase and rutile peaks in the final coating, demonstrating that TiO_2 nanoparticles survive the MAO process and are embedded within the oxide matrix rather than being dissolved or lost.

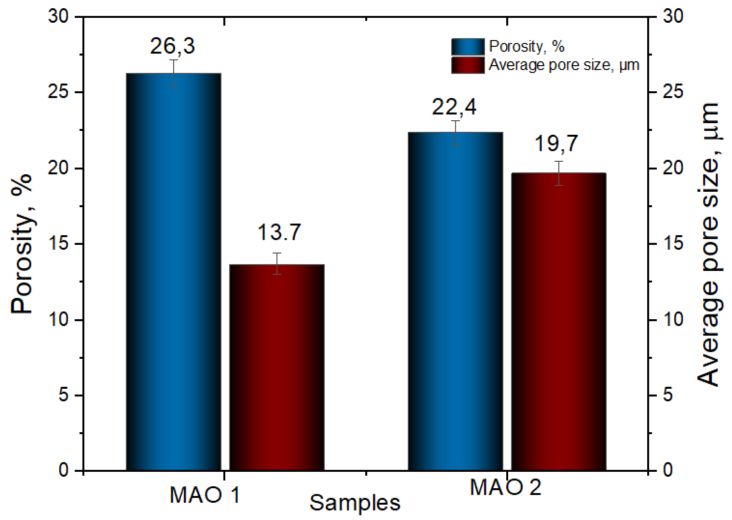

Figure 3. Porosity and average pore size of MAO coatings formed with different TiO_2 nanoparticle concentrations

Figure 3 presents the porosity and average pore-size values of the coatings. For the MAO 1 sample, the total open surface porosity is 26.3 %, with an average pore size of 22.4 μm. Increasing the TiO_2 nanoparticle concentration to 1 % (MAO 2) reduces the open porosity to 13.7 %, while the mean pore size decreases only slightly to 19.7 μm. SEM observations (Fig. 1) show that a few large discharge craters remain visible on MAO 2, but their areal density is lower, so that the overall mean pore diameter is marginally smaller. The reduction in open porosity is attributed to a more intense micro-arc oxidation process and the consequent densification of the oxide layer, which leads to partial closure of discharge channels [38–40]. Although high porosity can facilitate osseointegration by increasing the surface area available for cell attachment, excessive porosity may compromise corrosion resistance and mechanical strength. Thus, a TiO_2 nanoparticle concentration of 1 % promotes the formation of a denser coating with potentially improved structural stability while maintaining the characteristic MAO surface morphology.

Coating Thickness (Cross-Sectional SEM)

Cross-sectional SEM micrographs (Fig. 4) reveal the typical duplex MAO structure with a porous outer layer and a dense inner barrier layer. The coating thickness, determined from three independent measurements on each sample, is about 72±8 μm for MAO 1 and about 123±5 μm for MAO 2. Although no statistical analysis was performed, these values clearly indicate that the coating obtained with 1 wt.% TiO_2 is markedly thicker than the one produced with 0.5 wt.% TiO_2. The increase in thickness can be attributed to the higher density and energy of micro-discharges in the electrolyte with a larger amount of TiO_2 nanoparticles, which accelerates oxide growth and promotes the formation of a thicker porous layer.

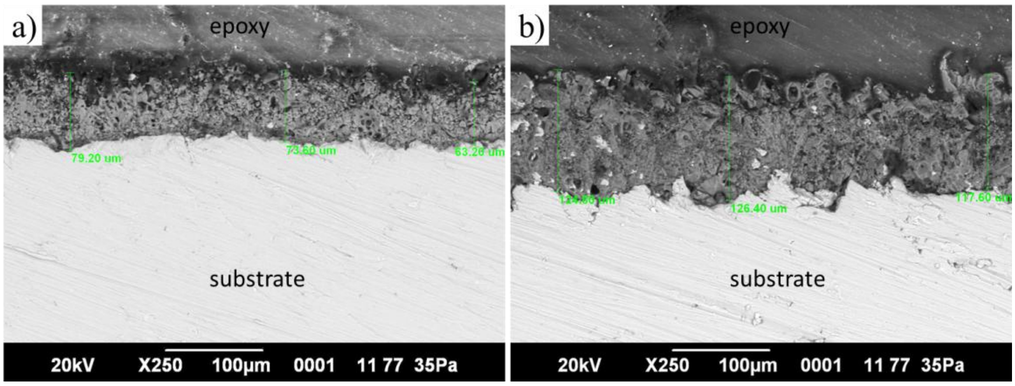

Figure 4. SEM cross-section images of MAO coatings: (*a*) MAO 1, (*b*) MAO 2

A similar increase in coating thickness with a higher TiO_2 content in the electrolyte was also noted in the works [41, 42], where it was shown that TiO_2 nanoparticles increase the conductivity of the electrolyte, enhance the energy of microdischarges and accelerate the growth of the oxide layer.

Surface Roughness

The surface roughness (Ra) values obtained from contact profilometry shown in Figure 5. The untreated titanium surface exhibits an average roughness of 3.55±1.5 µm, which reflects the initial sand-blasted preparation. The TiO_2-free MAO coating (MAO 0) shows a comparable Ra of 3.96±1.2 µm, indicating that the micro-arc oxidation process without nanoparticle additives does not substantially change the macro-scale roughness. In contrast, incorporation of TiO_2 nanoparticles leads to a slight but measurable decrease: MAO 1 — 3.05±0.4 µm and MAO 2 — 2.98±0.7 µm. This trend is consistent with the SEM observations (Figure 1), where the coatings containing nanoparticles display partial closure of large discharge channels and a denser surface. A lower Ra can improve the uniformity of cell attachment while maintaining the characteristic porous microstructure required for osseointegration.

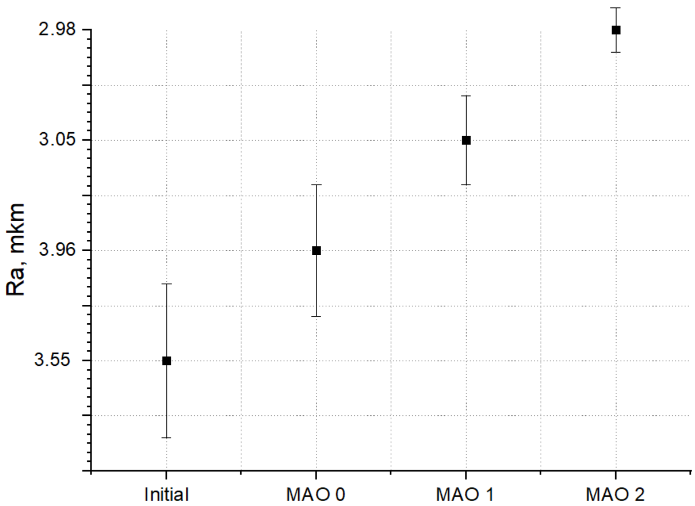

Figure 5. Surface roughness profiles of the tested samples

Corrosion Behavior

The anodic polarization curves (Fig. 6) demonstrate clear differences in the corrosion behavior of bare titanium and MAO-coated samples. In 3.5 wt.% NaCl solution (Figure 6*a*), the corrosion current density (Icorr) of untreated titanium is 1.48×10^{-5} A cm^{-2}, whereas MAO 1 and MAO 2 show markedly lower values of 3.50×10^{-6} A cm^{-2} and 8.89×10^{-6} A cm^{-2}, respectively. Both coatings also exhibit a positive shift of the corrosion potential, indicating a slowdown of anodic dissolution processes. Among them, the MAO 2 coating provides the most pronounced improvement in the chloride medium. In Ringer's solution (Figure 6*b*), the absolute Icorr values for all samples are lower, reflecting the formation of a protective passive TiO_2 film promoted by the calcium- and phosphate-containing ions of the medium: 2.27×10^{-6} A cm^{-2} for bare titanium, 9.68×10^{-7} A cm^{-2} for MAO 1, and 1.13×10^{-5} A cm^{-2} for MAO 2. Owing to this strong spontaneous passivation, the untreated titanium shows a slightly lower Icorr than the MAO coatings. This effect is well known for titanium in simulated body fluids and represents a temporary passivation phenomenon rather than superior long-term protection. Importantly, in the more aggressive chloride environment (NaCl), the MAO coatings, particularly MAO 2, still provide markedly better protection than bare titanium. The superior corrosion performance of MAO 2 compared with MAO 1 can be attributed to its lower open porosity (13.7 % vs. 26.3 %), which limits the penetration of aggressive ions, and to the higher crystallinity of the oxide layer with an increased content of stable TiO_2 phases [43, 44].

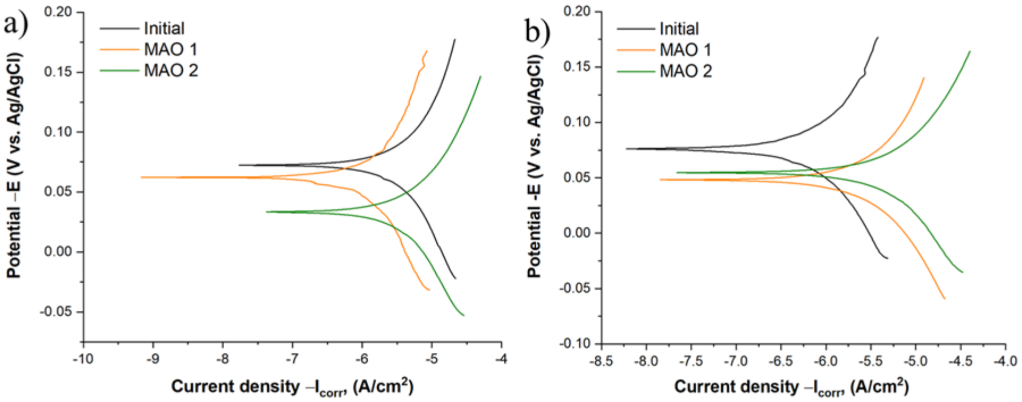

Figure 6. Polarization curves of the samples: (*a*) in 3.5 wt.% NaCl solution; (*b*) in Ringer's solution

Tribological Performance

Figure 7 shows the evolution of the friction coefficient (μ) during ball-on-disk sliding in Ringer's solution.

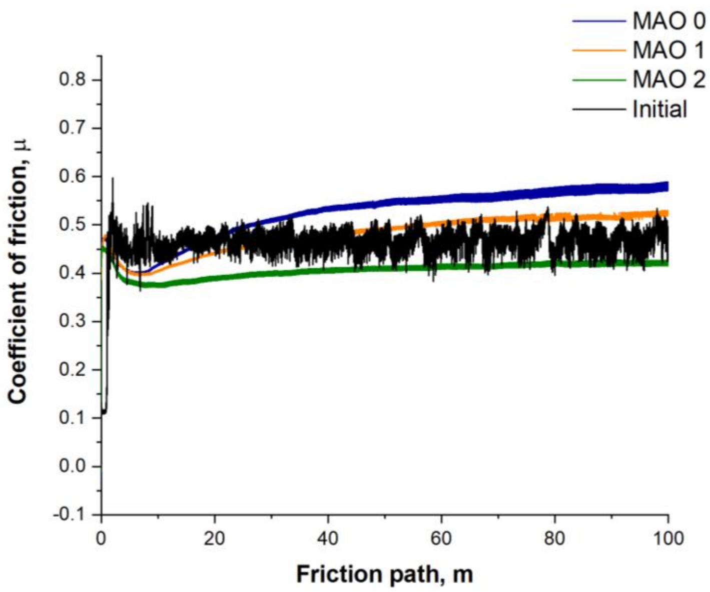

Figure 7. Tribological test results

All samples display an initial running-in stage with a rapid rise in μ, followed by a quasi-steady regime. The untreated titanium and the MAO 0 coating (formed without TiO_2 nanoparticles) exhibit the highest steady-state friction coefficients, stabilizing at about 0.55–0.60 and 0.50–0.55, respectively. For the TiO_2-containing coatings the friction levels are lower overall: MAO 1 reaches approximately 0.46–0.50, while

MAO 2 remains in the range 0.38–0.42 throughout the test. It should be noted that, at longer sliding distances, the μ value of MAO 1 slightly exceeds that of the untreated reference, which we have now stated explicitly; this reflects the combined effect of its relatively high open porosity and the formation of a stable tribolayer rather than any measurement artifact. The progressive reduction of μ from MAO 0 to MAO 2 correlates with the decrease in open surface porosity and the more compact microstructure (Fig. 3), which favor better retention of the lubricating medium and reduce adhesive interactions with the Si_3N_4 counterbody. Thus, the incorporation of TiO_2 nanoparticles, particularly at 1 wt.%, results in coatings with improved tribological behavior compared to both untreated titanium and MAO 0.

In the revised manuscript, Figure 8 presents SEM micrographs of the wear tracks formed after tribological tests in Ringer's solution. The width of the wear scars is approximately 1.2–1.4 mm for all coatings. The MAO 0 surface shows a relatively rough track with visible micro-grooves, typical of abrasive wear. In contrast, MAO 1 and MAO 2 coatings exhibit smoother tracks without signs of delamination, indicating that the oxide layer remained stable under sliding conditions. The MAO 2 sample demonstrates a slightly more compact and uniform wear zone, which correlates with its denser surface structure and lower friction coefficient.

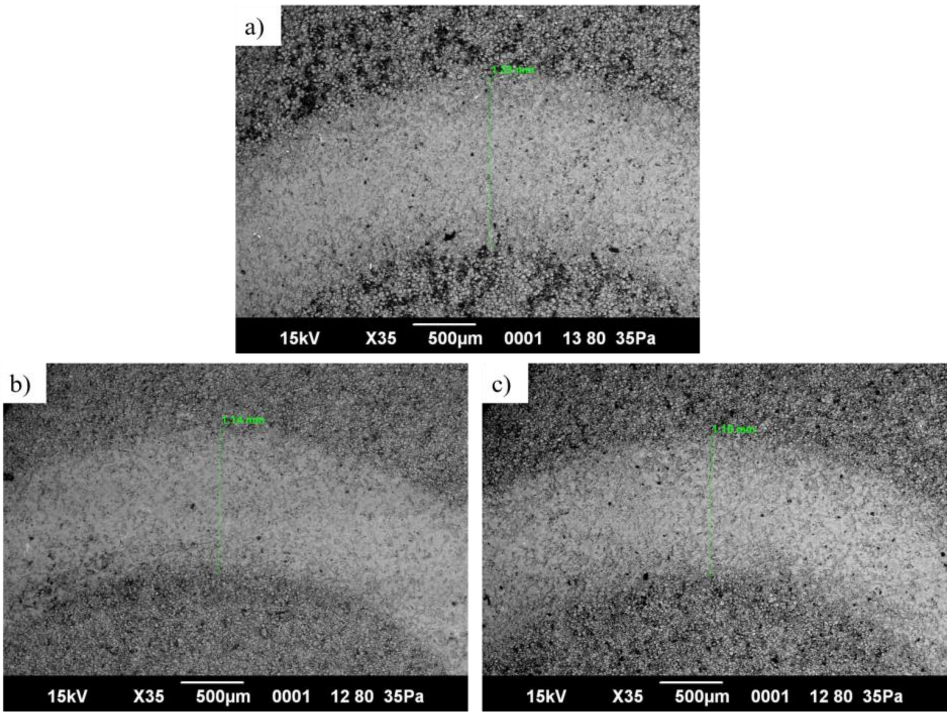

Figure 8. SEM images of wear tracks on the coatings after tribological testing in Ringer's solution: (*a*) MAO; (*b*) MAO 1; (*c*) MAO 2

Wettability (Water Contact Angle)

Figure 9 shows the static water contact angles of the investigated surfaces. The untreated titanium exhibits a contact angle of 68.0°, corresponding to a weakly hydrophilic surface. After micro-arc oxidation without TiO_2 (MAO 0) the contact angle decreases to 52.0°, and further to 47.2° for MAO 1 (0.5 wt.% TiO_2), indicating a more pronounced hydrophilic character. This trend correlates with the higher surface porosity and the moderately rough topography revealed by SEM and profilometry (Table 1), which favor the capillary penetration of water and thus enhance wetting. For MAO 2 (1 wt.% TiO_2), the contact angle slightly increases to 60.3°, remaining within the hydrophilic range (<90°). The small rise compared with MAO 1 can be related to the lower open porosity (13.7 % vs. 26.3 %) and the denser outer layer, which reduce the capillary effect despite similar Ra values. Overall, all coatings remain hydrophilic, a surface property known to be beneficial for early cell adhesion and subsequent osseointegration of implant materials [45]. All coatings remain hydrophilic (<90°), which is favorable for early cell adhesion.

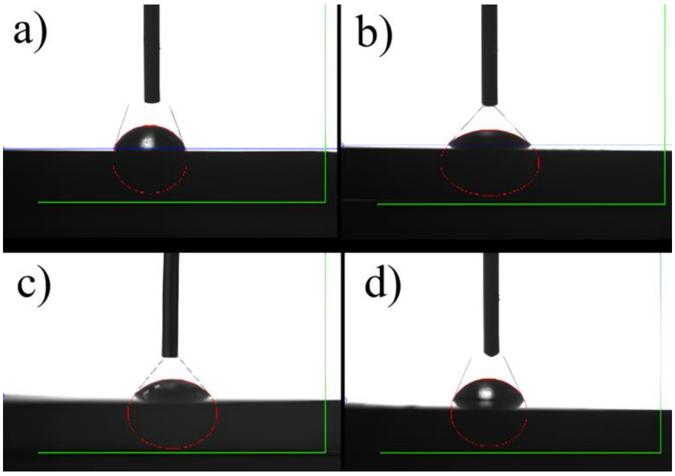

Figure 9. Water contact angle images of the tested surfaces: (*a*) initial, (*b*) MAO 0, (*c*) MAO 1, (*d*) MAO 2

Cytotoxicity and Surface Stability in Cell Culture

In this study, dark-field light microscopy was employed to assess the microrelief of the coating surfaces before and after thermal sterilization, as well as to analyze the uniformity and structural changes induced by technological treatments. Reflective dark-field microscopy of the samples (Fig. 10) revealed a pronounced microrelief typical of calcium–phosphate coatings formed by the micro-arc oxidation process, consisting of bright spherulitic structures and darker surface depressions.

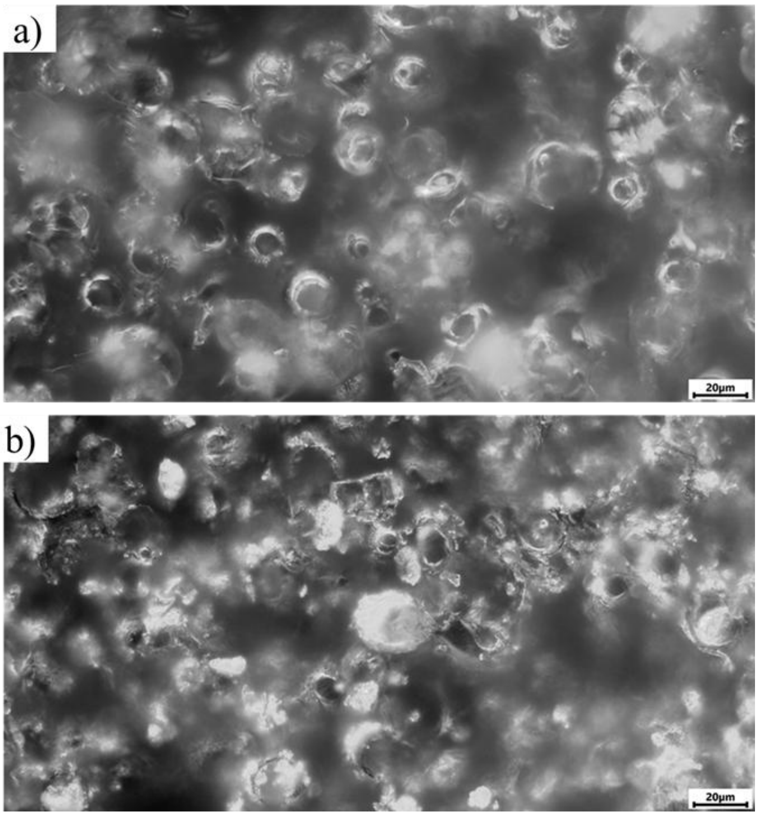

Figure 10. Microscopic appearance of the sample surfaces before dry-heat sterilization (dark-field light microscopy), magnification ×500; (*a*) sample No. 31 from the MAO 1 group; (*b*) sample No. 21 from the MAO 2 group

After sterilization at 160 °C for 60 min (prior to contact with the liquid cell culture), no additional surface integrity changes (such as cracks or delamination of structural elements) were observed. However, when the sterile samples were placed in the cell suspension, yellowing of the culture medium was noticeable in the MAO 2 group (Fig. 11). Only sample No. 25 displayed a medium color similar to that of the control group (cells without samples, K1 for comparison) and the MAO 1 test group (sample No. 35 for comparison). In addition, a white amorphous, flake-like precipitate formed at the bottom of the test tubes containing samples No. 21–24 (MAO 2 group), which was absent in the control tubes and in tubes containing samples No. 25 and No. 35. Synthetic cell culture media have their own buffering systems that protect against pH fluctuations. The yellowing observed in group 2 indicates acidification of the medium caused by chemical products released from the samples (e.g., detachment of structural coating elements or residual products of the micro-arc oxidation process that were not fully removed during sample preparation). pH fluctuations of ±1 unit from the neutral range (7.0–7.4) indicate that the sample did not pass sanitary-chemical suitability tests for potential implant use. Therefore, samples from the MAO 2 group may subsequently demonstrate excessive cytotoxicity in the MTT assay.

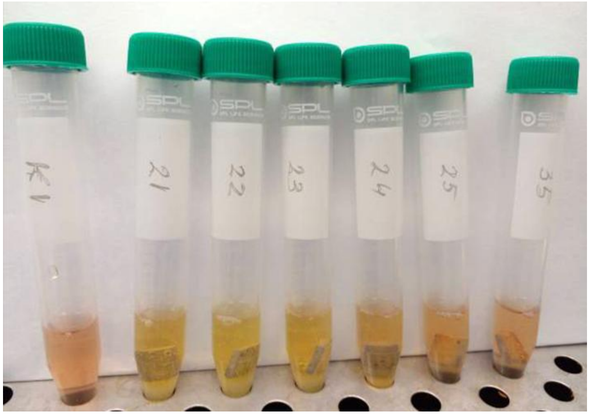

Figure 11. Change in the color of the culture medium immediately after adding samples from the MAO 2 group (Nos. 21–24)

In this context, it should be noted that after contact with the cell culture, coating defects were observed on both sides of the MAO 2 samples, particularly along the edges, which may indicate partial dissolution of the coating and precipitation of its components into the medium (Fig. 10). In the MAO 1 group, this effect was much less pronounced. Edge defects of MAO coatings have been reported in the literature in cases of excessive coating dissolution and are presumably associated with “stress concentrators.” The condition of a normal distribution of sample characteristics was not met; therefore, a nonparametric test was used to compare the results between the MAO 1 and MAO 2 groups. Verification according to Section 2.1.1 of the PI guidelines (Table 1) showed that the median cytotoxicity index (CI) in the MAO 2 group significantly exceeded the 30 % in vitro cytotoxicity threshold recommended by ISO 10993-5, reaching 81 % cell death compared to the control. In contrast, the MAO 1 group had a median CI of 3 % (Table 2), indicating the non-cytotoxic nature of the samples in this group. Statistically significant differences (p<0.001) in the median CI values were identified between the two groups (Table 3).

Table 1

Verification of MTT test results for the normal distribution of variables in the studied samples

Group	Shapiro–Wilk Test with Royston’s Correction	Normal Distribution Law of the Variable
MAO 1	SW = 0.94, p = 0.13	yes
MAO 2	SW = 0.66, p < 0.001	no

Table 2

Intergroup comparison of MTT test results in the studied samples

Group	Cytotoxicity Index Values, % of Control, Me (Q1; Q3)	Pairwise Comparison, Brunner–Munzel Test
MAO 1	3 (−2; 10)	Brunner–Munzel Test Statistic = 17.63 p < 0.001
MAO 2	81 (76; 84)	

Thus, the MAO 2 group samples exhibit a significant cytotoxic effect (>30 % relative to control) on the in vitro culture of HOS human osteosarcoma cells under direct short-term contact for 24 h. The results presented in Tables 3 and 4 indicate that the cytotoxic effect in the MAO 1 group varies around zero. Notably, sample No. 32 demonstrates statistically significant differences from the other samples in this group, showing a cytoprotective effect (enhanced cell viability).

Table 3

Intragroup comparison of MTT test results among samples within the MAO 1 group

Group	Cytotoxicity Index Values, % of Control (X ± SD)	Multiple Comparison, Welch's ANOVA	Pairwise Comparison, Games–Howell Test
Sample 31	10 ± 7	F = 7.21 $p = 0.0054$*	$p_{31–32} = 0.0067$* $p_{31–33} = 0.99$ $p_{31–34} = 0.28$ $p_{31–35} = 0.99$ $p_{32–33} = 0.0091$* $p_{32–34} = 0.099$ $p_{32–35} = 0.0095$ $p_{33–34} = 0.39$ $p_{33–35} = 0.99$ $p_{34–35} = 0.41$
Sample 32	−15.80 ± 8.82		
Sample 33	8.80 ± 7.19		
Sample 34	−0.2 ± 7.82		
Sample 35	8.6 ± 7.16		

* *n* — sample size (number of measurement replicates); the intragroup distribution of the variable was consistent with normality according to the Shapiro–Wilk test with Royston's correction.

In turn, with the exception of sample No. 25 (CI = 11.8 %), the remaining four samples showed CI values in the range of 77.0 %–90.8 % (Table 4), which is 2.5–3 times higher than the threshold level recommended by ISO 10993-5 (not exceeding 30 %).

Table 4

Intragroup comparison of MTT test results among samples within the MAO 2 group

Group	*n*	Cytotoxicity Index Values, % of Control (X ± SD)	Multiple Comparison, Welch's ANOVA	Pairwise Comparison, Games–Howell Test
Sample 21	5	80.60 ± 1.67	F = 201.47 $p < 0.001$*	$p_{21–22} < 0.001$* $p_{21–23} = 0.042$* $p_{21–24} = 0.071$ $p_{21–25} < 0.001$* $p_{22–23} < 0.001$* $p_{22–24} < 0.001$* $p_{22–25} < 0.001$* $p_{23–24} = 0.0014$* $p_{23–25} < 0.001$* $p_{24–25} < 0.001$*
Sample 22	5	90.80 ± 0.84		
Sample 23	5	84 ± 1.23		
Sample 24	5	77 ± 1.87		
Sample 25	5	11.80 ± 6.61		

* *n* — sample size (number of measurement replicates); the intragroup distribution of the variable was consistent with normality according to the Shapiro–Wilk test with Royston's correction.

Microscopic imaging of the sample surfaces after Azure II/eosin staining was used to visualize HOS cells adhered to the coatings (Fig. 12). Because of the irregular microrelief and variable depth of the MAO surface it was not possible to obtain sharply focused micrographs at all sites, even at low magnification (×200). Nevertheless, representative low-magnification images of the MAO 1 group (Fig. 12*a*) show multiple scattered stained areas corresponding in size to individual cells. Examination of several fields of view at higher magnification (×500) confirmed the presence of cell nuclei-like structures in these stained regions (Fig. 12*b*). For the MAO 2 group (Fig. 12*c*), stained elements were also found, but in repeated fields the overall number of attached cells was lower than on MAO 1, even though the single representative image shows two stained spots. The lower apparent count in the selected micrographs should therefore be interpreted qualitatively; the conclusion of higher cell adhesion on MAO 1 is based on observation of multiple areas rather than only the frames shown.

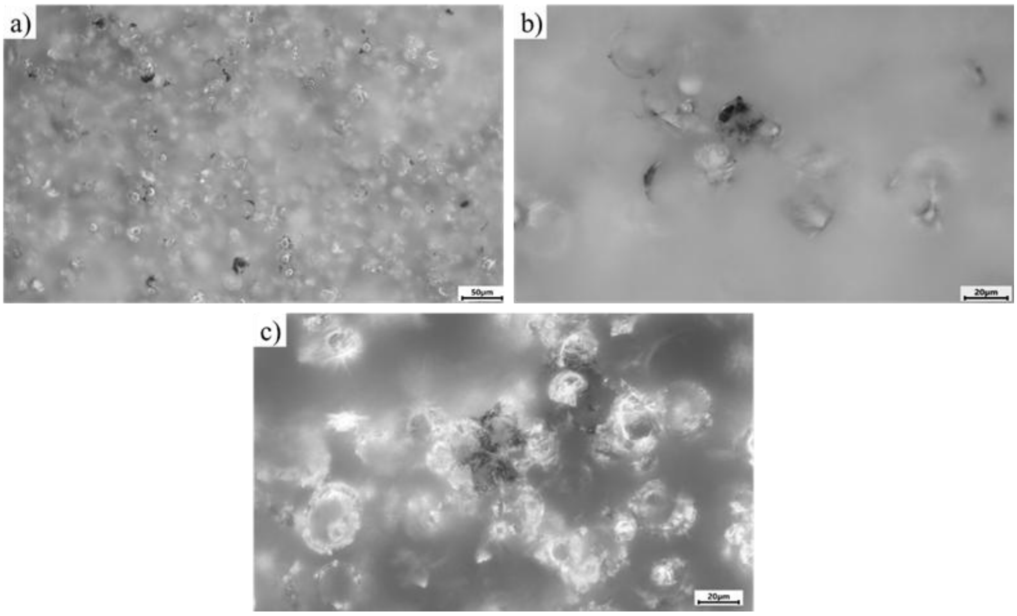

(*a*) MAO 1 No. 33, dark-field, ×200: numerous stained regions corresponding in size to individual cells are visible across the surface; (*b*) MAO 1, bright-field, ×500: single stained element showing a cell-nucleus-like structure; (*c*) MAO 2 No. 22, dark-field, ×500: representative view with two stained elements

Figure 12. Microscopic appearance of sample surfaces after 24 h contact with HOS cells and Azure II/eosin staining

Figure 12 presents the SEM results of the samples after cytotoxicity testing. For the MAO 1 group samples (Fig. 12*a*, *b*), the surface largely retains its original coating structure with minimal signs of degradation. The morphology remains relatively stable, with individual areas showing adhered cellular elements, confirming the low cytotoxicity of the coating and its ability to support cell adhesion. No significant dissolution or delamination of the coating was observed. In contrast, the MAO 2 group samples (Fig. 12*c*, *d*) exhibit more pronounced coating degradation, including localized dissolution, the appearance of microcracks, and areas where structural elements have delaminated. Some regions display residual decomposition products of the coating, likely released into the culture medium, correlating with the color change observed at the early stages of the experiment (Fig. 11). Such surface alterations indicate coating instability and potential release of particles or ions that may cause toxic effects on cells [46–50].

The higher cytotoxicity observed for the MAO 2 coating containing 1 wt.% TiO_2 may be related to several factors. First, a higher TiO_2 concentration can alter the electrolyte chemistry during coating growth and subsequently affect the surface stability in the biological medium. Partial leaching of Ti and P ions and local pH fluctuations may occur, leading to unfavorable conditions for cell viability. In addition, the increased discharge energy and the formation of a thicker, more porous layer can promote partial structural degradation and enhanced release of reaction products into the culture medium. Similar effects were reported by other authors for oxide coatings obtained at high nanoparticle concentrations.

EDS elemental mapping and spectra (Fig. 13) confirm the presence of titanium, calcium, phosphorus, oxygen, and trace amounts of carbon in both coatings. In the MAO 1 sample (non-cytotoxic coating), the distribution of calcium and phosphorus remains relatively uniform across the surface, and the overall composition shows minimal changes after contact with the cell culture. This indicates good chemical stability of the coating and low release of degradation products into the surrounding medium, correlating with the absence of cytotoxic effects. In contrast, the MAO 2 sample exhibits decreased phosphorus and calcium signals accompanied by an increased titanium and oxygen contribution, suggesting partial dissolution of the calcium–phosphate layer and exposure of the underlying titanium oxide phase. These compositional changes are consistent with the previously observed yellowing of the culture medium and the higher cytotoxicity index (>30 %). Thus, coatings formed with 0.5 % TiO_2 nanoparticles (MAO 1) demonstrate better chemical stability and biocompatibility compared to coatings formed with 1 % TiO_2 (MAO 2).

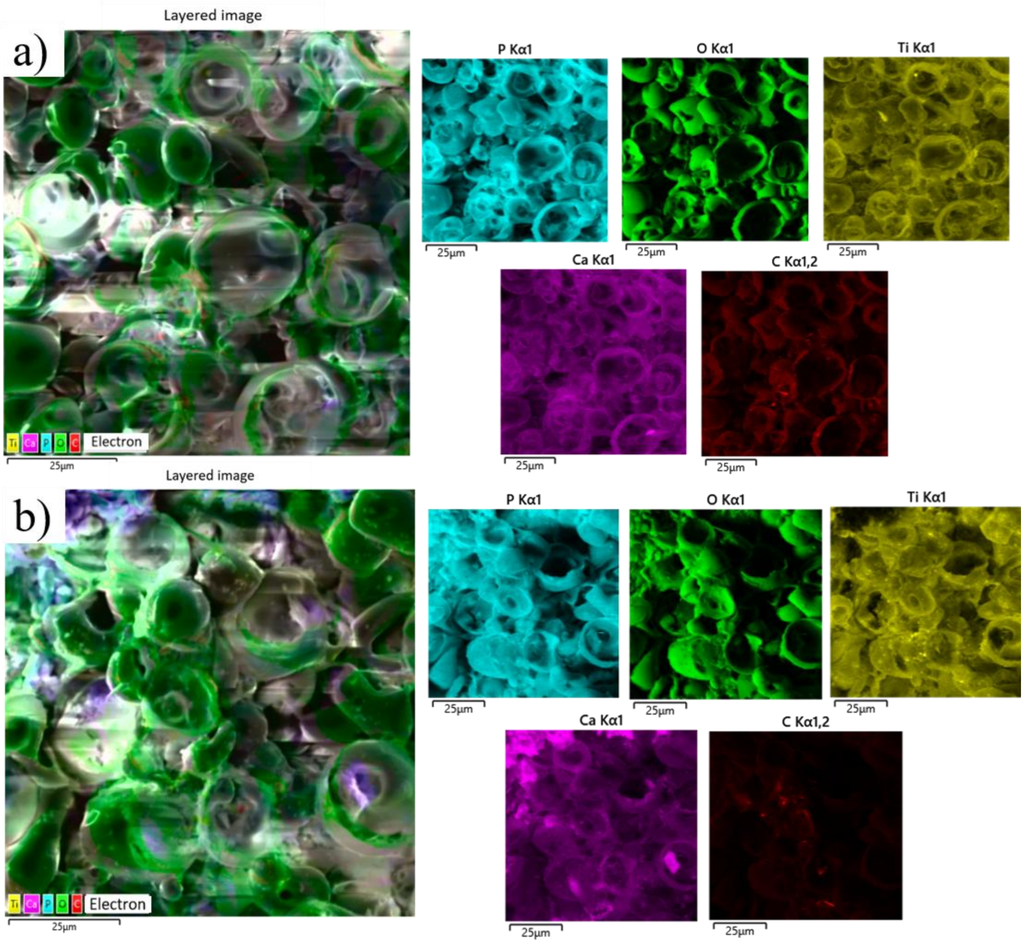

Figure 13. EDS analysis of MAO coatings after cytotoxicity testing: (*a*) MAO 1; (*b*) MAO 2

Table 5 summarizes the elemental composition of the coatings obtained from EDS mapping. Both coatings consist primarily of oxygen, phosphorus, and calcium, confirming the formation of a calcium–phosphate–titania layer. The titanium content is about 10.17 wt.% in MAO 1 and 7.24 wt.% in MAO 2, indicating that TiO_2 nanoparticles are successfully incorporated into the oxide layer. The slightly lower Ti content at 1 wt.% TiO_2 addition is consistent with the thicker Ca–P-rich outer layer and agrees with the XRD identification of anatase and rutile phases. These EDS results, together with the XRD and SEM analyses, confirm the presence and stable incorporation of TiO_2 nanoparticles in the MAO coatings.

Table 5

Elemental composition (EDS, weight %) of the MAO coatings

Element MAO 1	Weight, %	Element MAO 2	Weight, %
O	38.24	O	41.72
P	30.12	P	23.68
Ti	10.17	Ti	7.24
Ca	15.31	Ca	20.18
C	6.16	C	7.18

The observed differences between coatings produced with 0.5 and 1 wt.% TiO_2 nanoparticles can be explained by the influence of nanoparticle concentration on the micro-arc discharge behavior and the kinetics of oxide growth. TiO_2 nanoparticles in the electrolyte act as additional charge carriers and heterogeneous nucleation sites, which modify the breakdown voltage and increase the density and energy of micro-discharges [51]. At a higher nanoparticle content (1 wt.%), the higher discharge energy promotes more intense local melting and resolidification of the oxide, leading to partial closure of discharge channels and formation of a denser, more crystalline TiO_2-containing layer. Conversely, at 0.5 wt.%, the lower concentration of particles results in a more open, highly porous structure with larger areal density of discharge craters. These microstructural changes directly affect the corrosion behavior, tribological performance, and cytotoxicity of the coatings.

Conclusion

This study demonstrated that the incorporation of TiO_2 nanoparticles into the electrolyte during micro-arc oxidation significantly affects the morphology, phase composition, and functional characteristics of calcium–phosphate coatings formed on titanium. Both coatings exhibited a typical duplex structure with a porous outer layer and a dense inner barrier layer. Increasing the TiO_2 content from 0.5 wt.% to 1 wt.% resulted in a thicker coating (from 72±8 μm to 123±5 μm) and a higher proportion of anatase and rutile phases, which influenced the mechanical and electrochemical performance.

The coating produced with 0.5 wt.% TiO_2 (MAO 1) demonstrated a uniform microstructure, improved corrosion resistance, and the absence of cytotoxic effects, making it the most balanced composition in terms of protective and biological performance. In contrast, the coating with 1 wt.% TiO_2 (MAO 2) exhibited partial degradation and elevated cytotoxicity, likely caused by pH changes and ion release into the biological medium.

The developed coatings show strong potential for application on biomedical titanium implants, particularly for orthopedic and dental devices, where corrosion stability, surface bioactivity, and cell compatibility are critical. The MAO 1 coating, in particular, may serve as a bioactive and corrosion-resistant layer that enhances implant longevity and integration with bone tissue.

Future research will focus on long-term in vitro and in vivo testing to evaluate the coatings' osteogenic properties and biological stability, as well as on optimizing the MAO parameters and electrolyte composition to achieve an improved balance between coating thickness, porosity, and bioactivity. Additional attention will be given to ion-leaching behavior, mechanical fatigue resistance, and coating adhesion under dynamic physiological conditions to ensure the reliability of these coatings in real biomedical applications.

Funding

This research has been funded by the Committee of Science of the Ministry of Science and Higher Education of the Republic of Kazakhstan (Grant No. BR24992862).

References

1 Akshaya, S., Rowlo, P.K., Dukle, A., & Nathanael, A.J. (2022). Antibacterial coatings for titanium implants: Recent trends and future perspectives. *Antibiotics, 11,* 1719. https://doi.org/10.3390/antibiotics11121719

2 Besisa, N.H.A., & Yajima, T. (2024). Titanium-Based Alloys: Classification and Diverse. *Titanium-Based Alloys — Characterization and Applications,* 125.

3 Spriano, S., Yamaguchi, S., Baino, F., & Ferraris, S. (2018). A critical review of multifunctional titanium surfaces: New frontiers for improving osseointegration and host response, avoiding bacteria contamination. *Acta Biomaterialia, 79,* 1–22. https://doi.org/10.1016/j.actbio.2018.08.013

4 Liu, Z., Liu, X., & Ramakrishna, S. (2021). Surface engineering of biomaterials in orthopedic and dental implants: Strategies to improve osteointegration, bacteriostatic and bactericidal activities. *Biotechnology Journal, Vol. 16,* 2000116. https://doi.org/10.1002/biot.202000116

5 Kengesbekov, A.B., Serikbaykyzy, A., Bayandinova, M.B., Batanov E.E., Bazarov N.E., & Askhatov A.N. (2025). Development of biocompatible coatings for orthopedic joint implants. *Physical Sciences and Technology, 12,* 84–94. https://doi.org/10.26577/phst20251218

6 Ben Arbia, M., Helal, H., & Comini, E. (2024). Recent advances in low-dimensional metal oxides via sol-gel method for gas detection. *Nanomaterials, 14,* 359. https://doi.org/10.3390/nano14040359

7 Prasad, K.N., Syed, I., & Subbu, S.K. (2022). Laser dimple texturing — applications, process, challenges, and recent developments: A review. *Australian Journal of Mechanical Engineering, 20,* 316–331. https://doi.org/10.1080/14484846.2019.1705533

8 Roccaforte, F., Giannazzo, F., & Greco, G. (2022). Ion implantation doping in silicon carbide and gallium nitride electronic devices. *Micro, 2,* 23–53. https://doi.org/10.3390/micro2010002

9 Xie, J., Zhang, C., & Waite, T.D. (2022). Hydroxyl radicals in anodic oxidation systems: Generation, identification and quantification. *Water Research, 217,* 118425. https://doi.org/10.1016/j.watres.2022.118425

10 Xue, T., Attarilar, S., Liu, S., Liu, J., Song, X., Li, L., & Tang, Y. (2020). Surface modification techniques of titanium and its alloys to functionally optimize their biomedical properties: Thematic review. *Frontiers in Bioengineering and Biotechnology, 8,* 603072. https://doi.org/10.3389/fbioe.2020.603072

11 Alontseva, D., Safarova, Y., Voinarovych, S., Obrosov, A., Yamanoglu, R., Khoshnaw, F., & Weiß, S. (2024). Biocompatibility and corrosion of microplasma-sprayed titanium and tantalum coatings versus titanium alloy. *Coatings, 14,* 206. https://doi.org/10.3390/coatings14020206

12 Zhang, Z.Y., Huang, T.Y., Zhai, D.J., Wang, H.B., Feng, K.Q., & Xiang, L. (2022). Study on strontium doped bioactive coatings on titanium alloys surfaces by micro-arc oxidation. *Surface and Coatings Technology, 451,* 129045. https://doi.org/10.1016/j.surfcoat.2022.129045

13 Wen, X., Liu, Y., Xi, F., Zhang, X., & Kang, Y. (2023). Micro-arc oxidation (MAO) and its potential for improving the performance of titanium implants in biomedical applications. *Frontiers in Bioengineering and Biotechnology, 11,* 1282590. https://doi.org/10.3389/fbioe.2023.1282590

14 Wang, R., Ni, S., Ma, L., & Li, M. (2022). Porous construction and surface modification of titanium-based materials for osteogenesis: A review. *Frontiers in Bioengineering and Biotechnology, 10,* 973297. https://doi.org/10.3389/fbioe.2022.973297

15 Manisekaran, R., Chettiar, A.D.R., Marasamy, L., Arthikala, M.K., Kandasamy, G., Ibarra, V.C., & Rathore, H.S. (2025). Copper, Zinc, and Titanium-Based Semiconductor Nanomaterials for Antimicrobial Coatings and Their Mechanisms. *Nano Select, 6,* e202400155. https://doi.org/10.1002/nano.202400155

16 Rezić, I., & Meštrović, E. (2023). Characterization of nanoparticles in antimicrobial coatings for medical applications — a review. *Coatings, 13,* 1830. https://doi.org/10.3390/coatings13111830

17 Parham, S., Wicaksono, D.H., Bagherbaigi, S., Lee, S.L., & Nur, H. (2016). Antimicrobial treatment of different metal oxide nanoparticles: A critical review. *Journal of the Chinese Chemical Society, 63,* 385–393. https://doi.org/10.1002/jccs.201500446

18 Vera, M.L., Traid, H.D., Dwojak, A.N., Rosenberger, M.R., & Schvezov, C.E. (2023). Advances in nanostructured TiO_2 coatings for industrial applications. In *Industrial Applications of Nanoparticles* (pp. 228–255). CRC Press: Boca Raton, FL, USA. https://doi.org/10.1201/9781003183525

19 Rakhadilov, B., Zhassulan, A., Ormanbekov, K., Shynarbek, A., Baizhan, D., & Aldabergenova, T. (2024). Surface modification and tribological performance of calcium phosphate coatings with TiO_2 nanoparticles on VT1-0 titanium by micro-arc oxidation. *Crystals, 14,* 945. https://doi.org/10.3390/cryst14110945

20 Kengesbekov, A., Sagdoldina, Z., Torebek, K., Baizhan, D., Kambarov, Y., Yermolenko, M., & Maulet, M. (2022). Synthesis and formation mechanism of metal oxide compounds. *Coatings, 12,* 1511. https://doi.org/10.3390/coatings12101511

21 Abbasi-Oshaghi, E., Mirzaei, F., & Pourjafar, M. (2019). NLRP3 inflammasome, oxidative stress, and apoptosis induced in the intestine and liver of rats treated with titanium dioxide nanoparticles: In vivo and in vitro study. *International Journal of Nanomedicine, 14,* 1919–1936. https://doi.org/10.2147/IJN.S192382

22 Kumar, V., Sharma, N., & Maitra, S.S. (2017). In vitro and in vivo toxicity assessment of nanoparticles. *International Nano Letters, 7,* 243–256. https://doi.org/10.1007/s40089-017-0221-3

23 Ajdary, M., Moosavi, M.A., Rahmati, M., Falahati, M., Mahboubi, M., Mandegary, A., & Varma, R.S. (2018). Health concerns of various nanoparticles: A review of their in vitro and in vivo toxicity. *Nanomaterials, 8,* 634. https://doi.org/10.3390/nano8090634

24 Salama, B., Alzahrani, K.J., Alghamdi, K.S., Al-Amer, O., Hassan, K.E., Elhefny, M.A., & Fathalla, A.S. (2023). Silver nanoparticles enhance oxidative stress, inflammation, and apoptosis in liver and kidney tissues: Potential protective role of thymoquinone. *Biological Trace Element Research, 201,* 2942–2954. https://doi.org/10.1007/s12011-022-03399-w

25 Zhang, X., Zhou, W., Xi, W. (2024). Advancements in incorporating metal ions onto the surface of biomedical titanium and its alloys via micro-arc oxidation: A research review. *Frontiers in Chemistry, 12,* 1353950. https://doi.org/10.3389/fchem.2024.1353950

26 Xu, N., Fu, J., Zhao, L., Chu, P.K., & Huo, K. (2020). Biofunctional elements incorporated nano/microstructured coatings on titanium implants with enhanced osteogenic and antibacterial performance. *Advanced Healthcare Materials, 9,* 2000681. https://doi.org/10.1002/adhm.202000681

27 Ming, X., Wu, Y., Zhang, Z., & Li, Y. (2023). Micro-arc oxidation in titanium and its alloys: Development and potential of implants. *Coatings, 13,* 2064. https://doi.org/10.3390/coatings13122064

28 Rakhadilov, B., Zhassulan, A., Baizhan, D., Shynarbek, A., Ormanbekov, K., & Aldabergenova, T. (2024). The effect of the electrolyte composition on the microstructure and properties of coatings formed on a titanium substrate by microarc oxidation. AIMS *Materials Science, 11,* 547–564. https://doi.org/10.3934/matersci.2024027

29 Bayatanova, L.B., Zhassulankyzy, A.Z., Magazov, N.M., Rakhadilov, B.K., Muktanova, N., & Uazyrkhanova, G.K. (2023). Effect of plasma-electrolytic oxidation on mechanical properties of titanium coatings. *Bulletin of the University of Karaganda-Physics, 111,* 65–74. https://doi.org/10.31489/2023ph3/65-74

30 Kashin, A.D., Sedelnikova, M.B., Uvarkin, P.V., Ugodchikova, A.V., Luginin, N.A., Sharkeev, Y.P., & Bakina, O.V. (2023). Functionalizing diatomite-based micro-arc coatings for orthopedic implants: Influence of TiO_2 addition. *Biomimetics, 8,* 280. https://doi.org/10.3390/biomimetics8030280

31 Makurat-Kasprolewicz, B., Wekwejt, M., Ronowska, A., Gajowiec, G., Grodzicka, M., Dzionk, S., & Ossowska, A. (2024). Influence of ultrasound on the characteristics of CaP coatings generated via the micro-arc oxidation process in relation to biomedical engineering. *ACS Biomaterials Science & Engineering, 10,* 2100–2115. https://doi.org/10.1021/acsbiomaterials.3c01433

32 (2009). ISO 10993-5. Biological Evaluation of Medical Devices — Part 5: Tests for *In Vitro* Cytotoxicity. Geneva: International Organization for Standardization.

33 Wang, P., Wei, X.W., Cao, W.J., Tang, Y.T., Wang, Y., Gong, Z.Y., & Zu, X.T. (2019). Effect of TiO_2 nanoparticles on the characteristics of MAO coatings. *International Journal of Electrochemical Science, 14,* 9311–9325. https://doi.org/10.20964/2019.09.67

34 Woo, S.R., & Sung, Y.M. (2016). Enhanced photoelectrochemical water splitting of micro-arc oxidized TiO_2 via anatase/rutile phase control and nitrogen doping. *Journal of the Electrochemical Society, 163,* H278. https://doi.org/10.1149/2.0471605jes

35 Yerokhin, A.L., Nie, X., Leyland, A., & Matthews, A. (2000). Characterization of oxide films produced by plasma electrolytic oxidation of a Ti–6Al–4V alloy. *Surface and Coatings Technology, 130,* 195–206. https://doi.org/10.1016/S0257-8972(00)00719-2

36 Ceriani, F., Casanova, L., Massimini, L., Brenna, A., & Ormellese, M. (2023). TiO_2 microparticles incorporation in coatings produced by plasma electrolytic oxidation (PEO) on Titanium. *Coatings*, *13,* 1718. https://doi.org/10.3390/coatings13101718

37 Erfanifar, E., Aliofkhazraei, M., Nabavi, H.F., & Rouhaghdam, A.S. (2017). Growth kinetics and morphology of microarc oxidation coating on titanium. *Surface and Coatings Technology, 315,* 567–576. https://doi.org/10.1016/j.surfcoat.2017.03.002

38 Zhang, P., Zuo, Y., & Nie, G. (2020). The pore structure and properties of microarc oxidation films on 2024 aluminum alloy prepared in electrolytes with oxide nanoparticles. *Journal of Alloys and Compounds, 816,* 152520. https://doi.org/10.1016/j.jallcom.2019.152520

39 Jin, F., Chu, P.K., Tong, H., & Zhao, J. (2006). Improvement of surface porosity and properties of alumina films by incorporation of Fe micrograins in micro-arc oxidation. *Applied Surface Science, Vol. 253,* 863–868. https://doi.org/10.1016/j.apsusc.2006.01.024

40 Li, Z., Cai, Z.B., Cui, X.J., Liu, R.R., Yang, Z.B., & Zhu, M.H. (2021). Influence of nanoparticle additions on structure and fretting corrosion behavior of micro-arc oxidation coatings on zirconium alloy. *Surface and Coatings Technology, Vol. 410,* 126949. https://doi.org/10.1016/j.surfcoat.2021.126949

41 Bayatanova, A.M., Rakhadilov, B.K., & Abizhanova, I.K., et al. (2023). Effect of plasma-electrolytic oxidation on mechanical and corrosion properties of titanium coatings with TiO_2 nanoparticles. *Bulletin of the University of Karaganda-Physics, 3*(111), 54–61. https://doi.org/10.31489/2023ph3/65-74

42 Molaei, M., Bahrololoom, M.E., & Heshmati-Manesh, S., et al. (2022). Incorporating TiO_2 nanoparticles to enhance corrosion resistance and bioactivity of micro-arc oxidized titanium coatings. *Ceramics International, 48, 15,* 22021–22031. DOI: 10.1016/j.ceramint.2022.06.149

43 Kumar, K., Bhadauria, S.S., & Singh, A.P. (2023). Effect of post-coating heat treatment on corrosion and stress corrosion behaviors of NiCr/TiO_2-coated 316L stainless steel. *Arabian Journal of Science and Engineering, 48,* 3893–3908. https://doi.org/10.1007/s13369-022-07310-6

44 Chen, X.W., Song, H., Pu, H., Zheng, R., Zhang, M., & Zhang, D. (2024). Study of wear and corrosion resistance of ATO nanoparticle–doped micro-arc oxide film layers. *International Journal of Applied Ceramic Technology, 21,* 1078–1093. https://doi.org/10.1111/ijac.14599

45 Steel, J.P. (1927). The treatment of certain mental diseases by Ringer-Locke solution. *British Medical Journal, 2,* 1177. https://doi.org/10.1136/bmj.2.3494.1177

46 Suthar, J.K., Rakesh, B., Vaidya, A., & Ravindran, S. (2023). Comprehensive analysis of titanium oxide nanoparticle size and surface properties on neuronal PC-12 cells: Unraveling cytotoxicity, dopaminergic gene expression, and acetylcholinesterase inhibition. *Journal of Xenobiotics, 13,* 662–684. https://doi.org/10.3390/jox13040043

47 Line, F.C. (2023). Titanium dioxide nanoparticle (TiO_2 NP) induces toxic effects on LA-9 mouse fibroblast cell line. *Cellular Physiology and Biochemistry, 57,* 63–81. https://doi.org/10.33594/000000616

48 Mohammadalipour, Z., Rahmati, M., Khataee, A., & Moosavi, M.A. (2017). Different concentrations of titanium dioxide nanoparticles induce autophagy followed by growth inhibition or cell death in A375 melanoma cells. *Journal of Skin Stem Cell, 4,* e63994. https://doi.org/10.5812/jssc.63994

49 Jin, C.Y., Zhu, B.S., Wang, X.F., & Lu, Q.H. (2008). Cytotoxicity of titanium dioxide nanoparticles in mouse fibroblast cells. *Chemical Research in Toxicology, Vol. 21,* 1871–1877. https://doi.org/10.1021/tx800179f

50 Zhu, G., Wang, G., & Li, J.J. (2021). Advances in implant surface modifications to improve osseointegration. *Materials Advances, 2,* 6901–6927. https://doi.org/10.1039/D1MA00675D

51 Mamaeva, A., Kenzhegulov, A., Panichkin, A., Abdulvaliyev, R., Fischer, D., Bakhytuly, N., & Toiynbaeva, N. (2024). Influence of current duty cycle and voltage of micro-arc oxidation on the microstructure and composition of calcium phosphate coating. *Coatings, 14,* 766. https://doi.org/10.3390/coatings14060766

А.Б. Кеңесбеков, А.Ж. Жасұлан, Н. Мұқтанова,
Дарын Байжан, Е. Ахметова, А. Серікбайқызы

Титандағы PEO-кальций-фосфаты жабындарының коррозияға төзімділігін, цитоүйлесімділігін және бактерияға қарсы қасиеттерін арттыру үшін TiO_2 нанобөлшектерін енгізу

Титан және оның қорытпалары қолайлы механикалық қасиеттеріне және коррозияға төзімділігіне байланысты биомедициналық имплантацияларда кеңінен қолданылады; дегенмен, олардың табиғи бетінде жеткілікті биобелсенділік пен бактерияға қарсы қасиеттері жоқ. Микродоғалық тотығу биоактивті жабындарды өндірудің перспективалы тәсілі және TiO_2 сияқты нанобөлшектердің қосылуы олардың функционалдығын одан әрі жақсартуы мүмкін. Бұл зерттеу жабын тұрақтылығы мен биологиялық қауіпсіздікті қамтамасыз ететін микродоғалық тотығу электролитіндегі TiO_2 нанобөлшектерінің оңтайлы концентрациясын анықтауға бағытталған. Кальций-фосфатты жабындар екі TiO_2 концентрациясы бар микродоғалық тотығу арқылы коммерциялық таза титанда дайындалды: 0,5 % масса (MAO 1) және 1 % масса (MAO 2). Беттің морфологиясы, кеуектілігі және фазалық құрамы сканерлеуші электрондық микроскопия, энергия-дисперсиялық спектроскопия және рентген сәулелерінің дифракциясы арқылы талданды. Коррозияға төзімділік NaCl және Рингер ерітінділеріндегі потенциодинамикалық поляризация арқылы бағаланды, ал биоүйлесімділік HOS адам остеосаркома жасушалары мен MTT талдаулары арқылы *in vitro* арқылы бағаланды. TiO_2 мазмұнын 1 %-ға ұлғайту жабынның кеуектілігін төмендетті (MAO 1 үшін 13,7 %-ға қарсы 26,3 %), коррозиядан қорғауды жақсартты және жалаң титанмен салыстырғанда үйкеліс коэффициентін төмендетті. Дегенмен MAO 2 биологиялық ортада жоғары цитотоксикалық (81 % жасуша өлімі) және ішінара құрылымдық деградацияны көрсетті. MAO 1 тұтастығын сақтап, уытты әсерлерін көрсетпеді (3 % жасуша өлімі). Бұл нәтижелер TiO_2 0,5 %-нің коррозияға төзімділік, механикалық тұрақтылық және биоүйлесімділік арасындағы тепе-теңдікті қамтамасыз ете отырып, қауіпсіз имплант жабындарының дамуын қолдайтын оңтайлы концентрация екенін көрсетеді.

Кілт сөздер: микродоғалық тотығу, титан, TiO_2 нанобөлшектері, коррозия, биоүйлесімділік, цитотоксикалық

А.Б. Кеңесбеков, А.Ж. Жасұлан, Н. Мұқтанова,
Дарын Байжан, Е. Ахметова, А. Серікбайқызы

Включение наночастиц TiO_2 для повышения коррозионной стойкости, цитосовместимости и антибактериальных свойств ПЭО-кальций-фосфатных покрытий на титане

Титан и его сплавы широко используются в биомедицинских имплантатах благодаря своим благоприятным механическим свойствам и коррозионной стойкости. Однако их нативная поверхность не обладает достаточной биоактивностью и антибактериальными свойствами. Микродуговое оксидирование является перспективным методом получения биоактивных покрытий, а включение наночастиц, таких как TiO_2, может дополнительно повысить их функциональность. Целью данного исследования было определение оптимальной концентрации наночастиц TiO_2 в электролите для микродугового оксидирования, обеспечивающей стабильность покрытия и биологическую безопасность. Покрытия из фосфата кальция были получены на технически чистом титане методом микродугового оксидирования с двумя концентрациями TiO_2: 0,5 мас.% (MAO 1) и 1 мас.% (MAO 2). Морфологию поверхности, пористость и фазовый состав анализировали методами сканирующей электронной микроскопии, энергодисперсионной спектроскопии и рентгеновской дифракции. Коррозионную стойкость оценивали методом потенциодинамической поляризации в растворах NaCl и Рингера, а биосовместимость — *in vitro* с использованием клеток остеосаркомы человека HOS и MTT-теста. Увеличение содержания TiO_2 на 1 % уменьшало пористость покрытия (26,3 % против 13,7 % для MAO 1), улучшало защиту от коррозии и снижало коэффициент трения по сравнению с чистым титаном. Однако MAO 2 продемонстрировал высокую цитотоксичность (81 % гибели клеток) и частичную структурную деградацию в биологических средах. MAO 1 сохранял свою целостность и не оказывал токсического действия (3 % гибели клеток). Эти результаты свидетельствуют о том, что 0,5 % TiO_2 является оптимальной концентрацией для разработки безопасных покрытий для имплантатов, обеспечивая баланс между коррозионной стойкостью, механической стабильностью и биосовместимостью.

Ключевые слова: микродуговое оксидирование, титан, наночастицы TiO_2, коррозия, биосовместимость, цитотоксичность

Information about the authors

Kengesbekov, Aidar — PhD, D. Serikbayev East Kazakhstan Technical University, Ust-Kamenogorsk, Kazakhstan; e-mail: aidar.94.01@mail.ru; ORCID ID: https://orcid.org/0000-0002-5630-9467

Zhassulan, Ainur — PhD student, Engineering Center, Shakarim University NJSC, Semey, Kazakhstan; e-mail: a.zhassulan@shakarim.kz; ORCID ID: https://orcid.org/0009-0001-5887-0135

Muktanova, Nazerke — Researcher, D. Serikbayev East Kazakhstan Technical University, Ust-Kamenogorsk, Kazakhstan; e-mail: nmuktanova@bk.ru; ORCID ID: https://orcid.org/0000-0002-4823-6640

Daryn, Baizhan — PhD student, Shakarim University NJSC, Semey, Kazakhstan; e-mail: daryn.baizhan@mail.ru; ORCID ID: https://orcid.org/0000-0002-9105-3129

Ahmetova, Elvira — Researcher, D. Serikbayev East Kazakhstan Technical University, Ust-Kamenogorsk, Kazakhstan; e-mail: elya.akhmetova.04@mail.ru ORCID ID: https://orcid.org/0009-0000-4060-1001

Serikbaikyzy, Ainur — PhD student, D. Serikbayev East Kazakhstan Technical University, Ust-Kamenogorsk, Kazakhstan; e-mail: ainura.serikbaikyzy@gmail.com; ORCID ID: https://orcid.org/0000-0003-4623-4681

Article

UDC 533.9

https://doi.org/10.31489/2026PH1/40-48

Received: 12.11.2025
Accepted: 17.12.2025

M.N. Bakirci✉

Department of Physics, Faculty of Arts and Sciences, Gaziosmanpaşa University, Tokat, Turkey

Evaluation of Relativistic Plasma Dispersion Functions Using Downward Recursion and Analytical Relations

The Dnestrovskii functions provide a powerful framework for understanding wave propagation, attenuation and instabilities in plasmas where relativistic effects dominate, as relativistic plasma dispersion functions. To calculate the Dnestrovskii functions for a wide range of parameter values, effective analytical and downward recurrence formulae are proposed in this study. These formulae allow users to make efficient calculations specific to high-energy or relativistic plasmas. Because the recurrence formulas are simple, calculating time and accuracy are improved, and the formulas are easy to use. The results obtained using the new analytical and downward recurrence formulae agree well with published results and those obtained using numerical calculation methods for a wide range of parameters.

Keywords: Dnestrovskii functions, downward recurrence relations, relativistic plasma dispersion functions, plasma physics

✉*Corresponding author*: Mustafa Numan Bakirci, numan.bakirci@gop.edu.tr

Introduction

Relativistic plasma dispersion functions (PDFs) are essential for the study of wave propagation and instabilities in high-energy plasmas. They generalize non-relativistic plasma theory to account for relativistic effects, which are critical in environments where particles approach the speed of light. These functions are highly applicable in astrophysics, fusion research and intense laser-plasma interactions [1–5]. The PDFs, often referred to as Dnestrovskii functions, are particularly applicable to high-energy or relativistic plasmas [3]. These functions are critical for analyzing the behavior of wave propagation, damping and instabilities in plasmas where particle velocities approach a significant fraction of the speed of light. The Dnestrovskii functions provide a way of describing the relativistic effects on the plasma response to electromagnetic fields and waves [1–20].

The Dnestrovskii functions are typically defined by integrals involving the relativistic particle distribution function and the wave-particle interaction terms. Although closed-form analytical expressions are rare, these functions are essential for solving wave dispersion relations in relativistic plasmas, growth rates for instabilities in both thermal and non-thermal plasmas, energy transfer between particles and waves (e.g., for Landau and cyclotron damping in relativistic plasmas) [7–10].

High energy environments such as pulsar magnetospheres, relativistic jets and accretion disks around black holes all involve relativistic plasmas where Dnestrovskii functions are used to describe the behavior of waves and instabilities. In some fusion devices, especially in advanced scenarios involving high-energy particle beams, relativistic effects become important and Dnestrovskii functions are used to analyze plasma stability and wave-particle interactions. These functions extend classical plasma theory into the relativistic regime, making them essential for the analysis of high-energy plasmas in both astrophysical and laboratory contexts [3, 4]. Numerous studies have been proposed for the evaluation of Dnestrovskii functions. These studies are widely used in applied sciences.

Dnestrovskii functions play a crucial role in describing weakly relativistic, magnetised and thermal plasmas [3, 4].These functions, together with the Shkarofsky functions, are particularly important for waves with small wave numbers that are perpendicular to the magnetic field [3]. Robinson [3, 5] has made an extensive study of these plasma dispersion functions, providing series expansions, asymptotic series, recurrence relations, integral forms and approximations.An approach to relativistic quantum plasmas, including limit cases, using covariant Wigner functions has been presented in [6]. Matroli has developed a numerical method for the calculation of the weakly relativistic Vlasov dielectric dyad in magnetised thermal plasmas [7]. Another study investigated processes and equilibria in relativistic thermal plasmas, including the effects of magnetic fields on thermal, Comptonised synchrotron emission and pair equilibria [8]. The equilibria of relativistic thermal plasmas have been studied, taking into account electron-positron creation and annihilation, and photons produced in the plasma [9]. Krivenski provided a simple and exact expression for the weakly relativistic plasma dispersion functions in terms of the Z-function to study the absorption and emission properties of a magnetized plasma [10]. The physical properties of a finite thermal plasma as a function of temperature, proton optical depth and proton density or radius were studied in [11]. A new representation of the dielectric tensor elements introduced in magnetized plasmas, including for the weakly relativistic case [12]. In addition, Robinson introduced a more general class of plasma dispersion functions for waves with arbitrary perpendicular wave numbers [3]. Xiao (1988) developed a formalism to evaluate the growth rate of electromagnetic R-mode waves in a relativistic magnetized plasma, showing that relativistic corrections reduce the wave growth rate compared to the non-relativistic approximation [13]. New results, presented by Robinson, on functions governing wave properties in non-relativistic and weakly relativistic plasmas [14]. Melrose extended this work by defining generalized Trubnikov functions for unmagnetized plasmas, deriving recursion relations to generate expressions in terms of the relativistic plasma dispersion function T(z, ρ) introduced by Godfrey et al. in 1975 [15]. Exact and moderately relativistic plasma dispersion functions for weakly relativistic, magnetized, thermal plasmas are presented in [16]. A closed set of Lorentz covariant fluid equations for relativistic magnetized plasmas, allowing for anisotropy and heat flow, derived by Hazeltine (2002). Analytical approaches to thermodynamic functions of dense, fully ionized, non-ideal electron-ion plasmas, including weakly relativistic and magnetized cases, are reviewed in [17]. Lyutikov discussed microphysical processes in magnetically dominated relativistic astrophysical plasmas, but does not mention Dnestrovskii functions [18]. The electrostatic dispersion relation in a magnetized plasma using a weakly relativistic quantum kinetic model based on the Dirac equation derived in [19]. A comprehensive review of quantum kinetic theory for modelling plasmas, including weakly relativistic, magnetized and thermal plasmas, given in [20]. The relaxation characteristics in dense plasmas have been studied from the effective potentials using the Coulomb logarithm in [21]. Mamedov not only derived upward and downward Dnestrovskii recurrence formulas, but also developed an effective formula for Dnestrovskii functions using the binomial expansion theorem, expressing them in terms of binomial coefficients and incomplete gamma functions [4]. While in most cases the relativistic plasma dispersion function does not have a simple closed-form expression, it can be computed numerically by integrating the relativistic particle distribution over velocity space, considering the appropriate relativistic dynamics. The evaluation of Dnestrovskii functions can be challenging due to their complexity and dependence on relativistic effects. These functions generally lack simple closed-form solutions, so a variety of analytical approximations, numerical integration and specialized computational methods are used to evaluate them.

In this study, the Dnestrovskii function is calculated using the downward recurrence relations and analytical formula. The new analytic formula for the Dnestrovskii function is obtained by the use of the exponential-integral function. The results obtained according to the downward recurrence relation and the analytical formula obtained are evaluated and compared with those found in the literature. It is seen that the proposed method is suitable in terms of time and accuracy of the calculations.

Recurrence and analytical relations for the Dnestrovskii functions

The Dnestrovskii functions for the integer and non-integer values of q and z are defined as follows [5],

$$F_q\left(z\right)=\frac{1}{\Gamma\left(q\right)}\int_0^{\infty}\frac{x^{q-1}e^{x}}{x+z}dx \tag{1}$$

$$F_{q+1/2}\left(z\right)=\frac{1}{\sqrt{\pi}}\int_{-\infty}^{\infty}e^{-x^2}F_q\left(z+x^2\right)dx \tag{2}$$

In the literature there is also a series representation of the Dnestrovskii functions in the following form [3],

$$F_q\left(z\right)=z^{q-1}e^{z}\Gamma\left(1-q\right)-\sum_{j=0}^{\infty}\frac{z^{j}\Gamma\left(1-q\right)}{\Gamma\left(j+2\pm q\right)} \tag{3}$$

In case the value of z is real and positive, the following equation can be obtained [3],

$$F_q(z)=\sum_{j=0}^{\infty}\frac{L_j^{(1-g)}z}{j+1} \tag{4}$$

In this study an analytical formula for the Dnestrovskii function is given using the exponential integral equation, which is given as follows,

$$F_q(z)=e^z E_q(z)\Gamma(q) \tag{5}$$

where $E_q(z)$ is an exponential integral function which is defined as follows [22],

$$E_q(z)=\int_1^{\infty}\frac{e^{-zt}}{t^q}dt \tag{6}$$

Note that the Dnestrovskii functions satisfy the following downward recurrence relations for an integer order and for a non-integer value, respectively,

$$F_q(z)=\frac{1}{z}\left[1-qF_{q+1}(z)\right] \tag{7}$$

$$F_{q+1/2}(z)=\frac{1}{z}\left[1-\left(q+1/2\right)F_{q+3/2}(z)\right] \tag{8}$$

The upward recurrence relations of the Dnestrovskii function for an integer and a non-integer value are obtained using Eq. (7) and Eq. (8) as follows,

$$F_{q+1}(z)=\frac{1}{q}\left(1-zF_q(z)\right) \tag{9}$$

$$F_{q+3/2}(z)=\frac{1}{q+1/2}\left(1-zF_{q+1/2}(z)\right) \tag{10}$$

In the case that q = 0, the Eq. (1) and Eq. (2) take on the following form, respectively,

$$F_0(z)=\frac{1}{z} \tag{11}$$

$$F_{1/2}(z)=\sqrt{\frac{\pi}{z}}e^z Erfc\left(\sqrt{z}\right) \qquad \left|Arg(z)\right|<\pi \tag{12}$$

For the special case $q=1$, Eq. (9) and Eq. (10) take the following forms

$$F_1(z)=\int_z^{\infty}\frac{e^{-t}}{t}dt=e^z E_1(z) \qquad \left|Arg(z)\right|<\pi \tag{13}$$

$$F_{3/2}(z)=2\left(1-\sqrt{\pi z}e^z Erfc\left(\sqrt{z}\right)\right) \tag{14}$$

where $E_1(z)$ is the $q=1$ case of the exponential integral function given in equation (6) and is defined as follows [21],

$$E_1(z)=\int_1^{\infty}\frac{e^{-zt}}{t}dt \tag{15}$$

and in Eq. (14) $Erfc(z)$ is referred to as the complementary error function, which is defined in [21] as,

$$Erfc(z)=\frac{2}{\sqrt{\pi}}\int_z^{\infty}e^{-t^2}dt \tag{16}$$

Results and discussion

In this study, the calculation of the Dnestrovskii function is carried out using the analytical formula and the downward recurrence relation. In addition, the results of the calculation with the formulas proposed in the literature by means of approximate methods are compared with the results obtained in the present study. New approximations have been proposed for the calculation of the Dnestrovskii functions that arise from the propagation of waves and from instabilities in high energy plasmas. Based on the downward recurrence relations and new formula obtained in this study (Eq. (5)), a program was developed to compute the Dnestrovskii functions using the Mathematica 10 programming language. Furthermore, the results of our calculations are compared with numerical and theoretical models from the literature. Given a sufficiently high value for *q*, it is possible to select any initial value. As mentioned above, all values for $F_{q+1/2}(z)$ and $F_q(z)$ functions have the same order, so we can use Eq. (10–13) as the starting point for the backwards calculation. It should also be noted that this study represents the first time in the literature that the results of calculating Eq. (2) and the downward recurrence relations are presented comparatively.

The precision of the calculation results and their accuracy are listed in Table 1, in accordance with (Eq. (5)), downward (Eq. (7)) and upward (Eq. (9)) recurrence formulas (for $F_q(z)$), the serial representation of the Dnestrovskii function (Eq. (3–4)), Mamedov's formula [4] and the Mathematica numerical integration method (Eq. (1)) for arbitrary integer and non-integer values of the *q* and *z* parameters. Table 2 shows the calculation results for arbitrary integer and non-integer values of the downward (Eq. (8)) and upward (Eq. (10)) recurrence formulas (for $F_{q+1/2}(z)$) and the numerical integration method of (Eq. (2)) for arbitrary integer and non-integer values of the parameters *q* and *z*. As can be seen from Table 1, the Eq. (5) gives results that are in good agreement and high precision with Eq. (1) for all positive and real values of q and z. On the other hand, according to the calculations, it is easy to see from the table that Eq. (7) does not give results for values of $q<z$, while Eq. (9) gives results compatible with the Eq. (1). Similarly, while Eq. (7) gives results compatible with the Eq. (1) for values of $q>z$, Eq. (9) does not give results for these values of q and z. Furthermore, this table shows that for values of $q<z$, Eq. (3) and Eq. (4) yield no results whatsoever. In the case where q is about ten times larger than z, all of the equations, except for Eq. (7), give results that agree with the Eq. (1). As can be seen in Table 1, Eq. (3) and Eq. (4), which are the serial representations of the Dnestrovskii function, provide computational results only for some limited values of q and z. The same trend is observed for the downward Eq. (7) and upward Eq. (9) recurrence relations of the Dnestrovskii function as well. The empty cells in Table 1 and Table 2 are left blank because the corresponding formulae fail to give correct results for the given values of q and z. It should also be noted that in the evaluation of the calculation results obtained in Table 2, the downward recurrence formula Eq. (7) demonstrates improved calculation accuracy when the upper limit (*N*) is chosen between 50 and 100. At these *N* values, the results obtained from the downward recurrence formula are closer to the values obtained from the Mathematica numerical integration results.

Table 2 compares the calculated results for non-integer q and z values of Eq. (8) and Eq. (10) recurrence formulae with the Mathematica numerical integration equation (Eq. (2)) calculations. According to the calculation results shown in Table 2, in cases where z is smaller than q, Eq. (8) gives no result. Eq. (8) gives a result when z is greater than eight times q, but does not give a result for $z>q$ values where this condition is not satisfied. In cases where the value of *z* is greater than 20 times the value of *q*, the downward recurrence formula Eq. (8) shows optimal performance when initiated at $N = 50$. Under these conditions, the results obtained from Eq. (8) are more consistent with the results obtained from the Mathematica numerical integral equation Eq. (2).The calculation results were evaluated for the values of *q* and *z* where both equations yield valid outputs. In these cases, the results obtained with both equations are in good agreement with the results obtained with the Mathematica numerical integral equation.

Table 1

The comparative values of the relativistic Dnestrovskii functions $F_q(z)$ for $N = 100$

q	z	Eq.(9)	Eq.(7)	Eq.(5)	Eq.(3)	Eq. (4)	Ref. [4] Eq. (14)	Mathematica numerical integration results (Eq.(1))
2,6	10,5	–	–	0.07738359185496	0.07738359319046	–	0.07740403292196	0.07738359177273
4,3	12,5	–	–	0.06036964974966	0.06036871671676	–	0.06034126851801	0.06036964975028
6,6	0,5	0.16144676029281	–	0.16144676029281	0.16144797096149	0.16144797282830	0.16144676029281	0.16144797096083
22,6	1,1	0.04395518198149	–	0.04395518198149	0.04395518198149	0.04395518199762	0.04395518198149	0.04395518199551
29,9	2,9	0.03135428198352	–	0.03135428198352	0.03135428198352	0.03135428263318	0.03135428198352	0.03135428198352
10,4	40,7	–	–	0.01964758195555	–	–	0.01964758185953	0.01964758195555
18,7	10,7	–	–	0.03474664148905	0.03475300967693	0.03474664141427	0.03444496554965	0.03474664148905
38,5	3,1	0.02446328774997	–	0.02458333183835	0.02458333183835	0.02458071572591	0.02458333183835	0.02458333183842
88,5	1,1	0.01128508276980	–	0.01128508276980	0.01128508276980	–	0.01128508276980	0.01128508276992
12,1	0,5	0.08586109345137	–	0.08586109345030	0.08586109345030	0.08586109345028	0.08586109345057	0.08586109345031
44,3	4,5	0.02087867730034	–	0.02087867730034	0.02087867730034	0.02083868126221	0.02087867730034	0.02087867730001
61,7	2,5	0.01581274164031	–	0.01581274164031	0.01581274164031	–	0.01581274164031	0.01581274164032
10,7	65,2	–	0.01319920773514	0.01319920773515	–	–	0.01319920773515	0.01319920773515
0,7	88,2	–	0.01124956878817	0.01124956878817	–	–	0.01124956878817	0.01124956878849
8,1	58,1	–	0.01513299426812	0.01513299427036	–	–	0.01513299427036	0.01513299427035
30,3	90	–	0.00832977806673	0.00832977806674	–	–	0.00832977806674	0.00832977806674
30,3	9	–	–	0.02594829066550	0.02594832874244	0.02594828422538	0.02594829040580	0.02594832874244
10,3	0,1	0.10624884726200	–	0.10624884726200	0.10624884726200	0.10624884726201	0.10624884726200	0.10624884726182
5,1	40,7	–	–	0.02188530948366	–	–	0.02188530948366	0.02188530948627
5,1	50,7	–	0.01794963288102	0.01794963143260	–	–	0.01794963143260	0.01794963143486
80,9	23,7	–	–	0.00963113191696	–	–	0.00963113191696	0.00963113193243
80,9	3,7	0.01195532365190	–	0.01195532365190	0.01195532365190	–	0.01195532365190	0.01195532367379
0,4	55,5	–	0.01789130056259	0.01789130056259	–	–	0.01789130056259	0.01789130056274
55,5	0,4	0.01821247505245	–	0.01821247505245	0.01821247505245	–	0.01821247505245	0.01821247505246
25,5	0,4	0.04013370619365	–	0.04013370619365	0.04013370619365	0.04013370632818	0.04013370619365	0.04013370619365
26,6	2,6	0.03534205349374	–	0.03534205349376	0.03534205349376	0.03534205314621	0.04013370619365	0.03534205349376
9,6	96,6	–	0.00942408325233	0.00942408325233	–	–	0.00942408325233	0.00942408325232
12,3	5,8	–	–	0.05732327768504	0.05732327768328	0.05732327800416	0.05672578677826	0.05732327768505
66,8	5,8	0.01395051136111	–	0.01395051136111	0.01395051136111	–	0.01395051136111	0.01395051136111
36,8	0,19	0.02778130570315	–	0.02778130570315	0.02778130570315	0.02778148200364	0.02778130570315	0.02778130570331
5,8	0,19	0.19853374482721		0.19856031044880	0.19856031044880	0.19856030610462	0.19856014492373	0.19856031046867
10.1	65.0	–	0.01323420640588	0.01323420640589	–	–	0.01323420640589	0.01323420640589
2.7	80	–	0.01209656583428	0.01209656583428	–	–	0.01209656583428	0.01209656580835
45	2	0.02171818885051	–	0.02171818885051	—	–	0.02171818885051	0.02171818885000
11	3	–	–	0.07552959181501	—	0.07552959189899	0.07550995055347	0.07552959178514
11.8	3	–	–	0.07129646176920	0.07129646176921	0.07129646178124	0.07130379335562	0.07129646176921
15	90	–	0.00953657711636	0.00953657711636	–	–	0.00953657711636	0.00953657711635
3.8	42	–	0.02225389874224	0.02225389874224	–	–	0.02225389874224	0.02225389874223
1.7	42	–	0.02290283961924	0.02290283961924	–	–	0.02290283961924	0.02290283961924

Table 2

The comparative values of the relativistic Dnestrovskii functions by using downward recurrence relations, $F_{q+1/2}(z)$ for $N = 100$

z	*q*	Eq. (10)	Eq. (8)	Mathematica numerical integration results (Eq.(2))
65,2	5,5	0.01415945096631	0.01415945956818	0.01415946020549
31,2	1,5	0.03062168076122	–	0.03062168043606
90,6	1,5	0.01074417463866	0.01074417463694	0.01074417401793
90,6	7,5	0.01019403295080	0.01020148444383	0.01020148477889
90,6	12,5	–	0.00971055000316	0.00971055061711
90,6	35,5	–	–	0.00794775825821
1,1	35,5	0.02806487203395	–	0.02806487252910
2,9	72,5	0.01343373410043	–	0.01343373434772
4,3	12,5	0.06219097218131	–	0.06219097408672
48,6	12,5	0.01643361558159	–	0.01642020642880
99,4	8,5	0.00944895864996	0.00927449889396	0.00927449887642
19,7	27,5	0.02144651625463	–	0.02144651245955
9,7	46,5	0.01805778324645	–	0.01805778305634
0,7	46,5	0.02163777350948	–	0.02163777340892
9,7	4,5	0.07188671251409	–	0.07188671200669
79,3	4,5	0.01194065842446	0.01194065842945	0.01194065838736
37,5	4,5	0.02386796432871	–	0.02386796430175
83,9	7,5	0.01095520717832	0.01095055813507	0.01095055849122
91,3	27,5	–	–	0.00843373526493
62,4	83,5	–	–	0.00688084291229
62,4	3,5	0.01518640814421	0.01518640814399	0.01518640803752
47,1	13,5	–	–	0.01656101572075
47,1	6,5	0.01869768084745	0.01865405371751	0.01869769133608
2,7	10,5	0.08003592842445	–	0.08044447582587
2,7	38,5	0.02483322536828	–	0.02483322945412
75,1	3,5	0.01272968856100	0.01272968865274	0.01272968861057
57	2,5	0.01659481082540	0.01659481082595	0.01659480990599

Figure 1 shows the graph of the data plotted against each other from the calculated results obtained using the Eq. (5) and the Mathematica numerical integration method for arbitrary q and z values. As can be seen from the graph, the results of the calculations obtained from the two methods are in good correlation with each other.

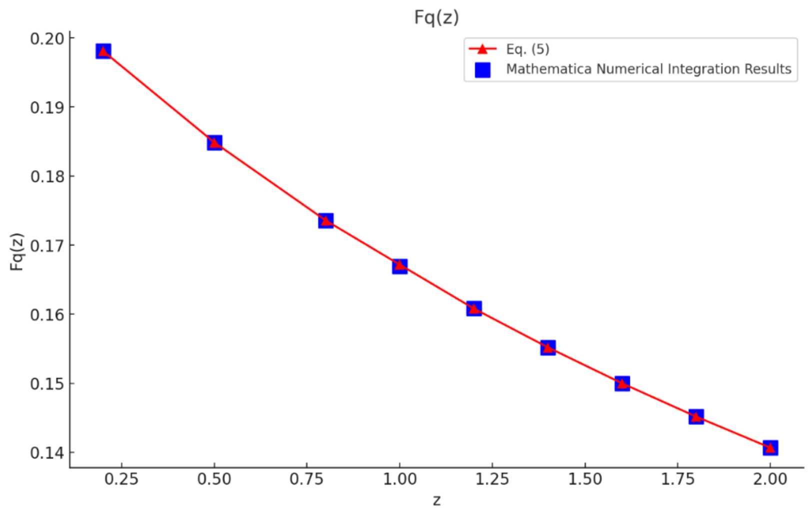

Figure 1. Correlation between Eq. (5) and Mathematica numerical integration results

Figure 2 shows 2D scatter plot that the calculation results of Eq. (5) and results of Mathematica numerical integration method are in a very good agreement. The ratio of the two sets of data to each other is centered around 1, as can be seen in the Figure 1.

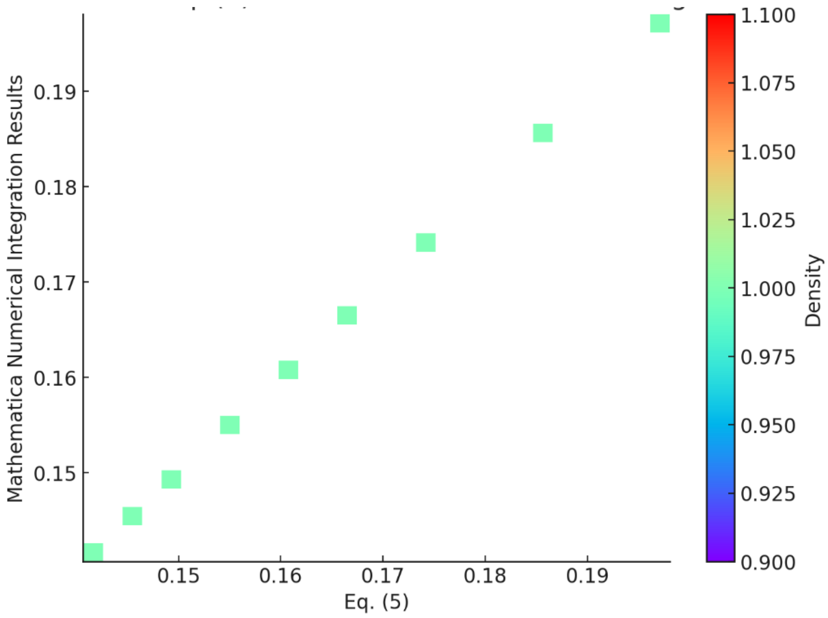

Figure 2. Comparison of the results obtained using the Eq. (5) and the Mathematica numerical integration method as a function of the parameter z for q = 5.8 and N = 100

Conclusion

The results obtained using the new formula (Eq. (5)), proposed in this study and downward recurrence formula (Eq. (7 & 8)), which allows the Dnestrovskii function to be calculated with high precision, agree very well with those obtained using the Mathematica numerical integration method. The accuracy of the proposed approaches for evaluating Dnestrovskii functions has been verified through comparison with other existing methods, demonstrating high consistency. These formulas, Eq. (5) and Eq. (7&8), provide a powerful computational framework for understanding wave propagation, damping and instabilities in plasmas where relativistic effects dominate. The performance of the Eq. (5) is better than previous ones and the formulas are easy to use.

The proposed analytical and recurrence formulas are particularly beneficial for specific plasma physics problems including: (i) wave-particle interaction calculations in fusion plasma heating scenarios, such as electron cyclotron resonance heating and radio-frequency wave absorption in tokamaks; (ii) dispersion relation analysis in astrophysical relativistic plasmas, including pulsar magnetospheres, relativistic jets, and accretion disk environments; and (iii) stability analysis and wave propagation studies in high-intensity laser-plasma interactions where weakly relativistic effects become significant. These methods provide computationally efficient alternatives to direct numerical integration, enabling faster parameter space exploration in plasma simulations.

Several constraints must be considered when applying these formulas. The downward recurrence relations (Eq. 7–8) exhibit limited parameter range validity. For integer orders, reliable results require $q>z$, while for half-integer orders, z must be approximately 8–20 times larger than q. Outside these ranges, the recurrence relations fail and numerical integration becomes necessary. The analytical formula (Eq. 5) demonstrates broader applicability but still requires careful initialization of the recurrence starting point (N = 50–100) to ensure numerical stability. Additionally, these functions are specifically designed for weakly relativistic, magnetized thermal plasmas with Maxwellian distributions, and therefore are not applicable to ultra-relativistic regimes, non-thermal particle distributions, or highly non-equilibrium plasma conditions.

References

1 Brambilla, M. (1998). *Kinetic theory of plasma waves: Homogeneous plasmas.* Oxford University Press.

2 Fried, B.D., & Conte, S.D. (1961). *The plasma dispersion function.* Academic Press.

3 Robinson, P.A. (1986). Relativistic plasma dispersion functions, *J. Math. Phys.*, *27*(5), 1206. https://doi.org/10.1063/1.527127

4 Mamedov, B.A. (2023). Analytical evaluation of the Dnestrovskii functions occurring in weakly relativistic, magnetized, and thermal plasmas. *Contrib. Plasma Phys.*, *63*(7). https://doi.org/10.1002/ctpp.202300019

5 Robinson, P.A. (1987). Relativistic plasma dispersion functions: Series, integrals, and approximation. *J. Math. Phys.*, *28*(5), 1203. https://doi.org/10.1063/1.527515

6 Hakim, R., & Heyvaerts, J. (1978). Covariant Wigner function approach for relativistic quantum plasmas. *Phys. Rev. A*, *18*(3), 1250. https://doi.org/10.1103/PhysRevA.18.1250

7 Maroli, C., & Petrillo V. (1981). Numerical calculation of the weakly relativistic dielectric dyadic for a vlasov plasma. *Phys. Scr.*, *24*(6), 955. https://doi.org/10.1088/0031-8949/24/6/008

8 Araki S., & Lightman, A.P. (1983). Relativistic Thermal Plasmas — Effects of magnetic fields. *The Astrophysical Journal*, *269*, 49. https://doi.org/10.1086/161018

9 Lightman, A.P. (1982). Relativistic thermal plasmas: pair processes and equilibria. *The Astrophysical Journal*, *253*, 842–858. https://doi.org/10.1086/159686

10 Krivenski, V., & Orefice, A. (1983). Weakly relativistic dielectric tensor and dispersion functions of a Maxwellian plasma. *Journal of Plasma Physics*, *30*(1), 125. https://doi.org/10.1017/S0022377800001045

11 Svensson, R. (1984). Steady mildly relativistic thermal plasmas: processes and properties. *Monthly Notices of the Royal Astronomical Society*, *209*(2), 175–208. https://doi.org/10.1093/mnras/209.2.175

12 Shkarofsky, I.P. (1986). New representations of dielectric tensor elements in magnetized plasma. *Journal of Plasma Physics*, *35*(2), 319. https://doi.org/10.1017/S0022377800011363

13 Xiao, F., Thorne, R.M., & Summers, D. (1998). Instability of electromagnetic R-mode waves in a relativistic plasma. *Phys. of Plasmas*, *5*(7), 2489–2497. https://doi.org/10.1063/1.872932

14 Robinson, P.A., (1989). Relativistic and nonrelativistic plasma dispersion functions. *J. Math. Phys.*, *30*(11), 2484–2487. https://doi.org/10.1063/1.528528

15 Melrose, D.B. (1999). Generalized Trubnikov functions for unmagnetized plasmas. *Journal of Plasma Physics*, *62*(2), 249. https://doi.org/10.1017/S0022377899007898

16 Swanson, D.G. (2002). Exact and moderately relativistic plasma dispersion functions. *Plasma Phys. Control. Fusion*, *44*(7), 1329. https://doi.org/10.1088/0741-3335/44/7/320

17 Potekhin, A.Y., & Chabrier, G. (2010). Thermodynamic Functions of Dense Plasmas: Analytic approximations for astrophysical applications. *Contrib. Plasma Phys.*, *50*(1), 82. https://doi.org/10.1002/ctpp.201010017

18 Lyutikov, M., & Lazarian, A. (2013). Topics in microphysics of relativistic plasmas. *Space Science Reviews*, *178*(2–4), 459. https://doi.org/10.1103/tr6y-kpc6

19 Hussain, A. et al. (2014). Weakly relativistic quantum kinetic theory for electrostatic wave modes in magnetized plasma. *Phys. Plasmas*, *21*(3), 032104. https://doi.org/10.1063/1.4867490

20 Brodin, G., & Zamanian, J. (2022). Quantum kinetic theory of plasmas. *J. Rev. Mod. Plasma Phys.*, *6*(1), 4. https://doi.org/10.1007/s41614-022-00065-5

21 Ramazanov, T.S. et al. (2020). Temperature anisotropy relaxation processes in dense plasma. *Recent Contributions to Physics*, *75*(4), 30. https://doi.org/10.26577/RCPh.2020.v75.i4.04

22 Gradshteyn, S., & Ryzhik, I.M. (1980). *Table of integrals. In series and products.* Academic Press.

М.Н. Бакирчи

Релятивистік плазманың дисперсиялық функцияларын төмен қайтарым рекурсиясы мен аналитикалық қатынастар арқылы есептеу

Днестровский функциялары релятивистік әсерлер басым болатын плазмалардағы толқындардың таралуын, әлсіреуін және тұрақсыздықтарын сипаттау үшін тиімді теориялық негіз және релятивистік плазманың дисперсиялық функциялары ретінде қолданылады. Бұл зерттеуде параметрлердің кең ауқымы үшін Днестровский функцияларын есептеуге арналған тиімді аналитикалық өрнектер мен төмен қайтарым рекурренттік формулалар ұсынылады. Ұсынылған өрнектер жоғары энергиялы және релятивистік плазмаларға тән есептеулерді жоғары тиімділікпен орындауға мүмкіндік береді. Рекурренттік формулалардың қарапайымдылығы арқасында есептеу уақыты мен дәлдігі жақсарады және формулаларды қолдану жеңілдейді. Жаңа аналитикалық және төмен қайтарым рекурренттік формулалар арқылы алынған нәтижелер параметрлердің кең аймағы үшін бұрын жарияланған нәтижелермен және сандық есептеу әдістерімен алынған нәтижелермен жақсы сәйкестік көрсетеді.

Кілт сөздер: Днестровский функциялары, төмен қайтарым рекурренттік қатынастар, релятивистік плазманың дисперсиялық функциялары, плазма физикасы

М.Н. Бакирчи

Оценка релятивистских дисперсионных функций плазмы с использованием рекуррентных формул нисходящего типа и аналитических соотношений

Функции Днестровского представляют собой эффективный теоретический аппарат для описания распространения волн, затухания и развития неустойчивостей в плазмах, где доминируют релятивистские эффекты, и выступают в качестве релятивистских дисперсионных функций плазмы. В настоящей работе предложены эффективные аналитические выражения и рекуррентные формулы нисходящего типа для вычисления функций Днестровского в широком диапазоне параметров. Данные выражения обеспечивают возможность высокоэффективных вычислений, характерных для высокоэнергетической и релятивистской плазмы. Благодаря простоте рекуррентных формул достигаются улучшенное вычислительное время и точность по сравнению с предыдущими методами, а также обеспечивается простота применения. Полученные результаты на основе предложенных аналитических выражений и рекуррентных формул нисходящего типа находятся в хорошем согласии как с опубликованными данными, так и с результатами, полученными с помощью численных методов, в широком диапазоне параметров.

Ключевые слова: функции Днестровского, рекуррентные соотношения нисходящего типа, релятивистские дисперсионные функции плазмы, физика плазмы

Information about the author

Mustafa Numan Bakirci (*corresponding author*) — Associate Professor, Doctor, Department of Physics, Faculty of Arts and Sciences, Taşlıçiftlik Campus, Tokat-Gaziosmanpaşa University, Tokat, Turkey; e-mail: numan.bakirci@gop.edu.tr; ORCID: https://orcid.org/0000-0002-5994-4853

Article

UDC 621.382: 004.3

https://doi.org/10.31489/2026PH1/49-58

Received: 12.10.2025
Accepted: 17.01.2026

N.K. Tanasheva[1], D.A. Afanasyev[1], G.A. Ranova[1]✉, L.L. Minkov[2],
A.N. Dyusembayeva[1], E.V. Sheinmaiyer[1], T.A. Rakhimgaliyev[1], M.K. Kaliaskarova[1]

[1]*Buketov Karaganda National Research University, Karaganda, Kazakhstan;*
[2]*Tomsk State University, Tomsk, Russia*

Designing and Prototyping a Microcontroller Device for Measuring the Main Parameters of Solar Panels

This article presents the results of prototyping and designing a device for measuring the basic characteristics of solar panels (photocurrent and voltage) and climatic conditions (temperature and illumination). This device is being developed to identify potential faults in the solar panel-microinverter system, as well as the causes of reduced efficiency in converting light energy into electrical energy. As a result of prototyping, a prototype of the measuring device was assembled using an Arduino Mega 2560 R3 with a W5100 Ethernet module. Current is measured by an ACS712 sensor. Voltage is measured via a voltage divider connected to the microcontroller's analog-to-digital converter input. OPT4003 light and DS18B20 temperature sensors are used. The IoT device is assembled using a RAK3172 sensor module and INA228, OPT4003, and DS18B20 microcircuits. A power module based on two IRFP460 field-effect transistors was developed to measure the solar panel's current-voltage characteristics. Software has been written for the developed prototype and the IoT device.

Keywords: IoT device, Solar panel, failure detection, microcontroller, current-voltage characteristics, operating algorithm

✉*Corresponding author*: Ranova, Gulden, guldeshka2812@gmail.com

Introduction

One of the current trends in the development of solar energy is an increase in the proportion of households using renewable energy sources [1-3]. One of the most popular sources is photovoltaic solar panels. With the development of this trend, there is a paradigm shift in the design of mini solar power stations. The use of microinverters to generate maximum solar energy from each individual solar module is increasing, as opposed to the use of an MPPT (maximum power point tracking) controller inverter, which works with several solar modules [4, 5]. Given current trends, further growth in interest in this technology can be expected.

To increase the efficiency of solar energy generation by a solar panel-MPPT controller system, it is necessary to constantly monitor the parameters of electricity generation in real-time. It is necessary to find optimal solutions between collecting a large amount of information and analysing it in real time and the minimum set of data necessary to increase the efficiency of electricity generation by solar modules.

To address this issue, scientific research is being conducted in the field of improving the electrical circuit of the MPPT controller [6], algorithms for finding the maximum power point [7, 8], and algorithms for finding possible malfunctions in solar panels [9–11]. Mathematical modelling of solar panel operation [12, 13] can be used to advance all these stages of improvement. One way to monitor the operation of the solar panel-MPPT controller system is to constantly monitor the efficiency of solar panel electricity generation. Usually, the illumination and temperature of the solar panel are monitored, and the current and voltage at the point of maximum power are determined [9, 14]. By comparing the generated electrical power with the theoretical power value obtained from the module's illumination and temperature data, the efficiency of the solar panel is predicted [14]. In the last decade, numerous studies have appeared on the use of neural networks to calculate possible malfunctions of solar panels or their shading [11, 15]. Another option for monitoring the performance of solar panels is to use the volt-ampere characteristic (VAC) of the solar panel to monitor for errors in the operation of the solar panel [11, 15].

Currently, MPPT controllers with an error diagnosis function are not commercially available. The scientific community is paying more attention to identifying more promising algorithms for finding the maximum power point [16–18]. To find faults and inaccuracies in operation, laboratory equipment [19–21] is used, which allows the characteristics of solar modules to be measured by simulating possible errors and problems. Work is also underway to create a device for monitoring solar panel malfunctions based on microcontroller devices [22] and PLC devices [23].

This paper presents the results of work on a microcontroller device for monitoring the main characteristics of solar panels in order to determine possible causes of malfunctions or reasons for a decrease in the efficiency of electricity generation by solar modules.

Materials and Methods

KZ PV 230 M60 polycrystalline silicon solar modules (from LLP "Astana Solar", Kazakhstan) were used.

A typical volt-ampere characteristic of a solar panel is shown in Figure 1, curve 1. An inverter or microinverter working with a solar panel maintains the operation of the solar panel at the maximum power point (MPP).

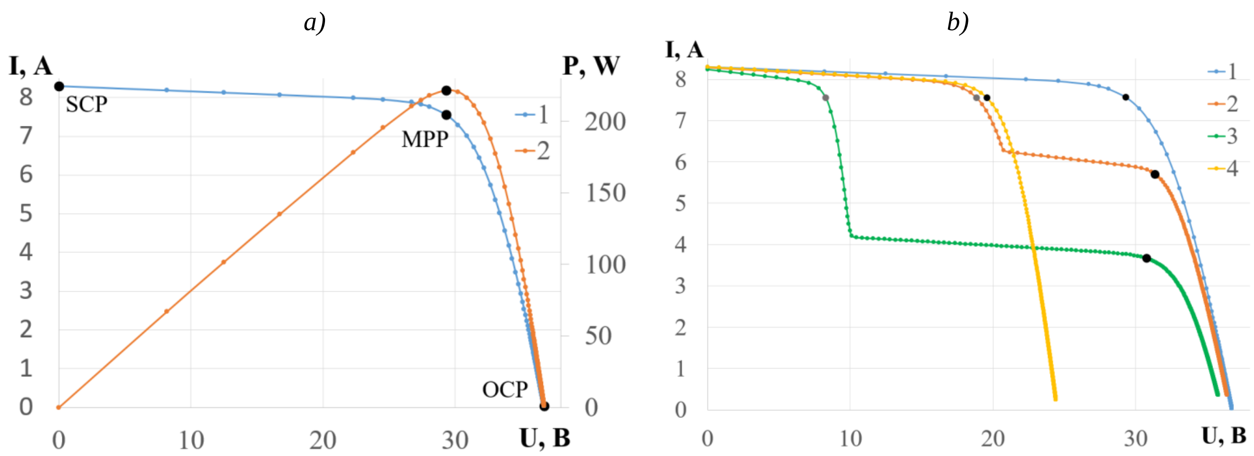

Figure 1. *a)* Standard view of the VAC (1) and volt-power characteristic (2) of the KZ PV 230 M60 solar panel at illumination Eυ = 1000 W/m² and temperature T = 25 °C: MPP — maximum power point, OCP — open-circuit point; SCP — short-circuit point. *b)* Standard view of the VAC (1), VAC of the panel with short circuit of 20 series-connected elements (2), VAC of the panel under conditions when 2 cells from different parts of the module are shaded by 50 % of the standard illumination of 1000 W/m² (3), VAC of the panel under conditions of shading of 1 cell by 25 % of the value of 1000 W/m² (4)

The VAC of a solar panel can be generally described using the formula:

$$I = I_{PV}N_{par} - I_0 N_{par}\left[\exp\left(\frac{V + R_S\left(\frac{N_{SER}}{N_{PAR}}\right)I}{V_T A N_{SER}}\right) - 1\right] - \frac{V + R_S\left(\frac{N_{SER}}{N_{PAR}}\right)I}{R_{SH}\left(\frac{N_{SER}}{N_{PAR}}\right)}, \quad (1)$$

where I_{PV} — photocurrent (A), I_0 — diode reverse saturation current (A), I — output current of the solar panel (A), V — output voltage of the solar panel (V), V_T — thermal voltage of the solar panel elements (V), A — diode ideality factor, R_S — series resistance of the solar cell (Ω), R_{SH} — shunt resistance (Ω), N_{SER} — number of series-connected cells in the module, N_{PAR} — number of parallel-connected cells in the module.

The thermal voltage of the solar panel components is determined using the formula below:

$$V_T = \frac{k(T + 273.15)}{q} \quad (2)$$

where, T — ambient temperature (°C), q — electron charge (1.106×10^{-19} C), k — Boltzmann constant (0.138×10^{-23} J/K).

In the case of the KZ PV 230 M60 panel, which contains 60 series elements and no parallel electrical circuits, formula 1 can be rewritten:

$$I = I_{PV} - I_0 \left[\exp\left(\frac{V + R_s N_S I}{V_T A N_s} \right) - 1 \right] - \frac{V + R_s N_S I}{R_{SH} N_S}. \quad (3)$$

To monitor the efficiency of power generation in a solar panel microinverter system, it is recommended to measure the voltage and current in the circuit. In operating mode, these are the voltage and current at the maximum power point (MPP) U_{max} and I_{max}. These parameters can be compared with the model parameters determined by formula (3). To use this formula, it is necessary to measure the solar panel temperature and its surface irradiance. The main solar panel parameters I_{PV}, I_0, R_S, R_{SH}, and A from formula 3 can be determined using the algorithm described in the article [24] from the parameters given in the solar panel technical specifications: U_{max} — voltage at P_{max}, I_{max} — current at P_{max}, V_{oc} — open-circuit voltage, I_{sc} — short-circuit current, α — temperature coefficient of I_{sc}, β — temperature coefficient of V_{oc}.

Previously, part of this research group implemented a project to design and manufacture a microcontroller device for playing musical melody in the presence of a person [25]. The experience gained during the implementation of this project was used in the work on this microcontroller device.

In the event of significant differences between experimental and theoretical readings, an attempt is made to determine probable faults based on the U_{max} and I_{max} values. Figure 1*a* shows the short-circuit and open-circuit points on the solar panel's VAC. These values are possible due to an electrical open-circuit or short circuit between the solar panel and the microinverter (Fig. 1).

There is a possibility that U_{max} and I_{max} data will be insufficient to identify potential faults and causes of reduced solar panel output. If U_{max} and I_{max} parameters are insufficient to determine potential faults, it is recommended to measure the solar panel's VAC. Using the measured and theoretical I-VAC, it is possible to identify other potential faults and causes of reduced electrical energy generation. Based on the curve's appearance or the difference in the numerical values between the measured VAC and the reference VAC, it is possible to identify potential faults or other causes of reduced solar panel electrical energy generation efficiency (Figure 1*b*, curves 2-4). In Figure 1*b*, the curves show the main (black dots) and additional (gray dots) points of maximum power.

If the observed effects are not included in the list of those entered into the database, a message may be sent to the operator regarding an unspecified error type.

The block diagram of the prototype and device under development is shown in Figure 2. This module contains a microcontroller device, a voltage and current measuring device, and temperature and illuminance meters.

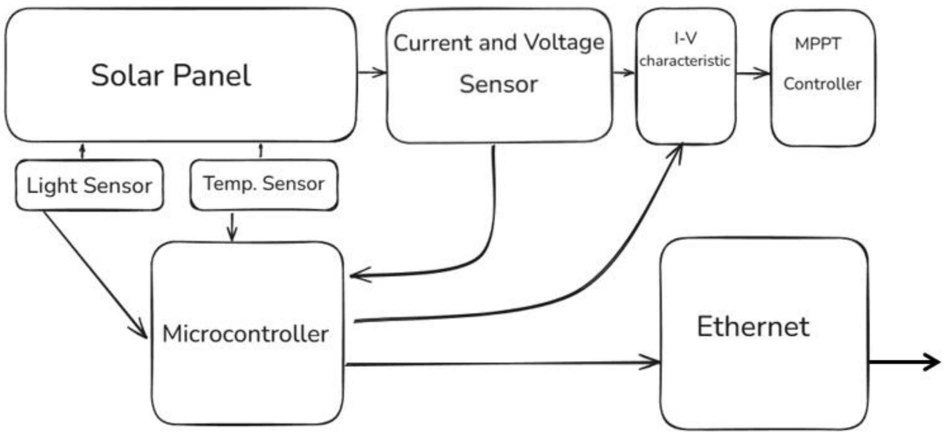

Figure 2. Functional diagram of the electrical device for measuring voltage and current at the maximum power point (U_{max}, I_{max}) and the I–V curve of the solar panel

LTSpice software was used to verify the functionality of the accepted circuit solutions. The printed circuit board was designed on the ECAD platform.

Functional requirements for the device — measurement of voltage, current, temperature and I–V curve of the solar panel.

Power supply — the device must operate independently of power control systems and be charged by a solar panel or wind turbine.

Technical requirements for the measuring device:

Measurable value ranges — voltage measurement range from 0 to 38 volts, current range from 0 to 10 amps, temperature range from –40 to +55 °C, illuminance range from 0 to 130,000 lux. The device must measure the I–V curve of a solar panel with a capacity of up to 240 watts.

Supported battery type (Li_2TiO_3) for independent power supply. Battery voltage not less than 5 volts.

Operating conditions: operating temperature from –40 to +60 °C. Dust and moisture protection class IP 65, complete protection against dust and jets from all sides under low pressure. No protection against overvoltage and overheating.

Supported communication interfaces: I2C, SPI, UART, OneWire, LoRawan 868 Mhz (license-free frequency permitted in Kazakhstan). Device control via LoRawan communication protocol. There are no buttons or screens.

Software and hardware requirements: STM32 platform microcontroller, support for firmware updates via UART and SWD interfaces. All collected data is transmitted to cloud storage via the LoRa wireless communication protocol, first to the gateway and then to the cloud.

Results and discussion

A prototype of a solar panel performance meter was assembled based on Arduino Mega 2560 R3 (Fig. 3, *a*). A Wiznet W5100 Ethernet module supporting TCP/UDP protocols was used to connect the Arduino Mega board to a local network or the Internet. The board is based on the W5100 chip and supports up to 4 connections at speeds of 10 and 100 Mbit/s. The board contains a micro-SD memory card slot. The data exchange protocol is SPI.

a) *b)*

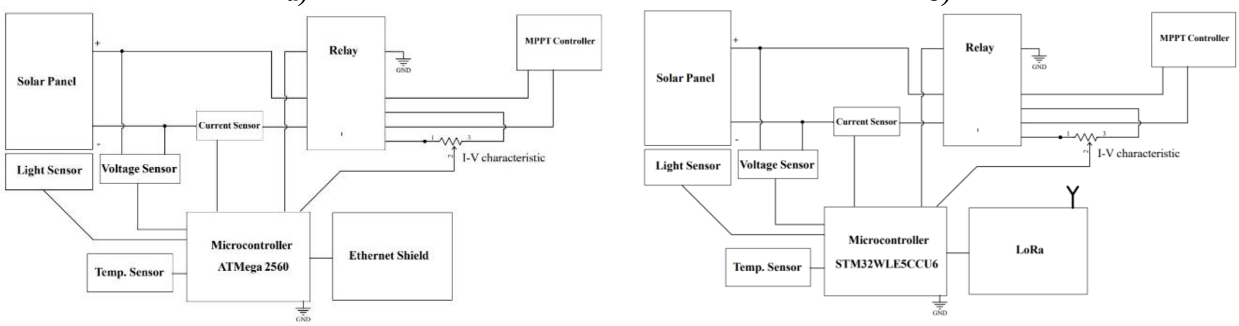

Figure 3. Block diagrams of the prototype (*a*) and measuring device (*b*)

The current is measured by an ACS712-20A Hall-effect sensor (maximum 20 A), and the panel voltage is measured via a divider connected to the microcontroller's ADC input. The Hall-effect sensor with a nominal sensitivity of 100 mV/A. The sensor output was digitized by a 16-bit ADS1115 ADC. The total current measurement uncertainty is dominated by the sensor sensitivity tolerance and offset voltage, resulting in an estimated accuracy of ±0.25 A (±2.5 % at 10 A).

The DC voltage was measured via a resistive divider (75 kΩ/10 kΩ, 2 % tolerance) followed by the same ADS1115 ADC. The resulting voltage measurement accuracy is approximately ±1.1 V, corresponding to ±2.8 % at 40 V. The ADC quantization error is negligible compared to the passive component tolerances.

A high-precision OPT4003-Q1 sensor is used to measure the illumination of the solar panel. It has high sensitivity and is designed for automotive use (class Q1), which guarantees its performance at low temperatures and under external influences. The device provides factory-calibrated illuminance data with a typical absolute accuracy of ±5 % and a maximum error of ±10 % over the specified operating conditions. Since the sensing element and ADC are integrated within the device, the quantization error is negligible compared to the sensor's specified accuracy.

DS18B20 digital temperature sensor was chosen as a reliable and widely used component with a digital interface, making it ideal for use in cold climates. The sensor provides factory-calibrated temperature readings with a guaranteed accuracy of ±0.5 °C in the –10 to +85 °C range and a resolution of 0.0625 °C. Since the sensing element and ADC are integrated within the device, the quantization error is negligible compared to the sensor's specified accuracy.

The Arduino board collects readings from all sensors and publishes them to the MQTT broker (Mosquitto). Telegraf subscribes to the relevant topics, receives the data and stores it in InfluxDB and PostgreSQL. Grafana connects to these databases and displays the data in the form of graphs and dashboards. More detailed information on the operation of the prototype and the experimental data obtained is given in [26].

The Arduino board control programme includes the following main modules:

1. Initialisation and interaction with sensors;
2. Collection, averaging, and storage of measurement data.
3. The programme measures the following physical quantities:

– panel electric current;
– panel electrical voltage;
– illuminance level;
– solar module surface temperature.

4. Data transmission via MQTT protocol;
5. Receiving control commands from the server;
6. In case of a request from the server, an algorithm for step-by-step change of electrical load is played to measure current and voltage from the solar panel in order to build the I–V curve of the solar panel.

One of the key functions of the device is the ability to automatically measure the I–V curve of the solar panel. Upon receiving a command from the server, the device performs the following sequence of actions:

– A relay is activated, which connects an electronic load to the panel;
– The load was adjusted step by step, which made it possible to obtain 50 discrete current values and 50 voltage values;
– The experimental points obtained form the panel's I–V curve;
– After the measurements are completed, all data is automatically sent to cloud storage via the MQTT protocol.

The software can be found at [27].

An example of measured I–V characteristics for the KZ PV 230 M60 solar panel is shown in Figure 4. The I–V curves of the cells are measured under current operating conditions, short-circuit conditions for 20–40 module cells, and open-circuit conditions for 20–40 module cells. The measurements showed results that correlated with model representations (Figure 1, *b*). However, analysis and comparison of theoretical and experimental data is not the primary goal of this work and will be conducted in future work.

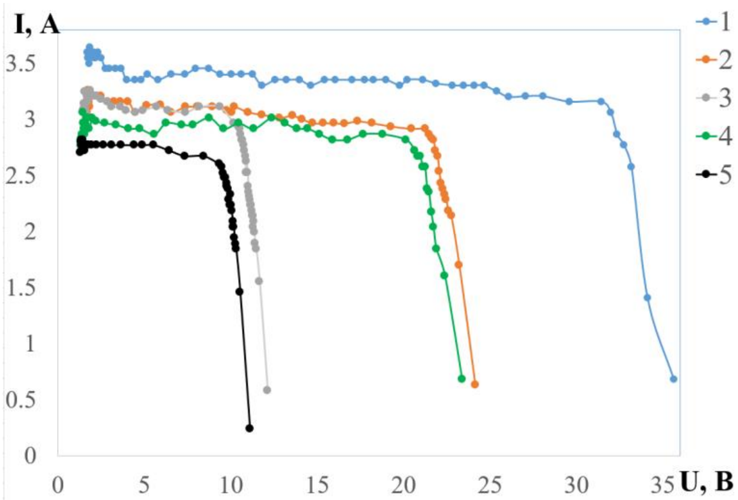

Figure 4. Measured I–V curves of the solar panel under different conditions:
1) I–V curve of the module at illumination level and temperature (Eυ = 430 W/m^2 and temperature T = 25 °C);
2) with a short circuit of 20 module cells (Eυ = 395 W/m², T = 25 °C);
3) with a short circuit of 40 module cells (Eυ = 395 W/m², T = 25 °C);
4) with a break in electrical connection with 20 module cells (Eυ = 370 W/m², T = 25 °C);
5) with a break in electrical connection with 40 module cells (Eυ = 370 W/m², T = 20 °C)

When designing an embedded IoT system for measuring the electrophysical parameters of a solar panel (Fig. 3, *b*), special attention was paid to the selection of components capable of functioning at low temperatures and ensuring stable operation of the device in field conditions. All electronic components used were selected taking into account climatic and operational requirements, as well as their functional compliance with the tasks solved within the system.

The RAK3172, an energy-efficient STM32-based module supporting the LoRaWAN protocol, was selected as the central control module. It provides reliable data transmission and has low power consumption, which is especially important for autonomous power plants. OPT4003 light sensors and DS18B20 temperature sensors are used. Current and voltage are measured using the INA228, a precision digital measurement amplifier capable of operating in an extended temperature range and providing high measurement accuracy. Electrical circuit diagrams are shown in the Figures S1–S4 in the Supplementary materials with a brief description of their functional purpose.

The device is powered by an LM2596T-5.0 DC-DC (Buck converter, step-down) stabilizer, which provides a stable output voltage of 5 V even when the input voltage fluctuates. ME6206A33PG linear stabilizer is used to power peripheral circuits, demonstrating high conversion efficiency and resistance to temperature fluctuations.

The design of the VAC removal unit is based on two powerful IRFP460 field-effect transistors, which made it possible to work with the required currents and voltages. To increase reliability and electrical safety, the system was designed with galvanic isolation from the microcontroller, which eliminated the impact of high currents on the control electronics. For analog control of the transistor gate voltage, an HA17358B operational amplifier is used, which is designed for precise regulation and is characterized by stable operation when the temperature changes.

The design uses X7R SMD capacitors, which are characterized by stable electrical parameters over a wide temperature range. This dielectric class ensures reliable operation of the devices in low temperatures typical for outdoor use. X7R capacitors maintain their capacitance with minimal deviations during temperature fluctuations, which is especially important for the operation of analog and power circuits.

The circuit also uses electrolytic capacitors specially selected for operation at sub-zero temperatures. Components with an extended temperature range are used, ensuring stable operation down to –40 °C and below, which prevents capacitance degradation and reduces the risk of failure during prolonged exposure to cold. This selection of passive components increases the reliability of the device and guarantees its resistance to external climatic influences.

A 3D view of the printed circuit board is shown in Figure 5.

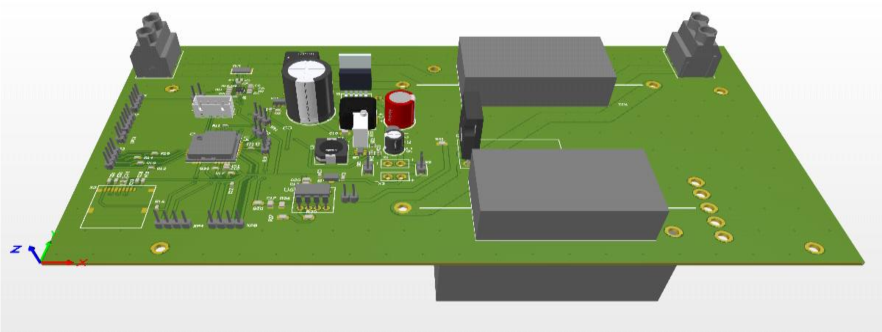

Figure 5. 3D view of the finished printed circuit board

The software for the device was developed in the Arduino IDE environment. This environment was chosen as the primary one for a number of practical reasons. First, it provides a convenient interface and access to a wide range of libraries, which simplifies interaction with microcontrollers. Secondly, and critically, the firmware pre-installed in the RAK3172 module is officially supported in Arduino IDE. The module is based on the STM32 architecture and works using the LoRaWAN protocol, so the choice of environment was actually predetermined [28].

The C language was chosen for writing the programme because it allows you to work effectively with systems where precise resource management is important. It provides direct access to hardware capabilities and is considered the primary language for working with microcontrollers.

The software structure of the device is based on a modular approach. Each block is responsible for a strictly defined function: interaction with peripheral devices, data collection and pre-processing, information transfer via the LoRaWAN network, working with an SD card, receiving commands from the server, etc. This solution simplifies scaling, maintenance, and future functionality expansion.

Initialisation begins with the configuration of all connected sensors. For example, current and voltage are measured using the INA228 microcircuit, which operates via the I²C interface. During initialisation, configuration parameters are written to its registers. The OPT4003-Q1 light sensor, which also uses the I²C interface, is configured using the same principle. The DS18B20 temperature sensor is connected via the OneWire bus using the DallasTemperature library.

After initialisation is complete, the system begins to periodically poll the sensors. The values obtained undergo primary processing: conversion to physical units, filtering, and checking of acceptable value limits. The data is then packaged into a formatted packet containing timestamps and parameters and transmitted via the RAK3172 module to the LoRaWAN network. The information is sent to the server via a gateway and then visualised or stored in a database.

A distinctive feature of the system is its support for feedback. The device not only transmits data, but can also receive commands from the server. This makes it possible, for example, to start the VAC measurement procedure for a solar panel when necessary. In VAC measurement mode, the device switches to a special mode: the output load is regulated by a PWM signal, which is converted into a linear voltage and fed to the gate of IRFP460 transistors, and the parameters—voltage and current—are measured dynamically. On the device itself, the VCC measurement command works as follows: the microcontroller switches the relay to the internal load from the transistors; the microcontroller outputs a PWM signal with a minimum duty cycle of 1 % from the required contact; the integrating chain receives it, and the output is a constant voltage with a minimum amplitude which is fed to the operational amplifier, and from there to the power transistor; it opens to the minimum value, loading the panel; the current and voltage are measured; the data is packaged and sent to the server via the gateway. The process of increasing the opening and recording continues until the PWM signal is completely filled, which means that we have opened the transistor completely and measured the VAC graph.

After each measurement, a packet is formed to be sent to the server and sent via LoRa to the gateway and then to the server.

In the event of a temporary loss of connection to the cloud system, the device switches to local storage mode. In this case, all data is recorded on a memory card, and as soon as the connection is restored, it is automatically transferred in sequence. This prevents information loss and maintains the integrity of the data set.

The program code is structured based on functions, macros, and user data types. Each logical block of the system is implemented separately, which improves readability and ease of maintenance. Working with sensors, LoRa connection logic, writing to an SD card, processing incoming commands — all of this is separated into separate sections of code, which makes it possible to develop the project without affecting its basic structure.

Thus, the software implemented as part of the work performs a full cycle — from collecting and analysing readings to transmitting them and responding to control signals. The architecture remains flexible, allowing the device to be adapted to new tasks, sensors to be added, and additional algorithms to be implemented in the future.

Conclusion

Thus, the proposed hardware and software solution provides comprehensive monitoring of key solar panel parameters — current, voltage, illuminance, and temperature — with data transmission over the network for further storage, processing, and visualisation.

To test the model, a system was assembled on an Arduino Mega 2560 R3 with an Ethernet Shield W5100, including ACS712 (20 A), a voltage divider, OPT4003 and DS18B20; VACs were measured using a controlled electronic load. The data was published in Mosquitto, aggregated by Telegraf, and stored in InfluxDB/PostgreSQL, followed by visualisation in Grafana. The sensors were calibrated against reference current and voltage sources.

An example of the I–V curves of the KZ PV 230 M60 solar panel is given in the text of the article.

During the course of the work, a full-fledged prototype of an embedded IoT system for monitoring solar panel parameters was developed, including both hardware and software components. Based on the prototype, a new device was created that meets all the functional and technical requirements.

During the development process:

– functional and technical requirements for the system were formed, operating conditions and supported interfaces were defined;

– a selection and justification of components capable of operating in a wide temperature range and ensuring high measurement accuracy was made;

– the schematic diagram and printed circuit board of the device were designed in the ECAD environment, component libraries and mounting locations were created in accordance with the technical documentation;

– individual circuit nodes were simulated in LTspice, which allowed the correctness of the selected circuit solutions to be confirmed prior to the hardware implementation stage;

– Software was developed in Arduino IDE using the **C** language, providing data collection from sensors, their pre-processing, transmission via the LoRaWAN protocol, as well as support for local storage of information and execution of control commands from the server.

– Algorithms were implemented to measure the volt-ampere characteristics of the solar panel with subsequent data transmission to the cloud.

– A functional block diagram has been created that reflects the operation of key system nodes.

Thus, the developed device meets the requirements: it operates autonomously from renewable energy sources, measures the necessary electrical and climatic parameters, is resistant to climatic conditions, and supports modern communication interfaces and the LoRaWAN protocol, which ensures integration into the IoT infrastructure.

The practical significance of the work lies in the creation of a universal platform for monitoring the condition of solar panels and wind turbines, which may be in demand in distributed energy systems, scientific research, and educational purposes. The result can be considered as a basis for further modernisation, adding new sensors and expanding the capabilities of the system depending on the specifics of operation.

Funding

This research is funded by the Science Committee of the Ministry of Science and Higher Education of the Republic of Kazakhstan (Grant No. AP22785282).

References

1 Štreimikienė, D., Lekavičius, V., Stankūnienė, G., & Pažėraitė, A. (2022). Renewable Energy Acceptance by Households: Evidence from Lithuania. *Sustainability*, *14*, 8370. DOI: https://doi.org/10.3390/su14148370

2 Rosak-Szyrocka, J., Allahham, A., Zywiolek, J., Turi, J., & Das, A. (2023). Expectations for Renewable Energy, and Its Impacts on Quality of Life in European Union Countries. *Management Systems in Production Engineering*, *31*(2), 128. DOI: 10.2478/mspe-2023-0015

3 Guta, D.D. (2020). Determinants of household use of energy-efficient and renewable energy technologies in rural Ethiopia. *Technology in Society*, *61*, 101249. Doi: https://doi.org/10.1016/j.techsoc.2020.101249

4 Vakacharla, V.R., Gnana, K., Xuewei, P., Narasimaharaju, B.L., Bhukya, M., Banerjee, A., Sharma, R., & Rathore, A.K. (2020). State-of-the-art power electronics systems for solar-to-grid integration. *Solar Energy*, *210*, 128. DOI: 10.1016/j.solener.2020.06.105

5 Moorthy, J.G., Moses, M.J., & Kalaiselvan, N. (2024). Active power regulation in low voltage grid-tied inverters for rooftop solar PV systems: Progress and future directions. *Energy Sources Part A — Recovery Utilization And Environmental Effects*, *46*(1), 81. DOI: 10.1080/15567036.2024.2392891

6 Vairavasundaram, I., Varadarajan, V., Pavankumar, P.J., Kanagavel, R.K., Ravi, L., & Vairavasundaram, S. (2021). A Review on Small Power Rating PV Inverter Topologies and Smart PV Inverters. *Electronics*, *10*(11), 1296. DOI: 10.3390/electronics10111296

7 Sarvi, M., & Azadian, A. (2022). A comprehensive review and classified comparison of MPPT algorithms in PV systems. *Energy Systems-Optimization Modeling Simulation and Economic Aspects*, *13*(2), 281. DOI: 10.1007/s12667-021-00427-x

8 Bhukya, L., Kedika, N.R., & Salkuti, S.R. (2022). Enhanced Maximum Power Point Techniques for Solar Photovoltaic System under Uniform Insolation and Partial Shading Conditions: A Review. *Algorithms*, *15*(10), 365. DOI: 10.3390/a15100365

9 Taghezouit, B., Harrou, F., Larbes, Ch., Sun, Y., Semaoui, S., Arab, A.H., & Bouchakour, S. (2022). Intelligent Monitoring of Photovoltaic Systems via Simplicial Empirical Models and Performance Loss Rate Evaluation under LabVIEW: A Case Study. *Energies*, *15*(21), 7955. DOI: 10.3390/en15217955

10 Madeti, S.R., & Singh, S.N. (2017). Online modular level fault detection algorithm for grid-tied and off-grid PV systems. *Solar energy*, *157*, 349. DOI: 10.1016/j.solener.2017.08.047

11 Chen, Z.C., Chen, Y.X., Wu, L., Cheng, S.Y., & Lin, P. (2019). Deep residual network based fault detection and diagnosis of photovoltaic arrays using current-voltage curves and ambient conditions. *Energy conversion and management*, *198*, 111793. DOI: 10.1016/j.enconman.2019.111793

12 Sharma, Ch., & Jain, A. (2014). Solar panel mathematical modeling using simulink. *Int. Journal of Engineering Research and Applications*, *4*(5), 67–72.

13 Kalliojarvi-Viljakainen, H., Lappalainen, K., & Valkealahti, S. (2022). A novel procedure for identifying the parameters of the single-diode model and the operating conditions of a photovoltaic module from measured current-voltage curves. *Energy Reports*, *8*, 4633. DOI: 10.1016/j.egyr.2022.03.141

14 Achouby, H.El., Zaimi, M., Ibral, A., & Assaid, E.M. (2018). New analytical approach for modelling effects of temperature and irradiance on physical parameters of photovoltaic solar module. *Energy Conversion and Management*, *177*, 258. DOI: https://doi.org/10.1016/j.enconman.2018.09.054

15 Das, S.K., Verma, D., Nema, S., & Nema, R.K. (2017). Shading mitigation techniques: State-of-the-art in photovoltaic applications. *Renewable & Sustainable Energy Reviews*, *78*, 369. DOI: 10.1016/j.rser.2017.04.093

16 Ali, M.H., Zakaria, M., & El-Tawab, S. (2025). A comprehensive study of recent maximum power point tracking techniques for photovoltaic systems. *Scientific Reports*, *15*(1), 14269. DOI: 10.1038/s41598-025-96247-5

17 Fkirin, M.A., Gowaly, Z.M., & Elsheikh, E.A. (2025). Dynamic Controller Design for Maximum Power Point Tracking Control for Solar Energy Systems. *Technologies*, *13*(2), 71. DOI: https://doi.org/10.3390/technologies13020071

18 Sarang, S.A., Raza, M.A., Panhwar, M., Khan, M., Abbas, G., Touti, E., Altamimi, A., & Wijaya, A.A. (2024). Maximizing solar power generation through conventional and digital MPPT techniques: a comparative analysis. *Scientific Reports*, *14*(1), 8944. DOI: 10.1038/s41598-024-59776-z

19 Huang, J.M., Wai, R.J., & Gao, W. (2019). Newly-Designed Fault Diagnostic Method for Solar Photovoltaic Generation System Based on IV-Curve Measurement. *IEEE Access*, *7*, 70919. DOI: 10.1109/ACCESS.2019.2919337

20 Li, B.J., Delpha, C., Migan-Dubois, A., & Diallo, D. (2021). Fault diagnosis of photovoltaic panels using full I-V characteristics and machine learning techniques. *Energy Conversion And Management*, *248*, 114785. DOI: 10.1016/j.enconman.2021.114785

21 Fadhel, S., Delpha, C., Diallo, D., Bahri, I., Migan, A., Trabelsi, M., & Mimouni, M.F. (2019). PV shading fault detection and classification based on I-V curve using principal component analysis: Application to isolated PV system. *Solar Energy*, *179*, 1. DOI: 10.1016/j.solener.2018.12.048

22 Cheddadi, Y., Cheddadi, H., Cheddadi, F., Errahimi, F., & Es-sbai, N. (2020). Design and implementation of an intelligent low-cost IoT solution for energy monitoring of photovoltaic stations. *SN Applied Sciences, 2*(7), 1165. DOI: 10.1007/s42452-020-2997-4

23 Madeti, S.R., & Singh, S.N. (2017). Online modular level fault detection algorithm for grid-tied and off-grid PV systems. *Solar Energy*, *157*, 349. DOI: 10.1016/j.solener.2017.08.047

24 Batzelis, E., & Papathanassiou, E. (2015). A method for the analytical extraction of the single-diode PV model parameters. *IEEE Transactions on Sustainable Energy*, *7*(2), 504. DOI: https://doi.org/10.1109/TSTE.2015.2503435

25 Tussupbekova A.K., Afanasyev D.A., Seldyugaev O.B., Karabassov V.A., Alpyssova G.K., Abikenov A.T., & Sheinmeier E.V. (2023). Development of a microcontroller device for reproducing audio information. *Eurasian Physical Technical Journal*, *20*(3), 70. DOI: 10.31489/2023No3/70-79

26 Tanasheva, N.K., Afanasyev, D.A., Ranova, G.A., Dyusembayeva, A.N., Sheinmaiyer, E., Rakhimgaliyev, T.A., & Bakhtybekova A.R. (2025). Thermophysical Aspects of Photovoltaic Module I–V Characteristics under Combined Environmental and Fault Conditions. *The European Physical Journal Plus.* (In press). https://github.com/mechanical-beaver/Solar-Panel-Sensor-Polling-System

27 Makhanov, K.M., Kurmanaliyev, N.B., Musepov, S.B., Naptalov, A.K., & Kenzhalieva, K.Z. (2022). Development of the wiring diagram of the device based on the LoRa module RAK3172. *Bulletin of the University of Karaganda-Physics, 108*(4), 48. DOI: 10.31489/2022PH4/48–55

Н.К. Танашева, Д.А. Афанасьев, Г.А. Ранова, Л.Л. Миньков,
А.Н. Дюсембаева, Е.В. Шейнмаиер, Т.А. Рахимгалиев, М.Қ. Қалиасқарова

Күн панельдерінің негізгі параметрлерін өлшеуге арналған микроконтроллер құрылғысын жобалау және прототиптеу

Мақалада күн панельдерінің (фототок және кернеу) және климаттық жағдайлардың (температура мен жарық) негізгі сипаттамаларын өлшеу құрылғысын прототиптеу және жобалау нәтижелері келтірілген. Бұл құрылғы күн панелі-микроинвертор жүйесіндегі мүмкін ақауларды, сондай-ақ жарық энергиясын электр энергиясына түрлендіру тиімділігінің төмендеуіне әкелетін себептерді анықтау мақсатында әзірленуде. Прототиптеу нәтижесінде W5100 Ethernet модулі бар Arduino Mega 2560 R3 негізіндегі өлшеу құрылғысының макеті жиналды. Ток ACS712 сенсорымен өлшенеді. Кернеу микроконтроллердің ADC кірісіне қосылған кернеу бөлгіш арқылы өлшенді. Opt4003 жарық және DS18B20 температура сенсорлары қолданылады. Интернет тарату құрылғысы INA228, OPT4003, DS18B20 сенсорлары мен чиптерінің rak3172 модулі негізінде құрастырылған. Күн панелінің Вольт-Ампер сипаттамаларын өлшеу үшін екі irfp460 өріс транзисторларына негізделген қуат модулі жасалды. Бағдарламалық жасақтама әзірленген прототип пен Интернет тарату құрылғысына жазылған.

Кілт сөздер: Интернет тарату құрылғысы, күн панелі, ақауларды анықтау, микроконтроллер, Вольт-Ампер сипаттамалары, жұмыс алгоритмі

Н.К. Танашева, Д.А. Афанасьев, Г.А. Ранова, Л.Л. Миньков,
А.Н. Дюсембаева, Е.В. Шейнмаиер, Т.А. Рахимгалиев, М.К. Калиаскарова

Проектирование и прототипирование микроконтроллерного устройства для измерения основных параметров солнечных панелей

В статье представлены результаты прототипирования и проектирования устройства измерения основных характеристик солнечных панелей (фототок и напряжение) и климатических условий (температура и освещенность). Данное устройство разрабатывается с целью определения возможных неисправностей в системе «солнечная панель — микроинвертор», а также причин, приводящих к снижению эффективности трансформации световой энергии в электрическую энергию. В результате прототипирования был собран макет измерительного устройства на базе Arduino Mega 2560 R3 с Ethernet-модулем W5100. Ток измеряется датчиком ACS712. Напряжение измерялось через делитель напряжения, подключённый к входу АЦП микроконтроллера. Использованы датчики освещенности OPT4003 и температуры DS18B20. IoT-устройство собрано на базе модуля RAK3172, датчиков и микросхем INA228, OPT4003, DS18B20. Для измерения вольт-амперных характеристик солнечной панели разработан силовой модуль на базе двух полевых транзисторов IRFP460. К разработанному прототипу и IoT-устройству написано программное обеспечение.

Ключевые слова: Устройство интернета вещей, солнечная панель, обнаружение неисправностей, микроконтроллер, вольт-амперные характеристики, алгоритм работы

Information about the authors

Tanasheva Nazgul — PhD, Professor, Department of Engineering Thermal Physics named after Professor Zh.S. Akylbaev, Buketov Karaganda National Research University, Karaganda, Kazakhstan; e-mail: nazgulya_tans@mail.ru; ORCID ID: https://orcid.org/0000-0002-6558-5383

Afanasyev Dmitry — PhD, Professor, Department of Radiophysics and Electronics, Buketov Karaganda National Research University, Karaganda, Kazakhstan; e-mail: a.d.afanasyev2@gmail.com; ORCID ID: https://orcid.org/0000-0002-0437-5315

Ranova Gulden — Doctoral student 2 years of study, Buketov Karaganda National Research University, Karaganda, Kazakhstan; e-mail: guldeshka2812@gmail.com; ORCID ID: https://orcid.org/0009-0006-9710-8406

Minkov Leonid — Doctor of Physical and Mathematical Sciences, Professor, Tomsk State University, Tomsk, Russia; e-mail: lminkov@ftf.tsu.ru ORCID ID: https://orcid.org/0000-0001-6776-6375

Dyusembayeva Ainura — PhD, Associate Professor, Department of Engineering Thermal Physics named after Professor Zh.S. Akylbaev, Buketov Karaganda National Research University, Karaganda, Kazakhstan; e-mail: aikabesoba88@mail.ru; ORCID ID: https://orcid.org/0000-0001-6627-7262

Sheinmaier Eduard — Laboratory Assistant, Center for Alternative Energy, Buketov Karaganda National Research University, Karaganda, Kazakhstan; e-mail: sheinmaier.edward.03@gmail.com; ORCID ID: https://orcid.org/0009-0007-2689-7943

Rakhimgaliev Temirbek — Laboratory Assistant, Center for Alternative Energy, Buketov Karaganda National Research University, Karaganda, Kazakhstan; e-mail: temirbek.18052003@gmail.com; ORCID ID: https://orcid.org/0009-0004-0909-2121

Kaliaskarova Madina — Engineer of the Department of Engineering Thermal Physics named after Professor Zh.S. Akylbaev; e-mail: kaliaskarovam@bk.ru

Article

UDC 621.3.01

https://doi.org/10.31489/2026PH1/59-68

Received: 30.10.2025
Accepted: 12.12.2025

S. Katsyv[1], V. Kukharchuk[1], V. Madyarov[1], V. Kucheruk[2]✉,
P. Kulakov[2], W. Mankovska[2], A.K. Khassenov[3], D.Zh. Karabekova[3]

[1]*Vinnytsia National Technical University, Vinnytsia, Ukraine;*
[2]*Uman National University, Uman, Ukraine;*
[3]*Buketov Karaganda National Research University, Karaganda, Kazakhstan*

Non-Standard Analysis in Electrical Engineering. Complex Circuits with Ideal Reactive Elements

The article presents the application of concepts and methods of non-standard analysis to problems of theoretical electrical engineering. It is substantiated that standard methods of electrical engineering are not effective enough, because they are excessively complex or even unsuitable for calculating DC electrical circuits containing ideal inductances and capacitances. This problem arises because for direct current (with zero frequency) the inductive resistance is zero, and the capacitive resistance goes to infinity. As a result, when using standard methods to calculate such electrical circuits, it is necessary to solve uncertainty expressions of the type $\frac{0}{0}$ or $\frac{\infty}{\infty}$, which creates difficulties within the framework of traditional mathematical analysis. Given the above difficulties, it is proposed to replace the classical mathematical analysis with a non-standard one. In this approach, the frequency of the direct current is considered not as zero, but as an infinitely small value α. This approach makes it possible to determine the reactance of inductive elements as αL and the reactance of capacitive elements as-$\frac{1}{\alpha C}$. This allows to successfully apply all standard methods of theoretical electrical engineering and avoid the need to work with indefinite expressions. The article provides specific examples of the analysis of complex direct current circuits with ideal inductances and capacitances.

Keywords: complex direct current circuits, non-standard analysis, electrical engineering, ideal reactive element

✉*Corresponding author*: Kucheruk, Vladimir, vladimir.kucheruk@gmail.com

Introduction

Non-standard analysis became widely used in the middle of the last century, which was made possible by the new axiomatics of mathematical analysis proposed at that time. Nowadays, non-standard analysis methods are quite often used in various fields of science and technology. When solving various technical and scientific problems, in some cases it is necessary to reveal uncertainties of the type $\frac{0}{0}$ or $\frac{\infty}{\infty}$, which is extremely difficult when using classical methods of analysis [1]. In such cases, it is advisable to use ideas and methods of non-standard analysis, which consist in the direct use of infinitely small and large numbers [2, 3]. In [4], the axiomatics of mathematical analysis are considered, which is based on the set of hyperreal numbers, which contains, in addition to standard numbers, also non-standard (infinitely small, infinitely large, their combinations with standard numbers) numbers. The use of non-standard analysis methods in identifying the internal parameters of electric motors, which in many cases cannot be implemented using traditional methods, is promising [5, 6]. Also, non-standard analysis methods can be used for mathematical modeling of electromechanical objects [7–9], mathematical modeling and calculation of measuring channels of electrical and non-electrical physical quantities [10–12], calculation of building structures [13, 14], analysis of biological [15], chemical [16] processes, as well as in medicine [17, 18]. The use of non-standard analysis in theoretical electrical engineering is especially important. Traditionally, calculation methods based on Ohm's and Kirchhoff's laws are used to analyze DC electrical circuits, but there are a number of tasks for which the use of these methods is practically impossible. Therefore, it is relevant to use the mathematical apparatus of non-standard analysis, which will allow using known unified methods for calculating such circuits. For example, this applies to the calculation of DC circuits with ideal reactive elements [19], as well as the analysis of transient processes in second-order electrical circuits with violation of switching laws [20]. This article discusses the use of non-standard analysis methods for complex circuits with ideal reactive elements.

Formulation of the problem

Calculation of DC circuits is usually carried out using traditional methods based on Ohm's and Kirchhoff's laws. However, such standard approaches are unsuitable for certain specific cases, in particular for complex electrical circuits containing ideal reactive elements. The complexity arises from the fact that at DC the resistance of an ideal inductance is zero, and the resistance of an ideal capacitance tends to infinity, which in this case makes it impossible to calculate complex circuits. In some cases, such problems can be solved by calculating using the energy characteristics of reactive elements, which significantly complicates the calculations, especially for complex circuits. In view of this, the application of the mathematical apparatus of non-standard analysis, which allows the use of unified methods for calculating such circuits, is relevant and promising. The paper considers non-standard analysis of complex DC circuits with ideal reactive elements. The aim of the article is to define a class of non-standard electrical engineering problems for the analysis of complex DC circuits with ideal inductances and capacitances, as well as to extend non-standard analysis methods to a wider class of problems involving the calculation of complex circuits with ideal inductances and capacitances.

Research results

Let R denote the ordered set of real numbers, and we will call the number α an infinitely small number if and only if

$$\forall r \in R(\alpha < r). \tag{1}$$

An infinitely large number will be called the number $\beta = \frac{1}{\alpha}$, for this case we can write

$$\forall r \in R(\beta > r). \tag{2}$$

Infinitesimal numbers of the first, second, third, and k-th order are defined, respectively, as $\alpha > \alpha^2 > \alpha^3 > \alpha^k$, and infinitely large numbers of the first, second, third, and k-th order are defined, respectively, as $\beta < \beta^2 < \beta^3 < \beta^k$.

All the rules of algebra apply to infinitely small and infinitely large numbers, namely addition, subtraction, multiplication, division, exponentiation, and theorems (commutativity, associativity, etc.). Infinitely small and infinitely large numbers, together with the real numbers $r \in R$, form an ordered set of hyperreal numbers $*R$, the real numbers $r \in R$ are called standard or Archimedean in contrast to the non-standard numbers $*r \in *R$. In the following, the notation $\approx$. ll mean the equivalence of two non-standard numbers.

For standard numbers m and n, the following relations are valid:

$$\frac{m\alpha}{n\alpha} = \frac{m}{n},\ \frac{m\alpha}{n} = \frac{m}{n}\alpha,\ m\alpha + n \approx n,\ m\alpha^k + n \approx n,\ \sin\alpha \approx \alpha,\ \cos\alpha \approx 1. \tag{3}$$

Not only the set of real numbers, but also the set of complex numbers has the same structure, based on this we can write:

$$m\alpha + jn \approx jn,\ m\beta + jn \approx m\beta,\ m + jn\alpha \approx m,\ m + jn\beta \approx jn\beta. \tag{4}$$

Since, in this case, the DC circuit is considered as a sinusoidal current circuit, the cyclic frequency of which is zero, the symbolic method can be used to solve such a problem, provided that $\omega = \alpha$. Assuming $\omega = \alpha$, for the complex resistance of the inductance we can write

$$\underline{Z}_L \approx j\alpha L, \tag{5}$$

and for the complex capacitance resistance

$$\underline{Z}_C \approx \frac{1}{j\alpha C}, \tag{6}$$

As a first example, consider the complex electrical circuit with three ideal inductances, two of which are magnetically coupled. First, consider the matched connection of ideal inductances, as shown in Fig. 1.

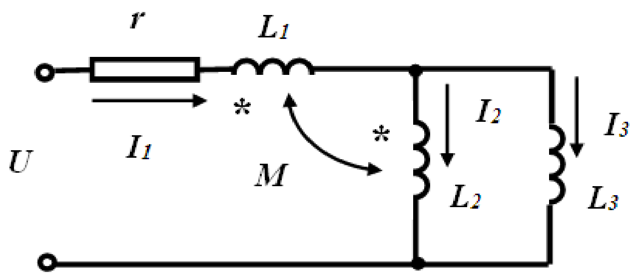

Figure 1. Electrical circuit with three ideal inductances and magnetic coupling between two of them (matched switching)

For the given circuit, the equations according to Kirchhoff's laws have the form:

$$\underline{I}_1 - \underline{I}_2 - \underline{I}_3 = 0, \tag{7}$$

$$\underline{I}_1 \left(r + j\alpha L_1 + j\alpha M \right) + \underline{I}_2 \left(j\alpha L_2 + j\alpha M \right) = U, \tag{8}$$

$$\underline{I}_3 j\alpha L_3 = \underline{I}_2 j\alpha L_2 + \underline{I}_1 j\alpha M. \tag{9}$$

Let perform equivalent transformations for equation (8).

$$\underline{I}_1 \left(r + j\alpha L_1 + j\alpha M \right) + \underline{I}_2 \left(j\alpha L_2 + j\alpha M \right) \approx I_1 r = U. \tag{10}$$

From expression (10) it follows:

$$\underline{I}_1 = \frac{U}{r}. \tag{11}$$

Thus, new equations were obtained in accordance with Kirchhoff's laws:

$$\frac{U}{r} - \underline{I}_2 - \underline{I}_3 = 0, \tag{12}$$

$$\underline{I}_3 j\alpha L_3 = \underline{I}_2 j\alpha L_2 + \frac{U}{r} j\alpha M. \tag{13}$$

Let's determine the current $\underline{I}_3$ from the equation (12) and substitute it into the second equation.

$$\underline{I}_3 = \frac{U}{r} - \underline{I}_2, \tag{14}$$

$$\left(\frac{U}{r} - \underline{I}_2 \right) j\alpha L_3 = \underline{I}_2 j\alpha L_2 + \frac{U}{r} j\alpha M. \tag{15}$$

From these equations it follows

$$\frac{U}{r} j\alpha L_3 - \underline{I}_2 j\alpha L_3 = \underline{I}_2 j\alpha L_2 + \frac{U}{r} j\alpha M, \tag{16}$$

$$\frac{U}{r} \left(j\alpha L_3 - j\alpha M \right) = \underline{I}_2 \left(j\alpha L_3 + j\alpha L_2 \right), \tag{17}$$

$$\underline{I}_2 = \frac{\frac{U}{r} \left(j\alpha L_3 - j\alpha M \right)}{\left(j\alpha L_3 + j\alpha L_2 \right)} = \frac{U \left(L_3 - M \right)}{r \left(L_3 + L_2 \right)}, \tag{18}$$

$$\underline{I}_3 = \frac{U}{r} - \underline{I}_2 = \frac{U}{r} - \frac{U \left(L_3 - M \right)}{r \left(L_3 + L_2 \right)} = \frac{U \left(L_2 + M \right)}{r \left(L_3 + L_2 \right)}. \tag{19}$$

As an example, let perform numerical calculations of the complex circuit shown in Figure 1 for three characteristic cases of the ratio between the inductances L_1, L_2, L_3 and the mutual inductance M, setting the following parameters: $U=30$ V, $r=10$ Ohm, $L_1=0.2$ H, $L_2=0.1$ H, $L_3=0.12$ H.

For the first characteristic case $M=0.05$ H, i.e. $M<L_2$. As a result of the calculation, we obtain $\underline{I}_2=0.955$ A, and $\underline{I}_3=2.045$ A.

For the second characteristic case $M=0.12$ H, i.e. $M=L_3$. In this case, all the current flows in the third coil ($\underline{I}_3=3$ A), and in the second coil it disappears ($\underline{I}_2=0$ A).

The most interesting is the third characteristic case, $M=0.14$ H, $L_3<M<\sqrt{L_1L_2}$. Here, the so-called "false capacitance effect" is observed, when the current in the third coil ($\underline{I}_3=3.273$ A) exceeds the input current, and in the second coil $\underline{I}_2=-0.273$ A the current changes its direction.

Let consider the case of counter-switching of inductors (Fig. 2).

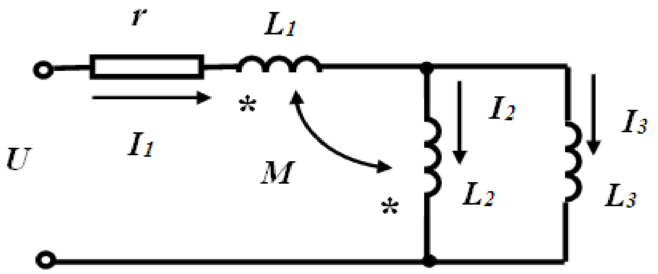

Figure 2. A circuit with three ideal inductances and magnetic coupling between two of them (counter-switching)

For the given circuit, the equations according to Kirchhoff's laws have the form:

$$\underline{I}_1-\underline{I}_2-\underline{I}_3=0, \tag{20}$$

$$\underline{I}_1\left(r+j\alpha L_1-j\alpha M\right)+\underline{I}_2\left(j\alpha L_2-j\alpha M\right)=U, \tag{21}$$

$$\underline{I}_3 j\alpha L_3=\underline{I}_2 j\alpha L_2-\underline{I}_1 j\alpha M. \tag{22}$$

Let perform equivalent transformations for equation (21).

$$\underline{I}_1\left(r+j\alpha L_1-j\alpha M\right)+\underline{I}_2\left(j\alpha L_2-j\alpha M\right)\approx \underline{I}_1 r=U. \tag{23}$$

From expression (23) it follows:

$$\underline{I}_1=\frac{U}{r}. \tag{24}$$

Thus, new equations were obtained in accordance with Kirchhoff's laws:

$$\frac{U}{r}-\underline{I}_2-\underline{I}_3=0, \tag{25}$$

$$\underline{I}_3 j\alpha L_3=\underline{I}_2 j\alpha L_2-\frac{U}{r}j\alpha M. \tag{26}$$

Let's determine the current $\underline{I}_3$ from the equation (25) and substitute it into the second equation.

$$\underline{I}_3=\frac{U}{r}-\underline{I}_2, \tag{27}$$

$$\left(\frac{U}{r}-\underline{I}_2\right)j\alpha L_3=\underline{I}_2 j\alpha L_2-\frac{U}{r}j\alpha M. \tag{28}$$

From these equations it follows

$$\frac{U}{r} j\alpha L_3 - \underline{I}_2 j\alpha L_3 = \underline{I}_2 j\alpha L_2 - \frac{U}{r} j\alpha M \,, \tag{29}$$

$$\frac{U}{r}\left(j\alpha L_3 + j\alpha M \right) = \underline{I}_2 \left(j\alpha L_3 + j\alpha L_2 \right), \tag{30}$$

$$\underline{I}_2 = \frac{\frac{U}{r}\left(j\alpha L_3 + j\alpha M \right)}{\left(j\alpha L_3 + j\alpha L_2 \right)} = \frac{U\left(L_3 + M\right)}{r\left(L_3 + L_2\right)}, \tag{31}$$

$$\underline{I}_3 = \frac{U}{r} - \underline{I}_2 = \frac{U}{r} - \frac{U\left(L_3 + M\right)}{r\left(L_3 + L_2\right)} = \frac{U\left(L_2 - M\right)}{r\left(L_3 + L_2\right)} \,. \tag{32}$$

As an example, let perform numerical calculations of the complex circuit shown in Figure 2 for three characteristic cases of the ratio between the inductances L_1, L_2, L_3 and the mutual inductance M, setting the following parameters: $U = 30$ V, $r = 10$ Ohm, $L_1 = 0.2$ H, $L_2 = 0.1$ H, $L_3 = 0.12$ H.

For the first characteristic case $M = 0.05$ H, i.e. $M < L_2$. As a result of the calculation, we obtain $\underline{I}_2 = 2.318$ A, and $\underline{I}_3 = 0.682$ A.

For the second characteristic case $M = 0.1$ H, i.e. $M = L_2$. In this case, all the current flows in the second coil ($\underline{I}_2 = 3$ A), and in the third coil it disappears ($\underline{I}_3 = 0$ A).

The most interesting is the third characteristic case, $M = 0.14$ H, $L_2 < M < \sqrt{L_1 L_2}$. Here, the so-called "false capacitance effect" is observed, when the current in the second coil ($\underline{I}_2 = 3.545$ A) exceeds the input current, and in the third coil $\underline{I}_3 = -0.545$ A the current changes its direction.

It should be noted that this task is very difficult to solve without the help of non-standard analysis methods, and for the next task it is practically impossible.

Let consider the second example, in which we determine the currents in all branches of a complex electrical circuit with ideal inductances and resistors, which is shown in Figure 3.

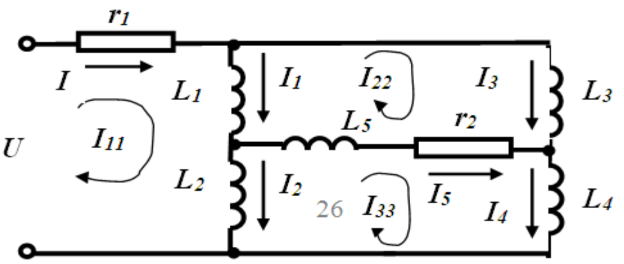

Figure 3. Complex electrical circuit with ideal inductances and resistors

Let the circuit shown in Figure 3 have the following parameters: $U = 100$ V, $r_1 = 10$ Ohm, $r_2 = 20$ Ohm, $L_1 = 0.2$ H, $L_2 = 0.15$ H, $L_3 = 0.1$ H, $L_4 = 0.05$ H, $L_5 = 0.025$ H. Let calculate this circuit using the loop current method. The equations for the loop current method have the form:

$$\underline{I}_{11}\underline{Z}_{11} + \underline{I}_{22}\underline{Z}_{12} + \underline{I}_{33}\underline{Z}_{13} = U \,, \tag{33}$$

$$\underline{I}_{11}\underline{Z}_{21} + \underline{I}_{22}\underline{Z}_{22} + \underline{I}_{33}\underline{Z}_{23} = 0 \,, \tag{34}$$

$$\underline{I}_{11}\underline{Z}_{31} + \underline{I}_{22}\underline{Z}_{32} + \underline{I}_{33}\underline{Z}_{33} = 0 \,. \tag{35}$$

Let find the self and common resistances of the contours:

$$\underline{Z}_{21} = -j\alpha L_1,\ \underline{Z}_{23} = -r_2 - j\alpha L_5,\ \underline{Z}_{31} = -j\alpha L_2, \tag{36}$$

$$\underline{Z}_{22} = j\alpha L_1 + j\alpha L_3 + j\alpha L_5 + r_2 \,, \tag{37}$$

$$\underline{I}_{33} = j\alpha L_2 + j\alpha L_4 + j\alpha L_5 + r_2 \,. \tag{38}$$

Let first consider equation (33), substituting into it expressions for the self and common resistances.

$$\underline{I}_{11}\left(r_1 + j\alpha L_1 + j\alpha L_2\right) + \underline{I}_{22}\left(-j\alpha L_1\right) + \underline{I}_{33}\left(-j\alpha L_2\right) = U \; . \tag{39}$$

Since only the coefficient at $\underline{I}_{11}$ is not infinitely small, we perform equivalent transformations:

$$\underline{I}_{11}\left(r_1 + j\alpha L_1 + j\alpha L_2\right) + \underline{I}_{22}\left(-j\alpha L_1\right) + \cdot_{33}\left(-j\alpha L_2\right) \approx \underline{I}_{11} r_1 = U \; . \tag{40}$$

From equation (40) it follows

$$\underline{I}_{11} = \underline{I} = \frac{U}{r_1} \, . \tag{41}$$

Similarly, we perform equivalent transformations for equation (34).

$$\frac{U}{r_1}\left(-j\alpha L_1\right) + \underline{I}_{22}\left(j\alpha L_1 + j\alpha L_3 + j\alpha L_5 + r_2\right) + \underline{I}_{33}\left(-r_2 - j\alpha L_5\right) \approx r_2 \underline{I}_{22} - r_2 \underline{I}_{33} = 0. \tag{42}$$

From equation (42) we obtain

$$\underline{I}_{22} = \underline{I}_{33} \, , \tag{43}$$

and

$$\underline{I}_5 = \underline{I}_{33} - \underline{I}_{22} = 0 \, . \tag{44}$$

Let perform equivalent transformations for equation (35).

$$\frac{U}{r_1}\left(-j\alpha L_2\right) + \underline{I}_{22}\left(-r_2 - j\alpha L_5\right) + \underline{I}_{33}\left(j\alpha L_2 + j\alpha L_4 + j\alpha L_5 + r_2\right) \approx -r_2 \frac{n!}{r!(n-r)!}_{22} + r_2 \underline{I}_{33} = 0. \tag{45}$$

It is obvious that

$$\underline{I}_{22} = \underline{I}_{33} \, . \tag{46}$$

Since there is no current in the inductance L_5, the task is significantly simplified, so we can write

$$\underline{I}_1 = \underline{I}_2 = \frac{U\left(L_3 + L_4\right)}{\left(L_1 + L_2 + L_3 + L_4\right) r_1} = 3\,\text{A}, \tag{47}$$

$$\underline{I}_3 = \underline{I}_4 = \frac{U\left(L_1 + L_2\right)}{\left(L_1 + L_2 + L_3 + L_4\right) r_1} = 7\ \text{A}. \tag{48}$$

Let's consider the third example, we will determine in a DC branched circuit with ideal capacitances (Fig. 4) the voltages on the capacitors C_1, C_2, C_3, the circuit parameters: $U = 100$ V, $C_1 = 200$ μF, $C_2 = 150$ μF, $C_3 = 100$ μF.

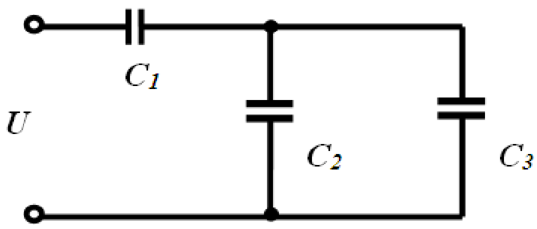

Figure 4. Branched circuit with ideal capacitances

Let find the total complex resistance of the circuit

$$\underline{Z}_{вх} \approx \frac{1}{j\alpha C_1} + \frac{\dfrac{1}{j\alpha C_2} \cdot \dfrac{1}{j\alpha C_3}}{\dfrac{1}{j\alpha C_2} + \dfrac{1}{j\alpha C_3}} = \frac{1}{j\alpha C_1} + \frac{\dfrac{1}{\left(j\alpha C_2\right)\left(j\alpha C_3\right)}}{\dfrac{j\alpha C_2 + j\alpha C_3}{\left(j\alpha C_2\right)\left(j\alpha C_3\right)}} =$$

$$=\frac{1}{j\alpha C_1}+\frac{1}{j\alpha C_2+j\alpha C_3}=\frac{j\alpha C_1+j\alpha C_2+j\alpha C_3}{j\alpha C_1\left(j\alpha C_2+j\alpha C_3\right)}=\frac{C_1+C_2+C_3}{j\alpha C_1\left(C_2+C_3\right)}, \tag{49}$$

then the current flowing through the capacitance C_1

$$\underline{I}_{C_1}=\frac{U}{\underline{Z}_{\text{вх}}}=\frac{Uj\alpha C_1\left(C_2+C_3\right)}{C_1+C_2+C_3}. \tag{50}$$

The currents flowing through the capacitors C_2, C_3 are found as

$$\underline{I}_{C_2}=\underline{I}_{C_1}\frac{\frac{1}{j\alpha C_3}}{\frac{1}{j\alpha C_2}+\frac{1}{j\alpha C_3}}=\frac{Uj\alpha C_1\left(C_2+C_3\right)}{C_1+C_2+C_3}\cdot\frac{\left(j\alpha C_2\right)}{j\alpha C_2+j\alpha C_3}=\frac{Uj\alpha C_1C_2}{C_1+C_2+C_3}, \tag{51}$$

$$\underline{I}_{C_3}=\underline{I}_{C_1}\frac{\frac{1}{j\alpha C_2}}{\frac{1}{j\alpha C_2}+\frac{1}{j\alpha C_3}}=\frac{Uj\alpha C_1\left(C_2+C_3\right)}{C_1+C_2+C_3}\cdot\frac{\left(j\alpha C_3\right)}{j\alpha C_2+j\alpha C_3}=\frac{Uj\alpha C_1C_3}{C_1+C_2+C_3}. \tag{52}$$

The voltages on the capacitors are determined by the following expressions:

$$U_{C_1}=\underline{I}_{C_1}\frac{1}{j\alpha C_1}=\frac{Uj\alpha C_1\left(C_2+C_3\right)}{C_1+C_2+C_3}\cdot\frac{1}{j\alpha C_1}=\frac{U\left(C_2+C_3\right)}{C_1+C_2+C_3}=42.857\text{ V}, \tag{53}$$

$$U_{C_2}=\underline{I}_{C_2}\frac{1}{j\alpha C_2}=\frac{Uj\alpha C_1C_2}{C_1+C_2+C_3}\cdot\frac{1}{j\alpha C_2}=\frac{UC_1}{C_1+C_2+C_3}=57.143\text{ V}, \tag{54}$$

$$U_{C_3}=\underline{I}_{C_3}\frac{1}{j\alpha C_3}=\frac{Uj\alpha C_1C_3}{C_1+C_2+C_3}\cdot\frac{1}{j\alpha C_3}=\frac{UC_1}{C_1+C_2+C_3}=57.143\text{ V}. \tag{55}$$

It is obvious that the voltages on the capacitors C_2, C_3 are the same.

Conclusion

1. The article systematizes a specific class of problems in theoretical electrical engineering. These problems concern the analysis of complex DC electrical circuits containing ideal capacitive and inductive elements. It is argued that traditional methods of analysis for this class of problems are extremely difficult or cannot be applied at all. This is due to the emergence of uncertainties caused by the limiting values of reactances at zero frequency (at DC).

2. To solve the above problems, it is proposed to apply a non-standard analysis, namely, to consider the frequency of the direct current not as zero, but as an infinitely small value. This approach transforms the original problem, making it suitable for solution using classical unified methods of theoretical electrical engineering.

3. The proposed approach, based on the use of non-standard analysis, has demonstrated high efficiency in solving electrical engineering problems on examples of analyzing complex electrical circuits with ideal reactive elements and contour parameters of various orders of infinitesimality.

4. It is advisable to direct further research to identify similar problems in other branches of science and technology, where the use of classical methods is limited due to the presence of boundary processes or uncertain analytical expressions. This will contribute to expanding the scope of application of non-standard analysis as an effective tool for mathematical modeling.

References

1 Benci, V., Cococcioni, M., & Fiaschi, L. (2022). Non-standard analysis revisited: An easy axiomatic presentation oriented towards numerical applications, *Int. J. Appl. Math. Comput. Sci.*, *32*(1), 65–80. https://doi.org/10.34768/amcs-2022-0006

2 Bell, J. (1998). *A Primer of Infinitesimal Analysis*. Cambridge University Press.

3 Lutz, R., & Goze, M. (1981). *Nonstandard Analysis: A Practical Guide with Applications*. Berlin: Springer-Verlag.

4 Robinson, A. (1996). *Non-Standard Analysis*. Princeton: Princeton University Press.

5 Aree, P. (2016). Analytical approach to determine speed-torque curve of induction motor from manufacturer data. *Procedia Computer Science, 86*, 293–296.

6 Kucheruk, V.Yu., Kurytnik, I.P., Oshanov, Ye.Z., Kulakov, P.I., Semenov, A.A., Karabekova, D.Zh., & Khassenov A.K. (2019). Computer-measuring system of the induction motor's dynamical torque-speed characteristics. *Bulletin of the University of Karaganda-Physics, 2*(94), 92–100.

7 Pfingsten, G., & Hameyer, K. (2017). Highly efficient approach to the simulation of variable-speed induction motor drives. *Science Measurement & Technology IET, 11*, 793–801.

8 Kojooyan-Jafari, H., Monjo, L., Córcoles, F., & Pedra, J. (2014). Parameter Estimation of Wound-Rotor Induction Motors From Transient Measurements, *IEEE Transactions on Energy Conversion*, *29*(2), 300–308. 10.1109/TEC.2014.2300236

9 Chirindo, M., Mushenya, J., Khan, M.A., & Barendse, P.S. (2023). Non-Intrusive Efficiency Estimation of Inverter-Fed Induction Motors. *IEEE Transactions on Energy Conversion, 38*(3), 1845–1854. DOI: 10.1109/TEC.2023.3242173

10 Podzharenko, V.A., & Kulakov, P.I. (2001). Photoelectric angle converter, Proc. SPIE 4425, Selected Papers from the International Conference on Optoelectronic Information Technologies (12 June). https://doi.org/10.1117/12.429768

11 Kassouf, N., Zappi, A., Monticelli, M., & Melucci, D. (2024). Analysis of Solid Formulates Using UV-Visible Diffused Reflectance Spectroscopy with Multivariate Data Processing Based on Net Analyte Signal and Standard Additions Method. *Chemosensors, 12*(11), 227. https://doi.org/10.3390/chemosensors12110227

12 Kucheruk, V., Kulakov, P., & Storozhuk, N. (2017). Measurement of the number servings of milk and control of water content in milk on stall milking machines. In: Szewczyk, R., Kaliczyńska, M. (Ed.) Recent Advances in Systems, Control and Information Technology. SCIT 2016. *Advances in Intelligent Systems and Computing,* 543. Springer, Cham. https://doi.org/10.1007/978-3-319-48923-0_46

13 Wang, C., Chang, L., & Chen, W. et al. (2025). Test and evaluation method of compressive strength of existing concrete structures, *Case Studies in Construction Materials, 23*, e05233. https://doi.org/10.1016/j.cscm.2025.e05233

14 Caicedo, D., Tomić, I., & Karimzadeh, S. et al. (2025). Code-based ground motion selection and scaling for seismic assessment: Application to two masonry building case studies. *Journal of Building Engineering, 111*, 113558. https://doi.org/10.1016/j.jobe.2025.113558

15 Ahmed, N., Yasin, M.W., & Iqbal, M.S., et al. (2025). Optimal and Computational Analysis Under the Noisy Environment in Biological Processes: The Stochastic Schnakenberg Model. *J Nonlinear Math Phys, 32*, 58. https://doi.org/10.1007/s44198-025-00311-7

16 Wacker, B. (2023). Framework for Solving Dynamics of Ca^{2+} Ion Concentrations in Liver Cells Numerically: Analysis of a Non-Negativity-Preserving Non-Standard Finite-Difference Method. *Mathematical Methods in the Applied Sciences, 46*(16), 16625–16643. https://doi.org/10.1002/mma.9464

17 Nogues I., Wen, J., & Zhao, Y., et al. (2024). Semi-supervised Double Deep Learning Temporal Risk Prediction (SeDDLeR) with Electronic Health Records. *Journal of Biomedical Informatics, 157*, 104685. https://doi.org/10.1016/j.jbi.2024.104685

18 Butt, A.I.K., Ahmad, W., & Rafiq, M., et al. (2023). Computationally efficient optimal control analysis for the mathematical model of Coronavirus pandemic. *Expert Systems with Applications, 234*, 121094. https://doi.org/10.1016/j.eswa.2023.121094

19 Katsyv, S., Kukharchuk, V., Kucheruk, V., Kulakov, P., & Gribov, M. (2023). Nonstandard analysis in electrical engineering. The analysis of the direct current circles with ideal reactive elements. *Bulletin of the University of Karaganda-Physics, 1*(109), 31–41. https://doi.org/10.31489/2023ph1/31-41

20 Katsyv, S., Kukharchuk, V., Madyarov, V., Holodiuk, V., Kucheruk, V., Kulakov, P., & Hribov, M. (2022). Non-standard analysis in electrical engineering. Transient analysis in second-order electrical circuits with violation of switching laws. *Bulletin of the University of Karaganda-Physics, 4,* 56–64. https://doi.org/10.31489/2022ph4/56-64

С. Кацыв, В. Кухарчук, В. Мадьяров, В. Кучерук,
П. Кулаков, В. Маньковская, А.К. Хасенов, Д.Ж. Карабекова

Электртехникадағы стандартты емес талдау. Идеал реактивті элементтері бар күрделі схемалар

Мақалада теориялық электртехника мәселелеріне стандартты емес талдаудың тұжырымдамалары мен әдістерін қолдану ұсынылған. Стандартты электртехника әдістері жеткілікті тиімді емес, өйткені олар өте күрделі немесе тіпті идеалды индуктивтілік пен сыйымдылықты қамтитын тұрақты ток тізбектерін есептеу үшін жарамсыз. Бұл мәселе тұрақты ток үшін (нөлдік жиілікте) индуктивті кедергі нөлге тең болғандықтан және сыйымдылық кедергісі шексіздікке кететіндіктен туындайды. Нәтижесінде, мұндай электр тізбектерін есептеудің стандартты әдістерін қолданған кезде, типтегі белгісіздік өрнектерін $\frac{0}{0}$ немесе $\frac{\infty}{\infty}$ дәстүрлі математикалық талдау шеңберінде қиындықтар туғызатын мәселелерді шешуге тура келеді. Осы қиындықтарды ескере отырып, классикалық математикалық анализді стандартты емес анализге ауыстыру ұсынылады. Бұл тәсілде тұрақты ток жиілігі нөлдік емес, α шексіз шамасы ретінде қарастырылады. Осы тәсіл индуктивті элементтердің реактивтілігін, сондай-ақ $\frac{1}{\alpha C}$ сыйымдылық элементтерінің реактивтілікті кедергісін анықтауға мүмкіндік береді. Бұл теориялық электртехниканың барлық стандартты әдістерін сәтті қолдануға және белгісіз өрнектермен жұмыс істеу қажеттілігін болдырмауға мүмкіндік береді. Мақалада идеалды индуктивтілігі мен сыйымдылығы бар күрделі тұрақты ток тізбектерін талдаудың нақты мысалдары келтірілген.

Кілт сөздер: тұрақты токтың күрделі тізбектері, стандартты емес талдау, электртехника, идеалды реактивті элемент

С.Ш. Кацыв, В.В. Кухарчук, В.Г. Мадьяров, В.Ю. Кучерук,
П.И. Кулаков, В.С. Маньковская, А.К. Хасенов, Д.Ж. Карабекова

Нестандартный анализ в электротехнике. Сложные схемы с идеальными реактивными элементами

В статье представлено применение концепций и методов нестандартного анализа к проблемам теоретической электротехники. Обосновано, что стандартные методы электротехники недостаточно эффективны, поскольку они чрезмерно сложны или даже непригодны для расчета электрических цепей постоянного тока, содержащих идеальные индуктивности и емкости. Эта проблема возникает из-за того, что для постоянного тока (с нулевой частотой) индуктивное сопротивление равно нулю, а емкостное сопротивление уходит в бесконечность. В результате при использовании стандартных методов расчета таких электрических цепей приходится решать выражения неопределенности типа $\frac{0}{0}$ или $\frac{\infty}{\infty}$, что создает трудности в рамках традиционного математического анализа. Учитывая указанные трудности, предлагается заменить классический математический анализ на нестандартный. При таком подходе частота постоянного тока рассматривается не как нулевая, а как бесконечно малая величина α. Такой подход позволяет определять реактивное сопротивление индуктивных элементов как и реактивное сопротивление емкостных элементов как — $\frac{1}{\alpha C}$. Это позволяет успешно применять все стандартные методы теоретической электротехники и избежать необходимости работы с неопределенными выражениями. В статье приведены конкретные примеры анализа сложных цепей постоянного тока с идеальными индуктивностями и емкостью.

Ключевые слова: сложные цепи постоянного тока, нестандартный анализ, электротехника, идеально-реактивный элемент

Information about the authors

Katsyv, Samoil — Candidate of Technical Sciences, Associate Professor, Department of Computerized Electromechanical Systems and Complexes, Vinnitsa National Technical University, Vinnytsia, Ukraine, e-mail: katsyvsam@ukr.net; ORCID ID: https://orcid.org/0000-0003-1375-5229

Kukharchuk, Vasily — Doctor of Technical Sciences, Professor, Department of Computerized Electromechanical Systems and Complexes, Vinnitsa National Technical University, Vinnytsia, Ukraine, e-mail: BKuch@ukr.net; ORCID ID: https://orcid.org/0000-0001-9920-2726

Madyarov, Vyacheslav — Candidate of Technical Sciences, Professor, Department of Computerized Electromechanical Systems and Complexes, Vinnitsa National Technical University, Vinnytsia, Ukraine, e-mail: madiarov@vntu.edu.ua; ORCID ID: https://orcid.org/0000-0002-6422-7779

Kucheruk, Vladimir (*corresponding author*) — Doctor of Technical Sciences, Professor, Department of Information Technologies of the Uman National University, Vinnytsia, Ukraine, e-mail: vladimir.kucheruk@gmail.com; ORCID ID: https://orcid.org/0000-0002-6422-7779

Kulakov, Pavel — Doctor of Technical Sciences, Professor, Department of Information Technologies of the Uman National University, Vinnytsia, Ukraine, e-mail: kulakovpi@gmail.com; ORCID ID: https://orcid.org/0000-0002-0167-2218

Mankovskaya, Victoria — Candidate of Technical Sciences, Associate Professor, Department of Information Technology, Uman National University, Vinnytsia, Ukraine, e-mail: viktoriyasergiivna@gmail.com; ORCID ID: https://orcid.org/0000-0003-0552-5482

Khassenov, Ayanbergen — PhD, Professor, Buketov Karaganda National Research University, Karaganda, Kazakhstan; e-mail; ayanbergen@mail.ru; ORCID ID: https://orcid.org/0000-0002-5220-9469

Karabekova, Dana — PhD, Professor, Buketov Karaganda National Research University, Karaganda, Kazakhstan; e-mail: karabekova71@mail.ru; ORCID ID: https://orcid.org/0000-0001-8776-4414

Article

UDC 548.73:539.23:621.3.049:620.9
https://doi.org/10.31489/2026PH1/69-80

Received: 23.10.2025
Accepted: 01.12.2025

Sh. Afroze[1, 2, 3], A.M. Kabyshev[1✉], A.A. Aimakhanova[1],
M.S. Reza[2], M.S. Islam[4], K.A. Kuterbekov[1], A.K. Azad[2]

[1]*Institute of Physical and Technical Sciences, L.N. Gumilyov Eurasian National University, Astana, Kazakhstan;*
[2]*University Brunei Darussalam, Bandar Seri Begawan, Brunei;*
[3]*Chalmers University of Technology, Gothenburg, Sweden;*
[4]*Bangladesh University of Engineering and Technology, Dhaka, Bangladesh*

A Study of Structural and Thermal Properties of a Novel Doped Perovskite-Type Oxide $SrFe_{0.6}Cu_{0.3}Mo_{0.1}O_{3-\delta}$

In this study, a novel perovskite-type oxide $SrFe_{0.6}Cu_{0.3}Mo_{0.1}O_{3-\delta}$ was synthesized via a conventional solid-state reaction route and comprehensively characterized using neutron powder diffraction (NPD), scanning electron microscopy (SEM), and thermal analysis. The application of NPD enabled precise determination of the atomic structure and differentiation between cations with similar atomic numbers. Rietveld refinement of the NPD data confirmed the formation of a single-phase cubic perovskite with the space group *Pm*-3*m* (no. 221) and a lattice parameter of $a = b = c = 3.8997(1)$ Å. SEM images revealed a highly porous, interconnected microstructure with uniform elemental distribution, while thermogravimetric analysis (TGA) demonstrated a two-step oxygen loss up to 1000 °C, confirming excellent thermal stability. The oxide exhibited a low thermal conductivity of 1.986 $W \cdot m^{-1} \cdot K^{-1}$ at 900 °C, attributed to enhanced phonon scattering induced by Cu and Mo co-doping and lattice disorder. These findings indicate that controlled B-site co-doping can effectively tailor defect chemistry and phonon transport, resulting in materials with reduced thermal conductivity and improved structural integrity. Therefore, $SrFe_{0.6}Cu_{0.3}Mo_{0.1}O_{3-\delta}$ shows great potential for high-temperature energy conversion applications, including thermoelectric devices and solid oxide fuel cells.

Keywords: perovskite oxide, neutron powder diffraction, Rietveld refinement, solid-state synthesis, scanning electron microscopy, thermogravimetric analysis, microstructure, oxygen non-stoichiometry, phonon scattering, thermal conductivity

✉*Corresponding author*: Kabyshev, Asset, kabyshev_am_1@enu.kz

Introduction

Perovskite-type oxides (ABX_3) were first identified in the mineral $CaTiO_3$, where A and B are cations and X is an anion. The perovskite lattice exhibits remarkable compositional flexibility, nearly all transition metals, lanthanides, and actinides can occupy the B-site, while larger alkali, alkaline-earth, or rare-earth ions occupy the A-site with twelve-fold oxygen coordination [1]. Doped perovskites with general formulas $A^{2+}B^{4+}O_3$, $A^{1+}B^{5+}O_3$, or $A^{3+}B^{3+}O_3$ have been widely studied because of their tunable physical and chemical properties [2]. Achieving single-phase perovskite oxides often requires high calcination temperatures and long sintering durations, especially when refractory metal oxides are incorporated [3–5]. Consequently, these materials have found broad applications in energy conversion and storage, superconductivity, ferroelectrics, piezoelectrics, and electrodes, owing to their excellent electrical, magnetic, and pyroelectric properties [6–18].

Neutron powder diffraction (NPD) provides a powerful tool for elucidating the atomic structures of such materials. Unlike X-ray diffraction, neutron scattering lengths are largely independent of atomic number, allowing accurate localization of light atoms (e.g., H, Li, O) and differentiation between neighboring elements or isotopes [19, 20]. As a result, NPD has become increasingly important for investigating advanced energy materials [21–23].

In thermoelectric and solid-oxide fuel cell (SOFC) applications, low thermal conductivity is desirable to minimize heat loss and enhance efficiency. While pristine $SrTiO_3$ exhibits relatively high thermal conductivity, targeted doping at the Sr- or Ti-site can effectively suppress phonon transport [24–29]. For example, La^{3+}, Sm^{3+}, and Y^{3+} substitutions at the Sr-site, or Nb-doping at the Ti-site, have yielded significant reductions in thermal conductivity.

Building upon this concept, we developed a co-doped perovskite $SrFe_{0.6}Cu_{0.3}Mo_{0.1}O_{3–\delta}$, introducing Cu and Mo at the B-site to tailor the crystal structure and defect chemistry. Using high-resolution time-of-flight neutron diffraction, we accurately determined the crystal symmetry and atomic arrangement, confirming a cubic perovskite phase with space group *Pm*-3*m*. Additionally, we investigated its microstructural morphology and thermal transport behavior to elucidate the structure–property relationship. The findings demonstrate that controlled B-site co-doping can effectively lower thermal conductivity without compromising structural stability, suggesting potential use in high-temperature electrochemical and thermoelectric systems [30].

Materials and methods

Grinding the powder particles mostly with mortar and pestle to homogenize the combination of reactants is referred to in solid-state synthesis [31–35]. Repeated grinding and firing of the compound until it achieves a single phase is used in this method. Polycrystalline sample of the $SrFe_{0.6}Cu_{0.3}Mo_{0.1}O_{3-\delta}$ was synthesized through a solid-state route by using $SrCO_3$ (≥99.90 %, Aldrich), Fe_2O_3 (≥99.998 %, Aldrich), CuO, and MoO_3 (≥99.50 %, Aldrich) ceramic powders with the inclusion of ethanol as a dispersing agent, the powders were manually ground in an agate mortar by a pestle. The hydraulic press was employed to pelletize the mixed powders, placed in α-Al_2O_3 crucibles, and annealed at elevated temperatures in a box furnace. The mixture of the powder samples was first annealed at 650 °C for 10 hours. After pelletizing, annealed at 900 °C for 12 hours, then sintered at 1100 °C for 12 hours, with intermediate grinding and pelletizing. The entire synthesis process was carried out in air.

Prior to neutron powder diffraction, XRD was used to determine the phase structure using a Bruker axs-D8 Advance diffractometer. At the ISIS Neutron & Muon Source in the UK, neutron powder diffraction data were acquired using the Polaris diffractometer (medium-resolution powder diffractometer at a high intensity) [36, 37]. Utilizing GSAS-II software [38], the time-of-flight (TOF) powder diffraction data were analyzed. Standard parameters were used in the Rietveld analysis to refine the results, including a shifted Chebyshev series as background that was initiated by the GSAS software, zero shift, scale factor, profile parameters (type 3 in GSAS), cell parameters, atomic coordinates, site-occupancy factor (SOF), and atomic displacement factors (ADP).

Scanning electron microscopy (SEM) was used to examine the morphological structure and to evaluate its porosity. Since the sample was extremely conductive, a coating of carbon was applied to prevent overcharging. The JSM-7610F (Japan Electron Optics Laboratory Co. Ltd., Japan) was used to capture the pictures of the surface of the pellet, and it gave an outstanding, high-contrast view of the pellet. Netzsch-Gerätebau GmbH-STA 409 PC Luxx Simultaneous Thermal Analyzer was employed to perform TGA in order to observe the weight change with rising temperature under flowing N_2. $SrFe_{0.6}Cu_{0.3}Mo_{0.1}O_{3-\delta}$ powder weighing 68.342 mg was put in an Al_2O_3 DSC/TG pan and heated at a rate of 5 °C/min while flowing N_2 at a rate of 20 ml/min. Before cooling, an hour of isothermal holding eliminated the absorbed species. To confirm that all pollutants had completely been desorbed, the procedure was then repeated. Once the desorption process was finished, N_2 flow was used in place of airflow, and the mass change was monitored until equilibrium was attained. A Netzsch-DSC 4044F1 was employed to perform differential scanning calorimetry in order to observe the heat flow with rising temperature under a flowing inert atmosphere (Ar). A Netzsch-LFA 467 HT/Hyper Flash was used to determine the thermal conductivity at a rate of 5 °C/min while flowing Ar at a rate of 20 ml/min.

Results and discussion

Crystal Structure Analysis

Perovskite oxides offer remarkable compositional flexibility due to the wide range of possible substitutions at both the A and B sites, enabling precise control over oxygen vacancy concentration, redox-active centers, and physicochemical properties [39, 40]. Fe-doped $SrTiO_3$ compositions such as $SrTi_{0.3}Fe_{0.7}O_{3-\delta}$ and $SrTi_{0.6}Fe_{0.4}O_{3-\delta}$ have demonstrated excellent anode performance for solid oxide fuel cells (SOFCs) when combined with $Ce_{0.9}Gd_{0.1}O_{2-\delta}$, as reported by Sungmee et al. [41].

In this study, the X-ray diffraction pattern of $SrFe_{0.6}Cu_{0.3}Mo_{0.1}O_{3-\delta}$ synthesized via the solid-state route revealed a single-phase cubic perovskite structure with space group *Pm*-3*m* (no. 221). To achieve a deeper understanding of its crystal structure, neutron powder diffraction (NPD) measurements were carried out at room temperature (Fig. 1). Rietveld refinement of the NPD data confirmed the single-phase cubic symmetry, with refined lattice parameters of $a = b = c = 3.8997(1)$ Å, consistent with the simple perovskite framework ($a_p \times a_p \times a_p$) where a_p is the primitive perovskite lattice parameter [42].

The diffraction data were refined using Bank 2 (up to 7 Å) of the POLARIS diffractometer. The refinement statistics and structural parameters are summarized in Table 1. The obtained low *R*-factors (R_p = 2.94 %, R_{wp} = 4.36 %, and R_f = 3.38 %) indicate excellent agreement between the observed and calculated profiles. The refined atomic positions, isotropic displacement parameters (U_{iso}), and Wyckoff sites confirm a well-ordered cubic structure without secondary phases or superstructure reflections associated with oxygen vacancy ordering.

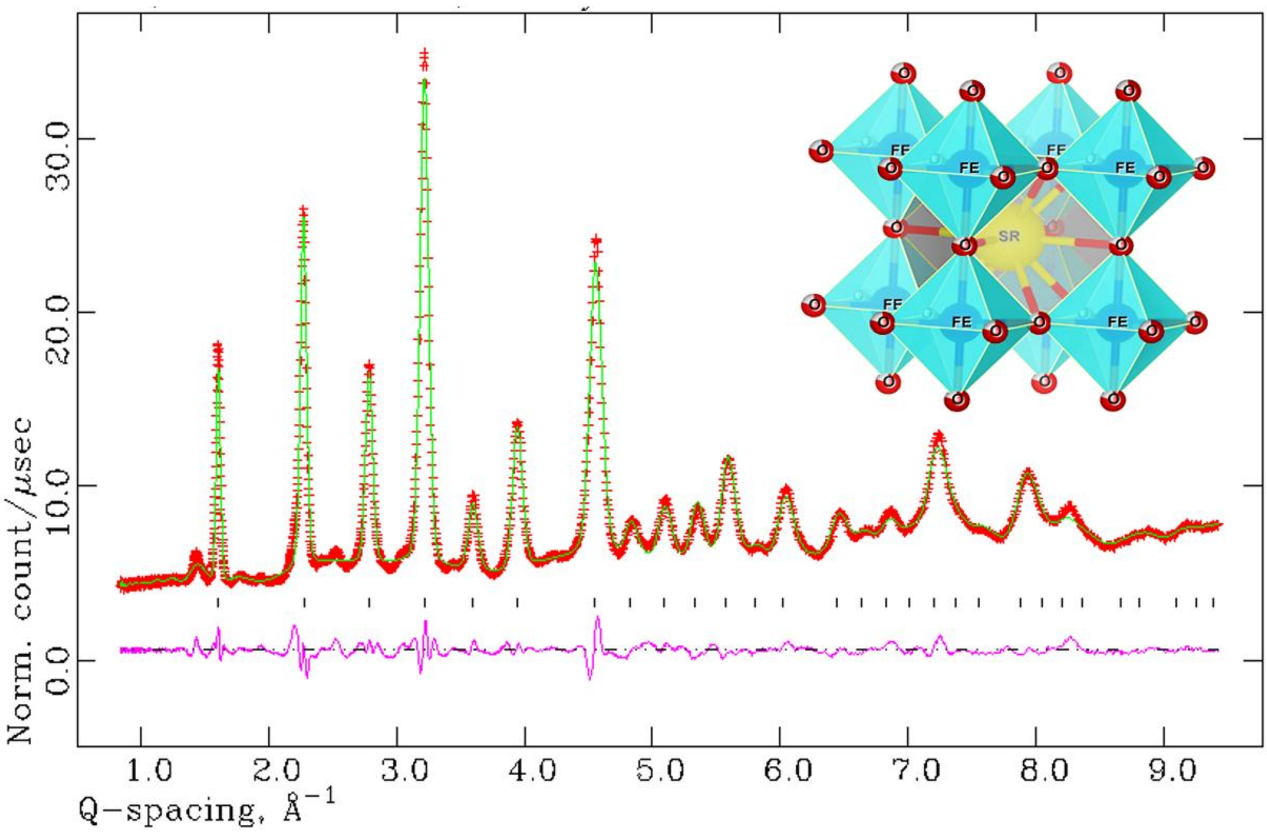

Figure 1. a) Rietveld refinement profile at room temperature for $SrFe_{0.6}Cu_{0.3}Mo_{0.1}O_{3-\delta}$.
The original data is represented by a crossline (red), the measured profile data is depicted by a continuous line (green), and the difference is shown by a bottom line (purple) with a 3D polyhedral representation of $SrFe_{0.6}Cu_{0.3}Mo_{0.1}O_{3-\delta}$ in it

Table 1

Rietveld refinement parameters for $SrFe_{0.6}Cu_{0.3}Mo_{0.1}O_{3-\delta}$ at room temperature (space group *Pm-3m*), atomic coordinates and isotropic temperature factors (U_{iso})

Parameters	$SrFe_{0.6}Cu_{0.3}Mo_{0.1}O_{3-\delta}$
Structure model	Cubic
Space group	*Pm-3m*
Volume (Å^3)	271.5090
R-factors	
R_f (%)	3.38
R_p (%)	2.94
R_{wp} (%)	4.36
Cell parameters	
a (Å)	3.8997 (1)
b (Å)	3.8997 (1)
c (Å)	3.8997 (1)
Atomic positions	*x*, *y*, *z*
Sr (1b)	0.5000, 0.5000, 0.0000
U_{iso} (Å^2)	0.0176 (1)
Fe (1a)	0.0000, 0.0000, 0.0000
U_{iso} (Å^2)	0.0045 (2)
Cu (1a)	0.0000, 0.0000, 0. 0.0000
U_{iso} (Å^2)	0.8000 (2)
Mo (1a)	0.0000, 0.0000, 0. 0.0000
U_{iso} (Å^2)	0.0183 (1)
O (3d)	0.5000, 0.0000, 0.0000
U_{iso} (Å^2)	0.0165 (1)

Bond Length Analysis

For an ideal cubic perovskite (ABO_3) structure, the bond lengths are given by d_a – O = $a/\sqrt{2}$ and d_b – O = a/2, where *a* is the lattice constant. The experimentally refined bond lengths for $SrFe_{0.6}Cu_{0.3}Mo_{0.1}O_{3-\delta}$ are listed in Table 2. The average B–O bond length was found to be 1.946 Å, in close agreement with the theoretical value calculated from the lattice constant and Shannon ionic radii [43].

Table 2

Bond distances for cubic $SrFe_{0.6}Cu_{0.3}Mo_{0.1}O_{3-\delta}$ in (Å) ($d \leq 6$ Å) extracted at room temperature (RT), based on NPD data

Bond	Multiplicity	Bond length (Å)
Sr–O_1	×12	2.75233 (3)
Fe–O_1	×6	1.94619 (3)
Cu–O_1	×6	1.94619 (3)
Mo–O_1	×6	1.94619 (3)

The absence of additional reflections in the NPD pattern suggests no symmetry reduction or long-range cation ordering, confirming that oxygen vacancies and cation substitutions do not induce structural distortion detectable within the resolution of the diffraction data.

The bond lengths obtained from the refinement were very close to the calculated bond lengths. The experimental bond length (B–O) for $SrFe_{0.6}Cu_{0.3}Mo_{0.1}O_{3-\delta}$ was obtained at 1.9462 Å (Table 2). The NPD layout measured at room temperature was appropriately refined in the space group *Pm*-3*m* and the polyhedral representation of the crystal structure as shown in Figure 1, displaying no extra peaks that ought to activist a superstructure bobbing up from oxygen vacancies or the long-range ordering of metals, or a reduction in symmetry.

Microstructural Characterization

The microstructure of the sample was examined using scanning electron microscopy (SEM) coupled with energy-dispersive X-ray spectroscopy (EDX). As shown in Figure 2, the SEM image reveals a porous and interconnected grain network, consistent with the open morphology typically observed in perovskite oxides synthesized via solid-state routes. The microstructure is composed of micrometer-sized agglomerates formed by the sintering of irregular nanocrystalline particles.

The presence of Cu^{2+} ions promotes enhanced grain growth and neck formation during sintering, leading to a partially fused morphology [44, 45]. The average grain size was approximately 1 µm, and EDX analysis confirmed a homogeneous elemental distribution of Sr, Fe, Cu, Mo, and O without detectable impurity phases. This uniformity further supports the single-phase nature of the compound as observed in the NPD and XRD analyses.

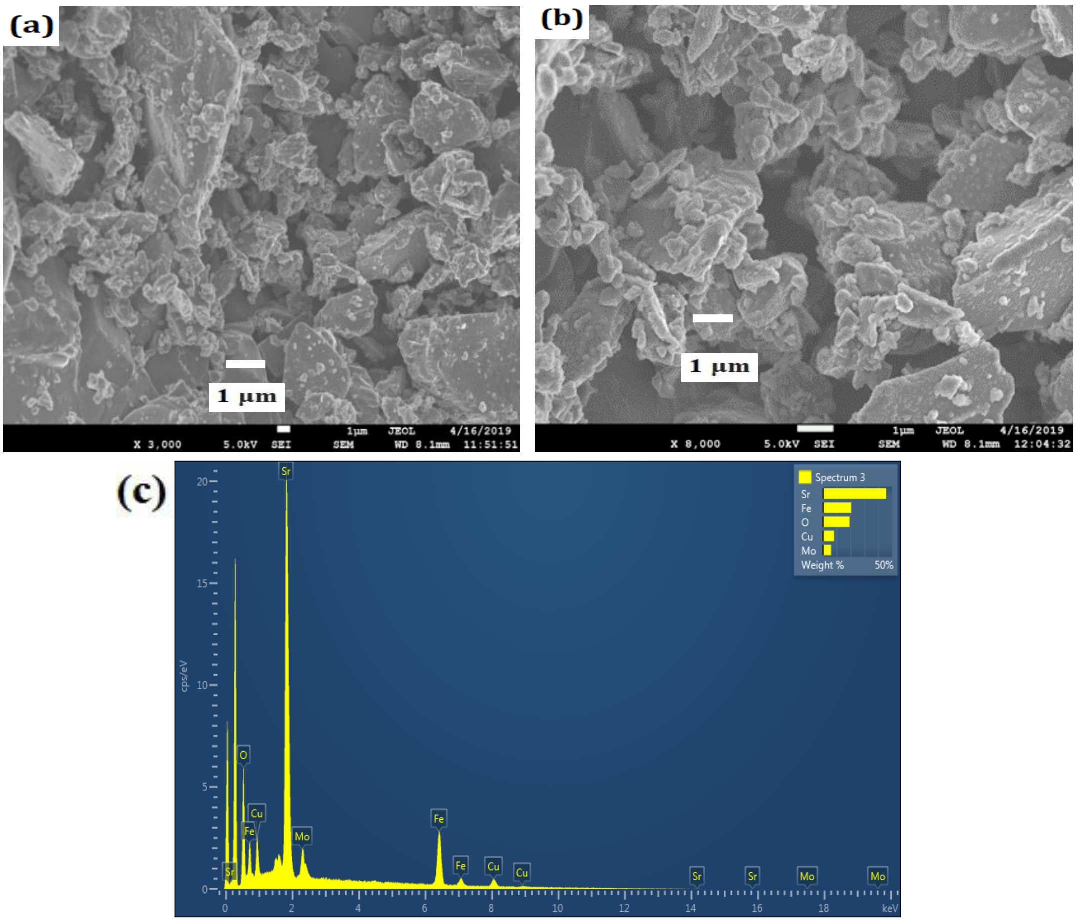

Figure 2. Scanning electron micrographs for $SrFe_{0.6}Cu_{0.3}Mo_{0.1}O_{3-\delta}$ pellet using a secondary electron image (SEI) detector with a low voltage (5.0 kV) with carbon-coated specimen and the associated EDS spectrum is shown in the inset

Thermal Analysis and Thermal Conductivity

Thermogravimetric analysis (TGA) of $SrFe_{0.6}Cu_{0.3}Mo_{0.1}O_{3-\delta}$ revealed a distinct two-stage weight loss pattern (Fig. 3). A sharp decrease in mass was observed up to 400 °C, similar to the thermal behavior reported by Rattiphorn et al. [44]. This initial weight loss is attributed to the release of physically adsorbed species and the partial oxidation of transition-metal cations. Between 400 °C and 650 °C, the weight loss proceeded gradually, corresponding to further oxidation reactions within the lattice and the formation of higher metal oxides. At elevated temperatures, CuO can partially decompose to Cu_2O, contributing to the observed mass change [45].

Copper-containing mixed oxides are widely recognized for their high oxygen exchange capacity and enhanced redox reactivity, which improve the performance of composite oxygen carriers and other functional materials [46–48]. To maintain an inert environment during the TGA experiment, the analysis was conducted under a nitrogen-rich atmosphere within a vacuum-sealed chamber. The onset of oxidation near 400 °C confirmed the sample's reactive oxygen mobility under thermal excitation.

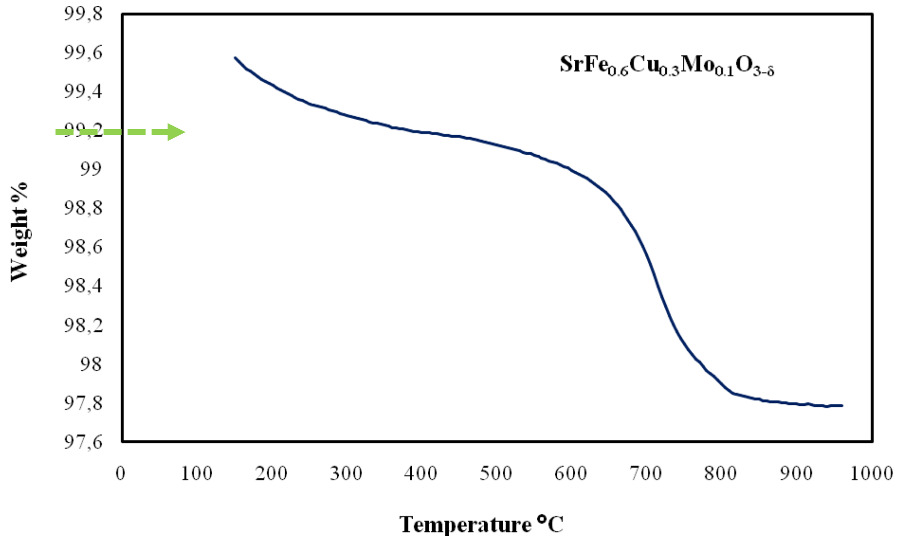

Figure 3. TGA diagram of $SrFe_{0.6}Cu_{0.3}Mo_{0.1}O_{3-\delta}$ on a scale of 20 °C to 950 °C

Differential scanning calorimetry (DSC) measurements (Fig. 4) further revealed a gradual increase in heat flow between room temperature and 110 °C, associated with the release of surface-bound volatiles. Two broad endothermic peaks appeared at 914 °C and 949 °C, followed by an endothermic transition near 104 °C, indicating structural rearrangements and oxygen loss at high temperature.

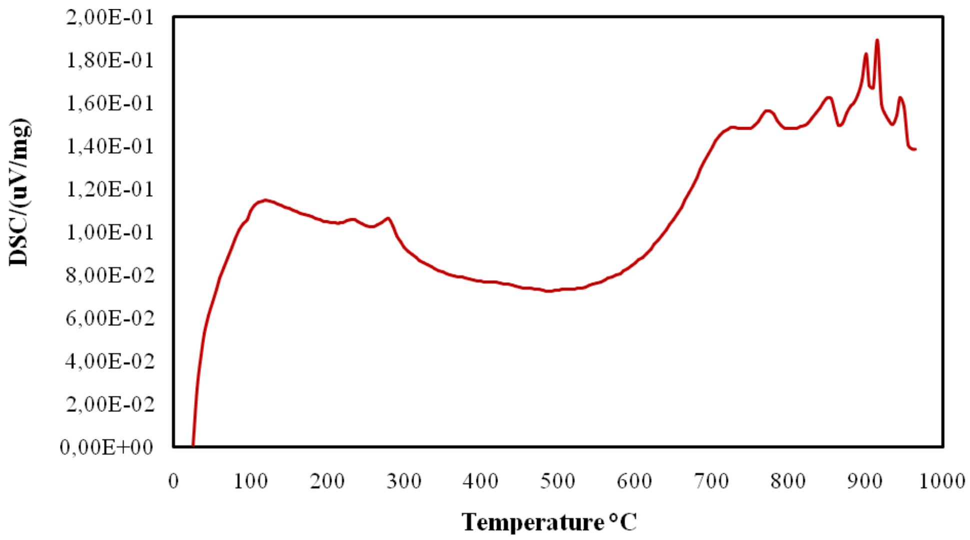

Figure 4. DSC diagram of $SrFe_{0.6}Cu_{0.3}Mo_{0.1}O_{3-\delta}$ on a scale of 25 °C to 950 °C

Thermal conduction in oxides primarily arises from phonon transport, governed by the mobility of lattice vibrations. Unlike metals, where free electrons dominate heat transfer, ceramic oxides exhibit inherently low thermal conductivity due to their predominantly ionic bonding and phonon scattering at grain boundaries. Additional microstructural factors such as porosity and grain interfaces further impede heat transport.

Perovskite-type oxides have, therefore, attracted considerable attention as low-thermal-conductivity materials with high structural stability at elevated temperatures [49, 50]. The measured thermal conductivity (κ) of $SrFe_{0.6}Cu_{0.3}Mo_{0.1}O_{3-\delta}$ from room temperature to 900 °C is presented in Figure 5. The oxide exhibited a value of 1.986 $Wm^{-1}K^{-1}$ at 900 °C, comparable to other complex perovskites such as $Sr_{0.9}La_{0.1}(Zr_{0.25}Sn_{0.25}Ti_{0.25}Hf_{0.25})O_3$ (1.89 $Wm^{-1}K^{-1}$ at 873 K) [51, 52] and significantly lower than undoped $SrTiO_3$ (10 W m^{-1} K^{-1} at 300 K) [53].

This reduction in κ can be attributed to enhanced phonon scattering caused by B-site cation disorder (Fe, Cu, Mo), oxygen vacancies, and the porous microstructure observed by SEM. These defects disrupt lattice periodicity and inhibit coherent phonon propagation. As summarized in Table 3, $SrFe_{0.6}Cu_{0.3}Mo_{0.1}O_{3-\delta}$ demonstrates one of the lowest thermal conductivities among single-phase cubic perovskites, confirming that Cu/Mo co-doping effectively tunes lattice dynamics without compromising phase stability.

Such a combination of structural stability, oxygen mobility, and low thermal conductivity suggests strong potential for this material in high-temperature thermoelectric and SOFC applications, where maintaining temperature gradients and minimizing heat loss are essential for improved performance and longevity.

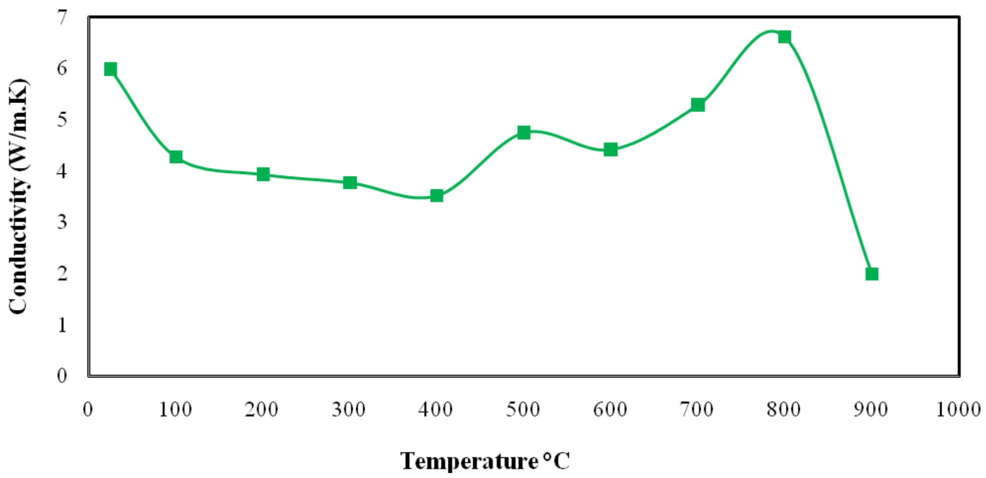

Figure 5. Thermal conductivity of $SrFe_{0.6}Cu_{0.3}Mo_{0.1}O_{3-\delta}$ on a scale of 25 °C to 900 °C

Table 3

Comparison of thermal conductivities for $SrFe_{0.6}Cu_{0.3}Mo_{0.1}O_{3-\delta}$ and other perovskite structures in the literature

Compositions	Temperature	Thermal conductivity ($Wm^{-1}K^{-1}$)	Ref.
$Sr_{0.9}La_{0.1}(Zr_{0.25}Sn_{0.25}Ti_{0.25}Hf_{0.25})O_3$	873 K	1.89	[52]
$(Ca_{0.25}Sr_{0.25}Ba_{0.25}La_{0.25})TiO_3$	1073 K	2.5	[54]
$SrZrO_3$	1273 K	2.1	[55]
$SrTiO_3$	300 K	10	[53]
$SrFe_{0.6}Cu_{0.3}Mo_{0.1}O_{3-\delta}$	1173 K	1.986	This work

Compared to other perovskites possessing single-phase cubic structures, $SrFe_{0.6}Cu_{0.3}Mo_{0.1}O_{3-\delta}$ exhibits a notably low thermal conductivity, as summarized in Table 3. The structural and thermal analyses indicate that the sample combines high porosity with good phase stability and a controlled degree of oxygen deficiency, which collectively contribute to its favorable thermal behavior. In this composition, the B-site cations (Fe, Cu, and Mo) occupy corner-shared octahedral sites within the cubic perovskite lattice, forming a well-defined and symmetrical framework.

The incorporation of Cu into the perovskite matrix not only promotes electronic conductivity but also modifies the lattice dynamics, enhancing phonon scattering and thereby reducing thermal transport. The resulting microstructure, characterized by a highly porous and interconnected network, facilitates effective charge mobility while impeding heat conduction. Thermogravimetric analysis revealed weight loss primarily between 200 °C and 950 °C, corresponding to oxygen release and the formation of thermally stable oxide phases.

Overall, the combination of single-phase cubic symmetry, controlled oxygen non-stoichiometry, and low thermal conductivity suggests that $SrFe_{0.6}Cu_{0.3}Mo_{0.1}O_{3-\delta}$ is a promising candidate for high-temperature thermoelectric and solid oxide fuel cell applications, where materials with low heat transport and stable structural integrity are essential.

Conclusion

A single-phase cubic perovskite oxide $SrFe_{0.6}Cu_{0.3}Mo_{0.1}O_{3-\delta}$ was successfully synthesized via the solid-state reaction method and characterized using neutron powder diffraction, scanning electron microscopy, and thermal analyses. Rietveld refinement of the neutron diffraction data confirmed that the material crystallizes in a simple cubic structure with space group *Pm*-3*m* and a lattice parameter of a = 3.8997(1) Å. The microstructural analysis revealed a homogeneous, porous morphology with interconnected grains, while TGA and DSC results demonstrated thermal stability up to 950 °C with oxygen release occurring in two main stages.

The measured thermal conductivity of 1.986 $Wm^{-1}K^{-1}$ at 900 °C indicates that Cu and Mo co-doping at the B-site effectively enhances phonon scattering and reduces heat transport without disrupting the structural integrity of the perovskite lattice. The combined characteristics of structural stability, controlled oxygen non-stoichiometry, and low thermal conductivity make $SrFe_{0.6}Cu_{0.3}Mo_{0.1}O_{3-\delta}$ a promising candidate for high-temperature energy applications such as solid oxide fuel cells and thermoelectric devices.

Future work will focus on correlating electrical conductivity and Seebeck coefficient data with the present thermal results to evaluate the overall thermoelectric performance and optimize the dopant concentration for enhanced functional efficiency.

Acknowledgment

This research was funded by the grant with reference number AP26103025, provided by the Ministry of Science and Higher Education of Kazakhstan. The authors are profoundly grateful to the L.N. Gumilyov Eurasian National University, Kazakhstan; Universiti Brunei Darussalam, Brunei; Chalmers University of Technology, Sweden for facilitating the work. The authors would also like to show gratitude to Professor Paul Henry and the ISIS Neutron and Muon facility in the UK for their scheduled beam-time.

References

1 Si, C., Zhang, W., Lu, Q., Guo, E., Yang, Z., Chen, J., He, X., & Luo, J. (2022). Recent advances in perovskite catalysts for efficient overall water splitting. *Catalysts, 12*(6), 601. https://doi.org/10.3390/catal12060601

2 Locock, A. J., & Mitchell, R.H. (2018). Perovskite classification: An Excel spreadsheet to determine and depict end-member proportions for the perovskite- and vapnikite-subgroups of the perovskite supergroup. *Computers & Geosciences, 113*, 106–114. https://doi.org/10.1016/j.cageo.2018.01.012

3 Jiang, W., Luo, W., Wang, J., Zhang, M., & Zhu, Y. (2016). Enhancement of catalytic activity and oxidative ability for graphitic carbon nitride. *Journal of Photochemistry and Photobiology C: Photochemistry Reviews, 28*, 87–115. https://doi.org/10.1016/j.jphotochemrev.2016.06.001

4 Mirzaei, M., Zarch, M.B., Darroudi, M., Sayyadi, K., Keshavarz, S.T., Sayyadi, J., Fallah, A., & Maleki, H. (2020). Silica mesoporous structures: Effective nanocarriers in drug delivery and nanocatalysts. *Applied Sciences, 10*(21), 7533. https://doi.org/10.3390/app10217533

5 Lu, Y., Zhang, Z., Wang, H., & Wang, Y. (2021). Toward efficient single-atom catalysts for renewable fuels and chemicals production from biomass and CO_2. *Applied Catalysis B: Environmental, 292*, 120–162. https://doi.org/10.1016/j.apcatb.2021.120162

6 Wang, R.T., Chang, H.Y., & Wang, J.C. (2021). An overview on the novel core–shell electrodes for solid oxide fuel cell (SOFC) using polymeric methodology. *Polymers, 13*(16), 2774. https://doi.org/10.3390/polym13162774

7 Madhavan, B., Suvitha, A., Steephen, A., & Pillai, M.B. (2022). Novel $La_{1-x}Ca_xTi_{1-y}Ta_yO_{3-\delta}$ perovskites with enhanced conductivity for solid oxide fuel cell electrodes. *Journal of Alloys and Compounds, 915*, 165370. https://doi.org/10.1016/j.jallcom.2022.165370

8 Cai, H., Xu, J., Wu, M., Long, W., Zhang, L., Song, Z., & Zhang, L. (2020). A novel cobalt-free $La_{0.5}Ba_{0.5}Fe_{0.95}Mo_{0.05}O_{3-\delta}$ electrode for symmetric solid oxide fuel cell. *Journal of the European Ceramic Society, 40*(12), 4361–4365. https://doi.org/10.1016/j.jeurceramsoc.2020.04.050

9 Song, J., Zhu, T., Chen, X., Ni, W., & Zhong, Q. (2020). Cobalt and titanium substituted $SrFeO_3$-based perovskite as efficient symmetrical electrode for solid oxide fuel cell. *Journal of Materials, 6*(2), 377–384. https://doi.org/10.1016/j.jmat.2020.02.009

10 Li, Q., Xia, T., Sun, L., Zhao, H., & Huo, L. (2014). Electrochemical performance of novel cobalt-free perovskite $SrFe_{0.7}Cu_{0.3}O_{3-\delta}$ cathode for intermediate temperature solid oxide fuel cells. *Electrochimica Acta, 150*, 151–156. https://doi.org/10.1016/j.electacta.2014.10.137

11 Ksepko, E. (2018). Perovskite $Sr(Fe_{1-x}Cu_x)O_{3-\delta}$ materials for chemical looping combustion applications. *International Journal of Hydrogen Energy, 43*(20), 9622–9634. https://doi.org/10.1016/j.ijhydene.2018.04.046

12 Omeiza, L.A., Kabyshev, A., Bekmyrza, K., Kubenova, M., Kuterbekov, K. A., Baratova, A., Adaikhan, S., Bakar, S.A., & Azad, A.K. (2024). Strontium-doped $BaZr_{0.8}Ni_{0.2}O_{3-\delta}$ cobalt-free cathode materials for solid oxide fuel cell. *International Journal of Precision Engineering and Manufacturing — Green Technology, 12*, 1295–1307. https://doi.org/10.1007/s40684-024-00667-z

13 Omeiza, L.A., Rahman, M.M., Kuterbekov, K.A., Kabyshev, A., Bekmyrza, K., Kubenova, M., Somalu, M.R., Bakar, S.A., & Azad, A.K. (2024). Novel Sr-doped $NdMn_{0.5}Cr_{0.5}O_{3-\delta}$ electrodes for symmetrical solid oxide fuel cell. *Electrochemistry Communications, 164*, 107730. https://doi.org/10.1016/j.elecom.2024.107730

14 Omeiza, L.A., Kuterbekov, K.A., Kabyshev, A., Bekmyrza, K., Kubenova, M., Afroze, S., Bakar, S.A., & Azad, A.K. (2024). Limitations and trends on cobalt-free cathode materials development for intermediate-temperature solid oxide fuel cell: An updated technical review. *Emergent Materials, 7*, 2189–2204. https://doi.org/10.1007/s42247-024-00737-7

15 Omeiza, L.A., Kabyshev, A., Bekmyrza, K., Kuterbekov, K.A., Kubenova, M., Zhumadilova, Z.A., Subramanian, Y., Ali, M., Aidarbekov, N., & Azad, A.K. (2025). Constraints in sustainable electrode materials development for solid oxide fuel cell: A brief review. *Materials Science for Energy Technologies, 8*, 32–43. https://doi.org/10.1016/j.mset.2024.07.001

16 Kuterbekov, K.A., Bekmyrza, K.Zh., Kabyshev, A.M., Kubenova, M.M., Aidarbekov, N.K., & Nurkenov, S.A. (2022). Investigation of the Characteristics of Materials with the Ruddlesden-Popper Structure for Solid Oxide Fuel Cells. *Bulletin of the University of Karaganda-Physics, 4*(108), 32–47. https://doi.org/10.31489/2022ph4/32-47

17 Adaikhan, S., Bekmyrza, K.Zh., Baratova, A.A., Kabyshev, A.M., Rajagopal, P., Aidarbekov, N.K., Kuterbekov, K.K., Kubenova, M.M., & Kuanysh, M.D. (2025). Development and characterization of nanostructured Ni–ScSZ composite anodes for solid oxide fuel cells. *Bulletin of the University of Karaganda-Physics*, *3*(119), 16–30. https://doi.org/10.31489/2025ph3/16-30

18 Bakalbayeva, G.A., Baratova, A.A., Aidarbekov, N.K., Kubenova, M.M., Amangozhayeva, A.N., & Bisseken, R.S. (2025). Investigation of the functional characteristics of $Pr_{1-x}Sr_xFe_{1-\gamma}Co_\gamma O_{3-\delta}$ perovskite cathodes for reversible solid oxide fuel cells. *Bulletin of the University of Karaganda-Physics*, *4*(120), 16–25. https://doi.org/10.31489/2025ph4/16-25

19 Tao, S., & Irvine, J.T.S. (2006). Phase transition in perovskite oxide $La_{0.75}Sr_{0.25}Cr_{0.5}Mn_{0.5}O_{3-\delta}$ observed by in situ high-temperature neutron powder diffraction. *Chemistry of Materials, 18*(23), 5453–5460. https://doi.org/10.1021/cm061413n

20 Afroze, S., Torino, N., Henry, P.F., Reza, M.S., Cheok, Q., & Azad, A.K. (2020). Insight of novel layered perovskite $PrSrMn_2O_{5+\delta}$: A neutron powder diffraction study. *Materials Letters, 261*, 127126. https://doi.org/10.1016/j.matlet.2019.127126

21 Hesse, F., Da Silva, I., & Bos, J.W.G. (2022). Insights into oxygen migration in $LaBaCo_2O_{6-\delta}$ perovskites from in situ neutron powder diffraction and bond valence site energy calculations. *Chemistry of Materials, 34*(3), 1191–1202. https://doi.org/10.1021/acs.chemmater.1c03726

22 Basbus, J.F., Arce, M.D., Napolitano, F.R., Troiani, H.E., Alonso, J.A., Saleta, M.E., González, M.A., Cuello, G.J., Fernández-Díaz, M.T., Sainz, M.P., Bonanos, N., Jimenez, C.E., Giebeler, L., Figueroa, S.J.A., Caneiro, A., Serquis, A.C., & Mogni, L.V. (2020). Revisiting the crystal structure of $BaCe_{0.4}Zr_{0.4}Y_{0.2}O_{3-\delta}$ proton conducting perovskite and its correlation with transport properties. *ACS Applied Energy Materials*, *3*(3), 2881–2892. https://doi.org/10.1021/acsaem.9b02498

23 Basbus, J.F., Arce, M.D., Alonso, J.A., González, M.A., Cuello, G.J., Fernández-Díaz, M.T., Sha, Z., Skinner, S.J., Mogni, L.V., & Serquis, A.C. (2022). In situ neutron diffraction study of $BaCe_{0.4}Zr_{0.4}Y_{0.2}O_{3-\delta}$ proton conducting perovskite: Insight into the phase transition and proton transport mechanism. *Journal of Materials Chemistry A, 10*(17), 9037–9047. https://doi.org/10.1039/d1ta10789e

24 Moos, R., Bischoff, T., Menesklou, W., & Härdtl, K.H. (1997). Solubility of lanthanum in strontium titanate in oxygen-rich atmospheres. *Journal of Materials Science*, *32*, 4247–4252. https://doi.org/10.1023/A:1018647117607

25 Lu, Z., Zhang, H., Lei, W., Sinclair, D.C., & Reaney, I.M. (2016). High-figure-of-merit thermoelectric La-doped A-site-deficient $SrTiO_3$ ceramics. *Chemistry of Materials, 28*(3), 925–935. https://doi.org/10.1021/acs.chemmater.5b04616

26 Han, J., Sun, Q., & Song, Y. (2017). Enhanced thermoelectric properties of La- and Dy-co-doped, Sr-deficient $SrTiO_3$ ceramics. *Journal of Alloys and Compounds, 705*, 22–27. https://doi.org/10.1016/j.jallcom.2017.02.146

27 Kovalevsky, A.V., Yaremchenko, A.A., Populoh, S., Thiel, P., Fagg, D.P., Weidenkaff, A., & Frade, J.R. (2014). Towards a high thermoelectric performance in rare-earth substituted $SrTiO_3$: Effects provided by strongly reducing sintering conditions. *Physical Chemistry Chemical Physics, 16*, 26946–26954. https://doi.org/10.1039/c4cp04127e

28 Gong, J., Yuan, Z., Xu, S., Li, Z., Xu, J., & Tang, G. (2017). Investigation of the thermoelectric properties of Nb- and oxygen-vacancy-co-doped $SrTiO_3$ ceramics. *Materials Research Express, 4*, 055504. https://doi.org/10.1088/2053-1591/aa6d04

29 Ohta, S., Ohta, H., & Koumoto, K. (2006). Grain size dependence of thermoelectric performance of Nb-doped $SrTiO_3$ polycrystals. *Journal of the Ceramic Society of Japan, 114*(1325), 102–105. https://doi.org/10.2109/jcersj.114.102

30 Leventouri, T., Bunaciu, C.E., & Perdikatsis, V. (2003). Neutron powder diffraction studies of silicon-substituted hydroxyapatite. *Biomaterials, 24*(23), 4205–4211. https://doi.org/10.1016/S0142-9612(03)00333-8

31 Jiang, S.P., Zhang, L., He, H.Q., Yap, R.K., & Xiang, Y. (2009). Synthesis and characterization of lanthanum silicate apatite by gel-casting route as electrolytes for solid oxide fuel cells. *Journal of Power Sources, 189*(2), 972–981. https://doi.org/10.1016/j.jpowsour.2008.12.064

32 Karim, A.H., Park, K.-Y., Lee, T.H., Ali, S.A.M., Hossain, S., Absah, H.Q.H.H., Park, J.-Y., & Azad, A.K. (2017). Synthesis, structure and electrochemical performance of double perovskite oxide $Sr_2Fe_{1-x}Ti_xNbO_{6-\delta}$ as SOFC electrode. *Journal of Alloys and Compounds, 724*, 666–673. https://doi.org/10.1016/j.jallcom.2017.07.059

33 Azad, A.K., Ivanov, S.A., Eriksson, S.-G., Eriksen, J., Rundlöf, H., Mathieu, R., & Svedlindh, P. (2001). Synthesis, crystal structure, and magnetic characterization of the double perovskite Ba_2MnWO_6. *Materials Research Bulletin, 36*(12), 2215–2228. https://doi.org/10.1016/S0025-5408(01)00707-3

34 Afroze, S., Torino, N., Henry, P.F., Reza, M.S., Cheok, Q., & Azad, A.K. (2020). Neutron and X-ray powder diffraction data to determine the structural properties of novel layered perovskite $PrSrMn_2O_{5+\delta}$. *Data in Brief, 29*, 105173. https://doi.org/10.1016/j.dib.2020.105173

35 Rahman, S.M.H., Norberg, S.T., Knee, C.S., Biendicho, J.J., Hull, S., & Eriksson, S.G. (2014). Proton conductivity of hexagonal and cubic $BaTi_{1-x}Sc_xO_{3-\Delta}$ ($0.1 \le x \le 0.8$). *Dalton Transactions, 43*, 15055–15064. https://doi.org/10.1039/c4dt01280a

36 Smith, R.I., Hull, S., Tucker, M.G., Playford, H.Y., McPhail, D.J., Waller, S.P., & Norberg, S.T. (2019). The upgraded Polaris powder diffractometer at the ISIS neutron source. *Review of Scientific Instruments, 90*, 115101–115113. https://doi.org/10.1063/1.5099568

37 Hull, S., Smith, R.I., David, W.I.F., Hannon, A.C., Mayers, J., & Cywinski, R. (1992). The Polaris powder diffractometer at ISIS. *Physica B: Condensed Matter, 180-181*, 1000–1002. https://doi.org/10.1016/0921-4526(92)90533-X

38 Toby, B.H., & Von Dreele, R.B. (2013). GSAS-II: The genesis of a modern open-source all-purpose crystallography software package. *Journal of Applied Crystallography, 46*, 544–549. https://doi.org/10.1107/S0021889813003531

39 Cowin, P.I., Lan, R., Petit, C.T.G., Du, D., Xie, K., Wang, H., & Tao, S. (2017). Conductivity and redox stability of new perovskite oxides $SrFe_{0.7}TM_{0.2}Ti_{0.1}O_{3-\delta}$ (TM = Mn, Fe, Co, Ni, Cu). *Solid State Ionics, 301*, 99–105. https://doi.org/10.1016/j.ssi.2017.01.017

40 Cowin, P.I., Lan, R., Petit, C.T.G., & Tao, S. (2015). Conductivity and redox stability of perovskite oxide $SrFe_{1-x}Ti_xO_{3-\delta}$ ($x \leq 0.3$). *Solid State Sciences, 46*, 62–70. https://doi.org/10.1016/j.solidstatesciences.2015.05.004

41 Cho, S., Fowler, D.E., Miller, E.C., Cronin, J.S., Poeppelmeier, K.R., & Barnett, S.A. (2013). Fe-substituted $SrTiO_{3-\delta}Ce_{0.9}Gd_{0.1}O_2$ composite anodes for solid oxide fuel cells. *Energy & Environmental Science, 6*, 1850–1857. https://doi.org/10.1039/c3ee23791e

42 Lan, R., Cowin, P.I., Sengodan, S., & Tao, S. (2016). A perovskite oxide with high conductivities in both air and reducing atmosphere for use as electrode for solid oxide fuel cells. *Scientific Reports, 6*, 31839. https://doi.org/10.1038/srep31839

43 Shannon, R.D. (1976). Revised effective ionic radii and systematic studies of interatomic distances in halides and chalcogenides. *Acta Crystallographica Section A, 32*, 751–767. https://doi.org/10.1107/S0567739476001551

44 Sumang, R., & Bongkarn, T. (2011). The influences of firing temperatures and excess PbO on the crystal structure and microstructure of $(Pb_{0.25}Sr_{0.75})TiO_3$ ceramics. *Journal of Materials Science, 46*, 6823–6829. https://doi.org/10.1007/s10853-011-5641-2

45 Barbooti, M.M. (1984). Thermal behaviour of copper oxides and copper sulphate in the presence of carbon. *Solar Energy Materials, 10*(1), 35–40. https://doi.org/10.1016/0165-1633(84)90005-4

46 Yang, W., Zhao, H., Wang, K., & Zheng, C. (2015). Synergistic effects of mixtures of iron ores and copper ores as oxygen carriers in chemical-looping combustion. *Proceedings of the Combustion Institute, 35*(3), 2811–2818. https://doi.org/10.1016/j.proci.2014.07.010

47 Siriwardane, R., Benincosa, W., Riley, J., Tian, H., & Richards, G. (2016). Investigation of reactions in a fluidized bed reactor during chemical looping combustion of coal/steam with copper oxide–iron oxide–alumina oxygen carrier. *Applied Energy, 183*, 1550–1564. https://doi.org/10.1016/j.apenergy.2016.09.045

48 Duan, L., Godino, D., Manovic, V., Montagnaro, F., & Anthony, E.J. (2016). Cyclic oxygen release characteristics of bifunctional copper oxide/calcium oxide composites. *Energy Technology, 4*(10), 1171–1178. https://doi.org/10.1002/ente.201600028

49 Liu, Y., Jia, D., Zhou, Y., Zhou, Y., Zhao, J., Nian, H., & Liu, B. (2020). $Zn_{0.1}Ca_{0.1}Sr_{0.4}Ba_{0.4}ZrO_3$: A non-equimolar multicomponent perovskite ceramic with low thermal conductivity. *Journal of the European Ceramic Society, 40*(15), 6272–6277. https://doi.org/10.1016/j.jeurceramsoc.2020.07.054

50 Zhao, Z., Xiang, H., Dai, F.Z., Peng, Z., & Zhou, Y. (2019). $(La_{0.2}Ce_{0.2}Nd_{0.2}Sm_{0.2}Eu_{0.2})_2Zr_2O_7$: A novel high-entropy ceramic with low thermal conductivity and sluggish grain growth rate. *Journal of Materials Science & Technology, 35*(11), 2647–2651. https://doi.org/10.1016/j.jmst.2019.05.054

51 Banerjee, R., Chatterjee, S., Ranjan, M., Bhattacharya, T., Mukherjee, S., Jana, S.S., Dwivedi, A., & Maiti, T. (2020). High-Entropy Perovskites: An Emergent Class of Oxide Thermoelectrics with Ultralow Thermal Conductivity. *ACS Sustainable Chemistry & Engineering, 8*(46), 17022–17032. https://doi.org/10.1021/acssuschemeng.0c03849

52 Lou, Z., Zhang, P., Zhu, J., Gong, L., Xu, J., Chen, Q., Reece, M.J., Yan, H., & Gao, F. (2022). A novel high-entropy perovskite ceramic $Sr_{0.9}La_{0.1}(Zr_{0.25}Sn_{0.25}Ti_{0.25}Hf_{0.25})O_3$ with low thermal conductivity and high Seebeck coefficient. *Journal of the European Ceramic Society, 42*(8), 3480–3488. https://doi.org/10.1016/j.jeurceramsoc.2022.02.053

53 Ekren, D., Azough, F., & Freer, R. (2019). Enhancing the thermoelectric properties of $Sr_{1-x}Pr_{2x/3\pm x/3}TiO_{3\pm\delta}$ through control of crystal structure and microstructure. *Philosophical Transactions of the Royal Society A: Mathematical, Physical and Engineering Sciences, 377*, 20190037. https://doi.org/10.1098/rsta.2019.0037

54 Zhang, P., Gong, L., Lou, Z., Xu, J., Cao, S., Zhu, J., Yan, H., & Gao, F. (2022). Reduced lattice thermal conductivity of perovskite-type high-entropy $(Ca_{0.25}Sr_{0.25}Ba_{0.25}Re_{0.25})TiO_3$ ceramics by phonon engineering for thermoelectric applications. *Journal of Alloys and Compounds, 898*, 162858. https://doi.org/10.1016/j.jallcom.2021.162858

55 Ma, W., Jarligo, M.O., Mack, D.E., Pitzer, D., Malzbender, J., Va'en, R., & Stöver, D. (2008). New generation perovskite thermal barrier coating materials. *Journal of Thermal Spray Technology, 17*, 831–837. https://doi.org/10.1007/s11666-008-9239-4

Ш. Афрозе, А.М. Кабышев, А.А. Аймаханова,
М.С. Реза, М.С. Ислам, К.А. Кутербеков, А.К. Азад

Жаңа легирленген перовскит түріндегі $SrFe_{0.6}Cu_{0.3}Mo_{0.1}O_{3-\delta}$ оксидінің құрылымдық және жылулық қасиеттерін зерттеу

Жұмыста жаңа перовскит түріндегі $SrFe_{0.6}Cu_{0.3}Mo_{0.1}O_{3-\delta}$ оксиді қаттыфазалық реакция әдісімен синтезделіп, нейтрондық ұнтақ дифракциясы (НҰД), сканерлеуші электрондық микроскопия (СЭМ) және жылулық талдау әдістері арқылы жан-жақты сипатталды. НҰД қолдану атомдық құрылымды дәл анықтауға және атомдық нөмірлері ұқсас катиондарды ажыратуға мүмкіндік берді. Ритвельд әдісі бойынша алынған нәтижелер *Pm*-3*m* (№ 221) кеңістік тобына жататын кубтық бірфазалы перовскит құрылымының қалыптасуын растады, ал тор параметрі $a = b = c = 3.8997(1)$ Å болды. СЭМ кескіндері біртекті элементтік таралуы бар жоғары кеуекті және өзара байланысқан микроқұрылымды көрсетті. Термогравиметриялық талдау (ТГА) 1000 °C дейін екі сатылы оттегі жоғалтуды көрсетті, бұл материалдың жоғары жылулық тұрақтылығын дәлелдейді. 900 °C температурасында өлшенген жылуөткізгіштік 1.986 $Вт \cdot м^{-1} \cdot К^{-1}$ шамасында болып, Cu және Mo бірлесіп легирлеу нәтижесінде фонондардың шашырауының артуымен және тордың бұзылуымен түсіндіріледі. Алынған нәтижелер B-позициясындағы бақыланатын легирлеу дефекттік химияны және жылу тасымалын тиімді реттейтінін көрсетті. $SrFe_{0.6}Cu_{0.3}Mo_{0.1}O_{3-\delta}$ жоғары температуралы энергия түрлендіргіштерінде, соның ішінде термоэлектрлік құрылғылар мен қаттыоксидті отын элементтерінде қолдануға перспективті материал болып табылады.

Кілт сөздер: перовскит типті оксид, нейтрондық ұнтақ дифракциясы, Ритвельд әдісі, қаттыфазалық синтез, сканерлеуші электрондық микроскопия, термогравиметриялық талдау, микроструктура, оттегінің қаттылығы, фонондардың шашырауы, жылуөткізгіштік

Ш. Афрозе, А.М. Кабышев, А.А. Аймаханова,
М.С. Реза, М.С. Ислам, К.А. Кутербеков, А.К. Азад

Исследование структурных и тепловых свойств нового легированного оксида перовскитного типа $SrFe_{0.6}Cu_{0.3}Mo_{0.1}O_{3-\delta}$

В данной работе оксид $SrFe_{0.6}Cu_{0.3}Mo_{0.1}O_{3-\delta}$ был синтезирован методом твёрдофазной реакции и охарактеризован с использованием нейтронной порошковой дифракции (НПД), сканирующей электронной микроскопии (СЭМ) и термического анализа. Нейтронная дифракция позволяет проводить детальный анализ сложных оксидов, особенно в случаях, когда атомы имеют близкие атомные номера. Уточнение по методу Ритвельда данных НПД подтвердило простую кубическую перовскитную структуру с пространственной группой *Pm*-3*m* (№ 221) и параметрами элементарной ячейки $a = b = c = 3.8997(1)$ Å. Результаты СЭМ показали высокопористую и взаимосвязанную микроструктуру, в то время как термогравиметрический анализ (ТГА) выявил двухступенчатую потерю кислорода до 1000 °C, что указывает на хорошую термическую стабильность материала. Измеренная теплопроводность составила 1.986 $Вт \cdot м^{-1} \cdot К^{-1}$ при 900 °C. Полученные результаты демонстрируют, что содопирование медью и молибденом эффективно регулирует дефекты кристаллической решётки и рассеяние фононов, что открывает перспективные возможности для разработки перовскитных оксидов с пониженной теплопроводностью для применения в области альтернативной энергетики, их высокой термомеханической совместимости, улучшенной проводимости и долговечности.

Ключевые слова: оксид перовскитного типа, нейтронная порошковая дифракция, метод Ритвельда, твёрдофазный синтез, сканирующая электронная микроскопия, термогравиметрический анализ, микроструктура, нестрогость по кислороду, рассеяние фононов, теплопроводность

Information about the authors

Shammya Afroze — Researcher of the Institute of Physical and Technical Sciences, L.N. Gumilyov Eurasian National University, Astana, Kazakhstan; Researcher of the Faculty of Integrated Technologies, Universiti Brunei Darussalam, Bandar Seri Begawan, Brunei; Researcher of the Department of Chemistry and Chemical Engineering, Chalmers University of Technology, Gothenburg, Sweden; e-mail: shammya111@gmail.com; Scopus ID: 57208761031; ORCID: https://orcid.org/0000-0002-8609-6001;

Kabyshev, Asset (*corresponding author*) — Teacher-Researcher of the Institute of Physical and Technical Sciences, L.N. Gumilyov Eurasian National University, Astana, Kazakhstan; e-mail: kabyshev_am_1@enu.kz; Scopus ID: 56177620700; ORCID: https://orcid.org/0000-0003-1472-4045

Aimakhanova, Ainur — PhD student of the Institute of Physical and Technical Sciences, L.N. Gumilyov Eurasian National University, Astana, Kazakhstan; e-mail: aimakhanova_aa@enu.kz.

MdSumon Reza — Researcher of the Faculty of Integrated Technologies, University Brunei Darussalam, Bandar Seri Begawan, Brunei; e-mail: sumonce@gmail.com; Scopus ID: 57208498300; ORCID: https://orcid.org/0000-0002-7451-8385;

MdSirajul Islam — Researcher of the Department of Civil Engineering, Bangladesh University of Engineering and Technology, Dhaka, Bangladesh; e-mail: mislam32@ncsu.eduж; ORCID: https://orcid.org/0009-0006-5365-6718

Kuterbekov, Kairat — Teacher-Researcher of the Institute of Physical and Technical Sciences, L.N. Gumilyov Eurasian National University, Astana, Kazakhstan; e-mail: kuterbekov_ka@enu.kz; Scopus ID: 6603440057; ORCID ID: https://orcid.org/0000-0001-5421-271X

Abul K. Azad — Professor, Faculty of Integrated Technologies, University Brunei Darussalam, Bandar Seri Begawan, Brunei; Scopus ID: 56962736700; https://orcid.org/0000-0001-9391-3463; e-mail: abul.azad@ubd.edu.bn.

Article

UDC 533.15:536.25

https://doi.org/10.31489/2026PH1/81-89

Received: 06.11.2025
Accepted: 21.01.2025

V.N. Kossov[1], S.A. Krasikov[1], M.K. Asembaeva[2]✉, E. Meirambekuly[2]

[1]*Abai Kazakh National Pedagogical University, Almaty, Kazakhstan;*
[2]*Al-Farabi Kazakh National University, Almaty, Kazakhstan*

Image of the Experimental 3D Concentration Field of the Separated Gas with Specified Thermophysical Properties under Conditions of Mechanical Equilibrium Instability in an Isothermal Ternary Mixture

Isothermal diffusion and convective mixing in a ternary He–Ar–N_2 mixture at varying pressures and initial compositions were examined experimentally by means of the two-flask method. The study was conducted under strictly controlled laboratory conditions to ensure precise, comparable, and reproducible results across all experiments. It was found that when the density decreases with height, the mechanical equilibrium of the mixture can be disturbed, causing gravitational flows and partial convection within the system. Anomalous transfer of the component with the greatest molecular mass was detected at particular pressures and starting compositions, pointing to the influence of supplementary convective processes beyond ordinary diffusion. When the experimental results were plotted in the phase space of the three variables — pressure, initial composition, and diffused component concentration — a pronounced wave-like iso-concentration surface emerged. This surface appeared in regions corresponding to well-developed convective flows. Its formation correlated with the highest intensity of partial component mixing, highlighting the combined influence of pressure, composition, and gravitational effects on the mixture's dynamic equilibrium. These findings provide insight into the interplay between diffusion and convection in multicomponent gas systems, revealing conditions under which gravitationally induced flows significantly alter component transport and overall mixture behavior.

Keywords: diffusion, instability, convection, pressure, initial composition, concentration

✉*Corresponding author*: Asembaeva, Mansiya, m.asembaeva@physics.kz

Introduction

Modern technologies for material production and the prediction of natural phenomena require a more accurate interpretation of heat and mass transfer processes in liquid and gaseous media. Complexities in the description of multicomponent systems are caused by the simultaneous influence of different heat and mass transfer mechanisms. The control of processes in such systems requires new knowledge about the specifics of combined mass transfer at different stages of mixing, especially in conditions where equilibrium is disturbed by gravitational convection [1, 2]. The generalizations presented in review studies [3, 4] on the investigation of non-isothermal mixing have shown that the emergence of different types of equilibrium instabilities is related to the complex interaction between temperature and concentration gradients. It was also noted that the transition of the studied system to a thermo-gravitational mixing regime can be realized within the framework of convective stability theory by determining the critical Rayleigh numbers that define the transition of the system from a convective state to a mixing regime. Researches of stability of equilibrium states of binary systems in non-isothermal conditions, carried out on the basis of methods presented in [1–4], have shown the existence of various specific features of thermal-concentration mixing, associated with the nature of boundary conditions, interface surfaces and the appearance of combined flows, and so on. These findings make it possible to systematically refine and apply the obtained information within the context of the studied problem. For example, the investigation of the mixing of binary mixtures of magnetic fluids in a non-uniform temperature field has shown that as a result of positive thermo-diffusion, density inversion regions are formed, which under the action of gravity destabilize the equilibrium of the system, causing the development of convective bursts [5, 6]. The peculiarity of this mixing regime is that the corresponding hydrodynamic currents manifest themselves in the so-called subcritical region, i.e., at Rayleigh numbers lower than the critical value that defines the transition between regimes, indicating a situation where, at the initial stage of mixing, the system exhibits a stable state of mechanical equilibrium.

A similar situation can occur in isothermal gas mixtures due to the diversity of diffusion mixing mechanisms. However, for binary mixtures, convective transfer arises within the traditional framework of Rayleigh–Taylor gravitational convection [7], which represents the mixing of a denser medium with a less dense one and corresponds to Rayleigh numbers exceeding the calculated critical value [8]. The opposite direction of the mixture's density gradient determines diffusive mixing [9], which is characterized by Rayleigh numbers significantly lower than the critical value that marks the onset of convection. Nevertheless, in ternary gas mixtures isothermal diffusion under certain conditions is capable of causing the appearance of analogs of convective bursts similar to those noted in [5, 6], with the subsequent development of concentration gravitational convection [9]. Despite the similarity of the effects observed in thermal and isoconcentration convection, the mechanisms responsible for the formation of inversion layers exhibit distinctive features. These differences are associated with the presence of multiple concentration gradients that give rise to specific diffusion regimes [10], which are absent in the thermal diffusion mixing described in [4–6]. One manifestation of such special diffusion regimes was reported in [11], where significant differences in the diffusion coefficients of the components lead to a nonlinear concentration distribution in a vertical channel, ultimately resulting in the inversion of the density gradient and the subsequent onset of isothermal gravitational convective flows. Several other features of diffusion mechanisms that cause concentration-driven gravitational convection are discussed in the review [12]. Among them, it is worth noting experimental results showing that the loss of system equilibrium stability leads to isothermal concentration gravitational convection accompanied by a synergistic increase in the rate of component mixing [9, 13]. In this case, the mixing intensity exhibits a nonlinear dependence on pressure, initial composition, and several other thermophysical parameters.

Thus, failure to take diffusion into account in multicomponent mass transfer leads to distortion in the description of concentration fields and their subsequent evolution. The need to take into account the appearance of gravitational convection in gas mixtures due to the violation of the mechanical equilibrium of the system will allow for a more accurate description of heat and mass transfer in multicomponent mixtures, which is not always done in diffusion experimental and computational-theoretical studies. This paper presents experimental results on the study of diffusion and the recording of convective currents caused by the disturbance of the equilibrium of a ternary mixture of helium, argon, and nitrogen in a wide range of concentrations and pressures and at a constant temperature. Based on the obtained experimental data, a quantitative assessment was made of the degree of mixing of the partial component fluxes in both the diffusive and combined regimes.

Materials and methods

Experiment

Experimental device and experimental procedure

Experimental studies were performed on a device that implements the two-flask method [14], upgraded to measure the partial concentrations of components not only in diffusion modes, but also in the field of convective transfer using flat and cylindrical channels with different geometric parameters [15]. The schematic representation of the measuring complex is reproduced in Figure 1.

Linear parameters and dimensions of the measuring device (diffusion cell) correspond to the following values: volume of the upper bulb $V_u = (185.0 \pm 0.5)\cdot 10^{-6}$ m^3; volume of the lower bulb $V_l = (186.0 \pm 0.5)\cdot 10^{-6}$ m^3; dimensions of the rectangular vertical channel a×b×L = $(30.00 \pm 0.05 \times 6.00 \pm 0.05 \times 165 \pm 0.05)\cdot 10^{-3}$ m (Figure 1*b*). In all measurements, the temperature was 298 K. Mixing time 300 s.

The features of isothermal mixing were studied by analyzing the concentration and baric dependences of the ternary system He (1) + Ar (2) – N_2 (3) at constant temperature. Table 1 presents the mutual diffusion coefficients as well as some thermophysical characteristics of the miscible components at normal pressure and temperature T = 298.0 K. In further discussion, we will assume that the numbers in parentheses after the chemical element determine its numbering in the system under study. The values given before the chemical elements of the mixture determine the initial composition in mole fractions. It should also be noted that in the pressure range of 0.1–2.0 MPa and temperature T = 298.0 K, the studied helium — argon — nitrogen mixture can be considered ideal for any initial compositions.

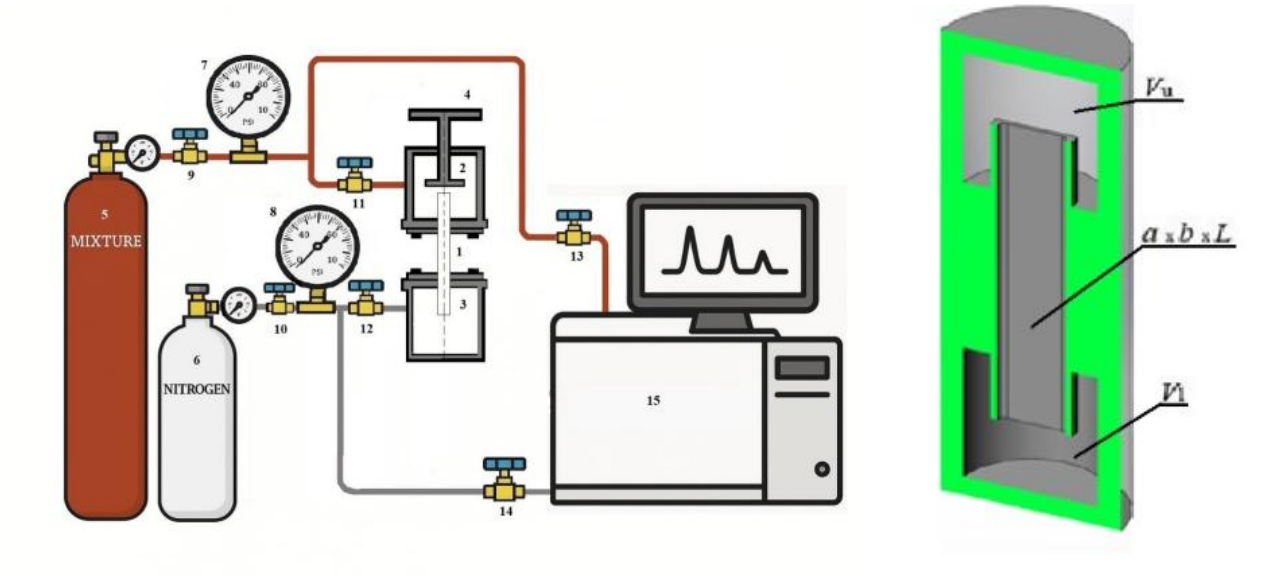

a) Experimental setup scheme *b)* Diffusion cell

Figure 1. Implementation of the two-column method

Table 1

Some thermophysical properties of the mixture components and coefficients of mutual diffusion of gases

Properties of gases [16]			
Gas	Molecular weight, 10^{-3} kg/mole	Density, kg/m^3	Viscosity, 10^{-5}Pa·s
Helium He	4.0026	0.16	1.997
Nitrogen N_2	28.0134	1.13828	1.775
Argon Ar	39.94	1.6	2.271

Interdiffusion coefficients of gases, $D_{ij}\cdot10^{-4}$ m^2/s [8, 16]		
$D_{\text{He-Ar}}$	$D_{\text{He-N}_2}$	$D_{\text{Ar-N}_2}$
0.745	0.621	0.230

At the initial stage of the experiment, aimed at studying both diffusive and convective separation of gas mixtures, the procedure of vacuumization of the internal volumes of the unit, including the main elements of the diffusion cell: the upper flask (2), the lower flask (3) and the connecting channel (1) is carried out. In the process of vacuumization the valve (4) remains closed. Further, the upper flask (2) is filled with a gas mixture of helium and argon from the cylinder (5) through open valves (9) and (11) with closed valve (13). The pressure of the mixture is brought to the experimental value and controlled by the manometer (7), after which the valves (9) and (11) are closed. The lower flask (3) is filled with nitrogen from the cylinder (6) through the open system of valves (10) and (12) with the valve (14) closed. The gas is supplied until the required pressure is reached, monitored by the manometer (8). When the filling of the lower flask is complete, valves (10) and (12) are closed. When the procedure of pressure equalization in flasks (2) and (3) is completed, valve (4) is opened and the process of multi-component mixing begins.

Experimental studies were carried out at pressures ranging from 0.15 to 2.55 MPa and temperature 298.0 K. The accuracy of temperature control was 0.1 K, pressure — 0.02 MPa. Determination of component concentrations was performed by gas chromatography with relative error not more than 1–3 %. Direct measurements were carried out for argon and nitrogen, and helium concentration was calculated from the condition of particle number conservation

$$\sum_{i=1}^{n} c_i = 1$$

where c_i is the concentration of the *i*-th component. To increase reliability, the results were averaged over several series of measurements under identical conditions. In all experiments, the upper flask of the diffusion cell contained a mixture of helium and argon, whereas the lower flask contained nitrogen.

The method of obtaining the concentration and baric dependence for isolated argon from experimental data

The intensity of diffusive and convective mixing in ternary gas mixtures was quantitatively evaluated by comparing experimental concentration data with values calculated from kinetic models assuming diffusion [8]. If the experimental and calculated data coincided within the experimental error, then this type of displacement was defined as diffusive. In the case of a discrepancy between them of tens or more percent, we can talk about the manifestation of convective transfer. By applying this approach at different pressures and initial compositions of the mixture and observing the constancy of all other experimental conditions in two-dimensional coordinates, it is possible to obtain baric or isoconcentration dependencies that characterize the corresponding type of mixing. By combining the characteristic dependencies and fixing the pressure, the initial mixture composition, and the concentration of the component governing the mixing behavior, an isoconcentration surface can be obtained in the coordinates of pressure, initial composition, and concentration of the transferred component.

Results and discussion

The main key parameter for understanding the dynamics of mixing and the kinetic transition from the diffusion regime to the convective one is to record the discrepancy between experimental and calculated concentrations at a certain value of the variable parameter (pressure, initial mixture composition). Figure 3 illustrates typical dependences of the concentrations of components diffused into the lower (helium and argon) and upper (nitrogen) flasks of the diffusion cell, respectively. Figure 2*a* shows that in the 0.68 He(1) + 0.32 Ar(2) – N_2(3) system, in the pressure range of 0.1–1.5 MPa, the coincidence of experimental and calculated using the Stefan-Maxwell equations [8] concentrations of components is recorded. This type of mixing can be characterized as diffusion. With an increase in the fraction of argon, the component with the highest molecular weight in the mixture, a dependence uncharacteristic of diffusion is observed: the mixing intensity increases with increasing pressure (Figure 2*b*).

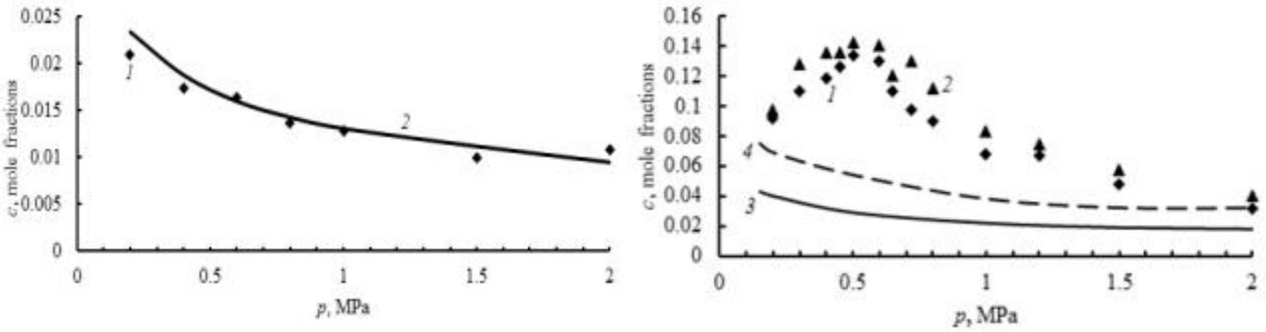

a) *b)*

Figure 2. Concentrations of components at different pressures in a vertical flat channel at T = 298.0 K: (*a*) — System 0.66 He + 0.34 Ar – N_2. Experimental points 1 — ♦ correspond to argon. Solid line 2 is calculated assuming diffusion for argon; (*b*) — System 0.43 He + 0.57 Ar – N_2. Experimental points ♦, ▲ correspond to: 1 — argon, 2 — nitrogen. Solid line 3 and dotted line 4 correspond to data calculated assuming diffusion for argon and nitrogen

For a number of compositions, pressure ranges are noted in which argon has a transport advantage over other components. This deviation from the classical diffusion concepts, assuming a weakening of mass transfer with increasing pressure, indicates the occurrence of convection due to the violation of mechanical equilibrium of the ternary system. The range of thermophysical parameters that determines the change in the "diffusion-convection" modes can be defined within the framework of stability theory [2], extended to the case of isothermal ternary gas mixtures [9]. However, it cannot be extended to describe combined mass transfer in the range of parameters significantly exceeding the boundary values for which nonlinear dependencies of the intensity of partial mixing of components on pressure are marked in Figure 3*b*. In this case, the condition of neutrality of convective perturbations [2] is violated, and the formalism of stability theory leads to significant quantitative discrepancies between experimental and calculated data.

Figure 3 shows the baric dependences of ternary mixtures with different argon contents in the mixture. Further experimental results are given for argon, since convective effects are most pronounced for argon. This allows us to avoid excessive detailing in the graphs and provide a more visual representation of the observed phenomena. The points correspond to experimental data for different argon contents in the initial composition of the mixture under study. Solid lines are approximation curves. According to the data obtained and the results published in [9, 13], an increase in the mixing intensity is observed as the content of the component with the highest molecular weight in the mixture increases. Visualization of this type of mixing carried out in [17] showed the presence of complex convective flows with structural formations. It should also be noted that for some convective regimes, the maximum mixing intensity is fixed.

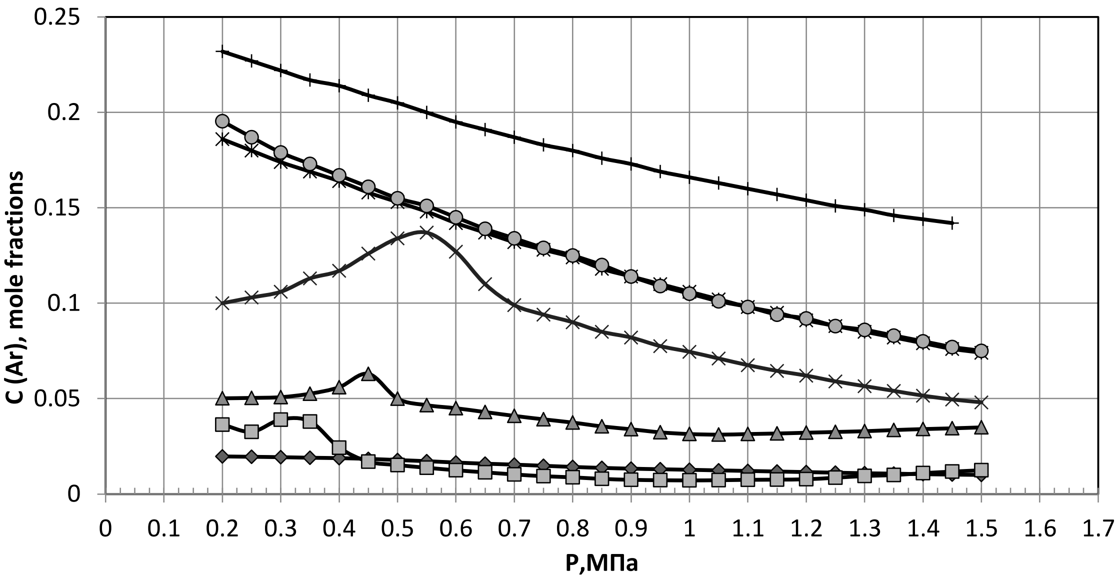

Figure 3. Baric dependencies of argon concentrations when mixing in the He + Ar – N_2 system with different initial compositions at T=298.0 K. The mixing time is τ = 300 s. The points determine the argon content at different pressures in the initial composition of the mixture expressed in mole fractions and correspond to: ◆ — 0.340; ■ — 0.420; ▲ — 0.516; ✕ — 0.570; * — 0.610; ● — 0.649; + — 0.697. Solid lines are approximations of experimental data

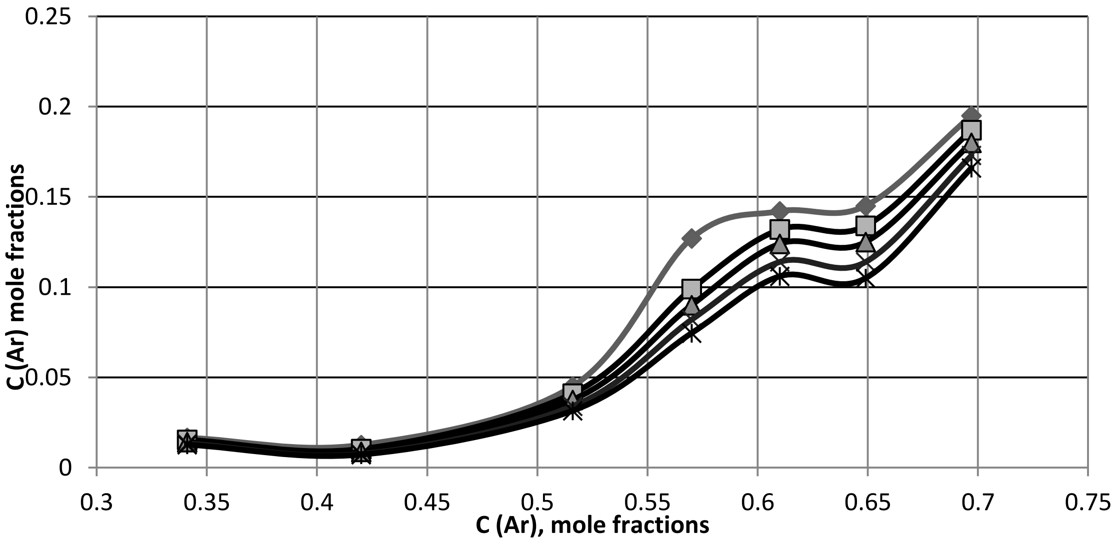

Figure 4. Argon concentrations when mixing in the He + Ar – N_2 system at a given pressure and various initial compositions of argon in a binary mixture with helium at T = 298.0 K. The mixing time is τ = 300 s. Points at different compositions are determined by a given pressure value in MPa and correspond to: ◆ — 0.60; ■ — 0.70; ▲ — 0.80; ✕ — 0.90; * — 1.00. Solid lines approximate the experimental data

Figure 4 shows the isoconcentration lines, a distinct nonlinear dependence is observed: with increasing content of the component with the highest molecular weight, the intensity of convective mixing increases significantly. Also, as for the previous case, there are characteristic areas of the initial composition (0.55–0.65 mole fractions of argon) at which a pronounced nonlinearity of the mixing intensity is recorded. In figures 3 and 4, a number of characteristic modes of mass transfer can be distinguished:

1 — at concentrations of 0.34 mole fractions of argon and below, we observe a purely diffusive mass transfer;

2 — at concentrations from 0.34 to 0.61 mole fractions of argon, determining the condition of mixture density decrease with height, convection and diffusion processes are observed in the system, generating separation of the mixture into heavy (in terms of density) and light components. At certain pressures and compositions, the preferential transfer of argon is observed, which is atypical for diffusion processes;

3 — at concentrations from 0.61 to 0.649 mole fraction of argon in the system under study, the condition of approximate parity of densities in the upper and lower parts of the channel is realized (approximate equality of the mixture density gradient to zero). Convective mixing modes continue in the system, but the signs of nonlinearity of partial mixing are not registered;

4 — at concentrations from 0.649 to 0.697 mole fractions of argon, the density gradient of the mixture changes sign, convective and diffusion processes separate the components of the mixture according to the mechanisms determined by Rayleigh–Taylor convection [7].

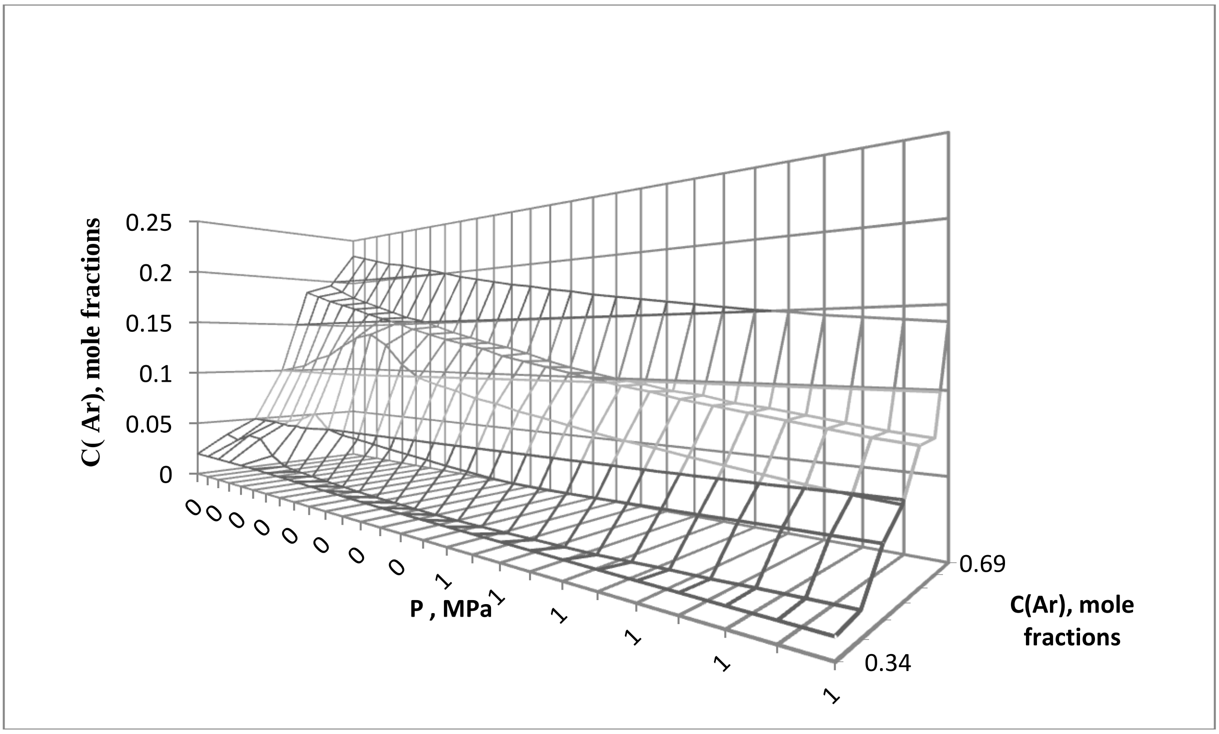

Figure 5. Three-dimensional field of argon concentrations in diffusion and convection modes in the He + Ar – N_2 system at T = 298.0 K and various initial compositions and pressures. Mixing time τ = 300 s

Combining the experimental data presented in Figures 3 and 4, in the coordinates “pressure – initial composition of the mixture – diffused concentration of the component” and supplementing them with approximation lines, it is possible to obtain an experimental surface characterizing the concentration field in both diffusion and convective modes. Figure 5 shows a three-dimensional argon concentration field in the diffusion regime (up to 0.34 mole fractions of argon in the initial composition of the mixture) and then a kinetic transition to a state of gravitational concentration convection with a pronounced nonlinear increase in the intensity of mass transfer in the pressure range (0.25–0.7) MPa and the initial composition (0.42–0.57) mole fractions. The experimental values presented allow us to speak about the occurrence of spatial concentration waves, which occur at certain ratios between mixture composition and pressure leads to preferential transfer of the most dense component (see Table 1), i.e. argon. Such resonant manifestations significantly turbulate convective flows created as a result of instability of the mechanical equilibrium, as can be judged by comparing the concentrations of argon during mixing at the diffusion–convection boundary and in areas where pronounced nonlinearities are present. Moreover, as can be seen from Figure 5, the resulting concentration wave can be controlled not only by pressure and temperature, but also by the influence of these two parameters simultaneously.

Conclusion

The conducted studies show that in multicomponent mixtures, the difference in the diffusion coefficients leads to a violation of the mechanical equilibrium of the mixture and the occurrence of gravitational concentration convection. Experimental study of the helium + argon – nitrogen system under the condition of decreasing density of the mixture with altitude has shown that in certain pressure ranges and initial composition of the mixture there is a nonlinear increase in the mixing intensity for the component with the highest molecular weight, which is not characteristic of classical diffusion. Representation of this effect in the phase space of the three measured quantities —"pressure – initial mixture composition – diffused component concentration" — showed a non-monotonic, isoconcentration wave-like surface that appears in the region of developed convective flows. Its emergence corresponds to the highest intensity of partial component mixing. Control of its displacement in the phase coordinates can be achieved either through individual variations in pressure and initial mixture composition or by simultaneous adjustment of these parameters.

Acknowledgments

Some of the results presented in this paper were obtained with the financial support of the Committee of Science of the Ministry of Science and Higher Education of the Republic of Kazakhstan under the project AR 23488139.

References

1 Nield D.A. Convection in Porous Media / D.A. Nield, A. Bejan. — Springer, 2006. — P. 654.

2 Gershuni G.Z. Convective stability of incompressible fluids / G.Z. Gershuni, E.M. Zhukhovitskii. — Keterpress, 1976. — P. 330.

3 Andreev V.K. Stability of non-isothermal fluids (review) / V.K. Andreev, V.B. Bekezhanova // Journal of Applied Mechanics and Technical Physics. — 2013. — Vol. 54, No. 2. — P. 171–184.

4 Рыжков И.И. Термодиффузия в смесях: уравнения, симметрии, решения и их устойчивость / И.И. Рыжков. — Новосибирск: Издательство СО РАН, 2013. — С. 201.

5 Glukhov A.F. Effect of particle thermophoresis on convection of magnetic fluids in narrow channels heated from below / A.F. Glukhov, A.S. Sidorov // Fluid Dynamics. — 2022. — Vol. 58, No. 1. — P. 45–56. DOI: 10.1134/S0015462822601863.

6 Glukhov A.F. Subcritical convection in colloids and liquid binary mixtures with positive thermal diffusion / A.F. Glukhov. // Bulletin of Perm University. Physics. — 2024. — No. 2. — P. 19–26. DOI: 10.17072/1994-3598-2024-2-19-26.

7 Wei T. Rayleigh–Taylor unstable condensing liquid layers with nonlinear effects of interfacial convection and diffusion of vapour / T. Wei, M. Zhang // J. Fluid Mech. — 2020. — Vol. 904. — A1. DOI: 10.1017/jfm.2020.572.

8 Bird R.B. Transport Phenomena (Revised Second ed.) / R.B. Bird, W.E. Stewart, E.N. Lightfoot. — John Wiley & Sons, 2007. — P. 895.

9 Kossov V. Diffusion and convective instability in multicomponent gas mixtures at different pressures / V. Kossov, S. Krasikov, O. Fedorenko // Eur. Phys. J. Spec. Top. — 2017. — Vol. 226. — P. 1177–1187. DOI: 10.1140/epjst/e2016-60201-1.

10 Kaminskii V.A. Special modes of three–component diffusion in gases / V.A. Kaminskii // Russ. J. Phys. Chem. — 2011. — Vol. 85. — P. 2203–2208. DOI: 10.1134/S0036024411120156.

11 Kosov V.N. Inversion of the density gradient and the diffusion "gate" in isothermal mixing of gases / V.N. Kosov, Y.I. Zhavrin, V.D. Seleznev // Technical Physics. — 1998. — Vol. 43, No. 5. — P. 488–492. DOI: 10.1134/1.1259026.

12 Kossov V. Diffusion Mechanisms of Convective Instability in Liquid and Gas Mixtures / V. Kossov, H. Altenbach // Journal of Applied Mathematics and Mechanics. — 2023. — Vol. 103, No. 1. DOI: 10.1002/zamm.202300801.

13 Kossov V. Peculiarities of mixing of some multicomponent gas mixtures containing carbon dioxide under the conditions of the diffusion–convection transition in vertical channels / V. Kossov, M. Asembaeva, O. Fedorenko, E. Meirambekuly // Heat Transfer Research. — 2025. — Vol. 56, No. 17. — P. 57–66.

14 Marrero T.R. Gaseous Diffusion Coefficients / T.R. Marrero, E.A. Mason // J. Phys. Chem. Ref. — 1972. — Vol. 1. — P. 3–118. DOI: 10.1063/1.3253094.

15 Asembaeva M.K. Effect of the Channel Inclination Angle on Convective Mixing Caused by Instability of Mechanical Equilibrium of Ternary Gas Mixture at Isothermal Diffusion / M.K. Asembaeva, V.N. Kosov, S.A. Krasikov, O.V. Fedorenko // Technical Physics Letters. — 2019. — Vol. 45, No. 11. — P. 1071–1074. DOI: 10.1134/S1063785019110038.

16 Vargaftik N.B. Handbook of Physical Properties of Liquids and Gases. Pure Substances and Mixtures / N.B. Vargaftik. — Springer, 2014.

17 Kossov V.N. Comparative study of evolution of structured flows at boundary of the regime change “diffusion–concentration convection” in isothermal multicomponent mixing in gases by techniques of visual and numerical analysis / V.N. Kossov, S.A. Krasikov, S.A. Belov, O.V. Fedorenko, M. Zhaneli // Bulletin of the University of Karaganda-Physic. — 2023. — Vol. 109, No. 1. — P. 49–58. DOI: 10.31489/2023PH1/49–58.

В.Н. Косов, С.А. Красиков, М.К. Асембаева, Е. Мейрамбекұлы

Изотермиялық үштік қоспадағы механикалық тепе-теңдік тұрақсыздығы жағдайында көрсетілген жылуфизикалық қасиеттері бар бөлінген газдың тәжірибелік 3D концентрация өрісінің кескіні

Изотермиялық диффузия және He–Ar–N_2 үштік газ қоспасындағы конвективтік араласу әртүрлі қысымдар мен бастапқы құрамдар кезінде тік жазық каналмен жалғанған екі колба әдісі арқылы эксперименттік түрде зерттелді. Зерттеулер 0,15-тен 2,55 МПа-ға дейінгі қысымдар диапазонында және 298,0 К температурада жүргізілді. Қоспа компоненттерінің концентрациялары газдық хроматография әдісімен анықталды. Белгілі бір шарттарда тәжірибе бірнеше рет қайталанып, өлшенген шамаларды орташа алу арқылы компоненттердің концентрацияларының нақты мәндері анықталды. Қоспаның тығыздығы биіктік бойынша азаятын жағдайларда компоненттердің диффузия коэффициенттерінің әртүрлі болуы жүйеде тығыздықтың стратификациясына әкелетіні көрсетілді. Бұл өз кезегінде механикалық тепе-теңдіктің тұрақтылығының бұзылуына себеп болып, әртүрлі қарқындылықтағы гравитациялық ағындардың пайда болуын туындатады. Эксперименттік түрде белгілі бір қысымдар мен құрамдар кезінде үштік жүйелерде қоспадағы молекулалық массасы ең үлкен компоненттің басым тасымалдануы байқалатыны анықталды. Мұндай араласу диффузияға тән емес. Тәжірибелік нәтижелерді «қысым — қоспаның бастапқы құрамы — диффузияланатын компоненттің концентрациясы» атты үш өлшенетін шама фазалық кеңістігінде ұсыну барысында толқын тәрізді изоконцентрациялық бет анықталды. Бұл бет дамыған конвективтік ағындарға сәйкес келетін қысым мен құрам аймақтарында пайда болады. Оның қалыптасуы молекулалық массасы ең үлкен компоненттің араласу қарқындылығының жоғары болуымен, сондай-ақ қысым мен құрамның қоспаның динамикалық тепе-теңдігіне әсерімен байланысты.

Кілт сөздер: диффузия, тұрақсыздық, конвекция, қысым, бастапқы құрамы, концентрация

В.Н. Косов, С.А. Красиков, М.К. Асембаева, Е. Мейрамбекулы

Изображение экспериментального 3D поля концентрации выделенного газа с заданными теплофизическими свойствами в условиях неустойчивости механического равновесия в изотермической тройной смеси

Изотермическая диффузия и конвективное перемешивание в тройной газовой смеси He–Ar–N_2 при различных давлениях и начальных составах были экспериментально исследованы методом двух колб, соединенных вертикальным плоским каналом. Исследования проводились в диапазоне давлений от 0,15 до 2,55 МПа и при температуре 298,0 К. Концентрации компонентов определялись методом газовой хроматографии. При заданных условиях опыт повторялся несколько раз, и путем усреднения измеряемых величин определялось конкретное значение концентрации компонентов. Показано, что при условиях, когда плотность смеси уменьшается с высотой, различие коэффициентов диффузии компонентов приводит к стратификации плотности в системе с последующим нарушением устойчивости механического равновесия, которое вызывает появление гравитационных потоков различной интенсивности. Экспериментально обнаружено, что при определенных давлениях и составах в тройных системах возникает приоритетный перенос компонента с наибольшим молекулярным весом в смеси. Такое смешения не типично для диффузии. При представлении опытных результатов в фазовом пространстве трёх измеряемых величин — «давление – начальный состав смеси – концентрация диффундирующего компонента» — была обнаружена волнообразная изоконцентрационная поверхность. Эта поверхность появляется в областях давления и состава, соответствующих развитым конвективным течениям. Её формирование связано с наибольшей интенсивностью перемешивания компонента с наибольшим молекулярным весом и влиянием давления и состава на динамическое равновесие смеси.

Ключевые слова: диффузия, нестабильность, конвекция, давление, исходный состав, концентрация

References

1 Nield, D.A., & Bejan, A. (2006). *Convection in porous media* (3rd ed.). Springer.

2 Gershuni, G.Z., & Zhukhovitskii, E.M. (1976). *Convective stability of incompressible fluids*. Keterpress.

3 Andreev, V.K., & Bekezhanova, V.B. (2013). Stability of non-isothermal fluids (review). *Journal of Applied Mechanics and Technical Physics, 54*(2), 171–184.

4 Ryzhkov, I.I. (2013). *Termodiffuziia v smesiakh: uravneniia, simmetrii, resheniia i ikh ustoichivost* [Thermodiffusion in mixtures: equations, symmetries, solutions, and their stability]. Novosibirsk: Izdatelstvo Sibirskogo Otdelenie Rossiiskoi Akademii Nauk [in Russian].

5 Glukhov, A.F., & Sidorov, A.S. (2022). Effect of particle thermophoresis on convection of magnetic fluids in narrow channels heated from below. *Fluid Dynamics, 58*(1), 45–56. https://doi.org/10.1134/S0015462822601863

6 Glukhov, A.F. (2024). Subcritical convection in colloids and liquid binary mixtures with positive thermal diffusion. *Bulletin of Perm University. Physics,* 2, 19–26. https://doi.org/10.17072/1994-3598-2024-2-19-26

7 Wei, T., & Zhang, M. (2020). Rayleigh–Taylor unstable condensing liquid layers with nonlinear effects of interfacial convection and diffusion of vapour. *Journal of Fluid Mechanics, 904*, A1. https://doi.org/10.1017/jfm.2020.572

8 Bird, R.B., Stewart, W.E., & Lightfoot, E.N. (2007). *Transport phenomena* (Revised 2nd ed.). John Wiley & Sons.

9 Kossov, V., Krasikov, S., & Fedorenko, O. (2017). Diffusion and convective instability in multicomponent gas mixtures at different pressures. *European Physical Journal Special Topics, 226*, 1177–1187. https://doi.org/10.1140/epjst/e2016-60201-1

10 Kaminskii, V.A. (2011). Special modes of three-component diffusion in gases. *Russian Journal of Physical Chemistry, 85*, 2203–2208. https://doi.org/10.1134/S0036024411120156

11 Kosov, V.N., Zhavrin, Y.I., & Seleznev, V.D. (1998). Inversion of the density gradient and the diffusion "gate" in isothermal mixing of gases. *Technical Physics, 43*(5), 488–492. https://doi.org/10.1134/1.1259026

12 Kossov, V., & Altenbach, H. (2023). Diffusion mechanisms of convective instability in liquid and gas mixtures. *Journal of Applied Mathematics and Mechanics, 103*(1). https://doi.org/10.1002/zamm.202300801

13 Kossov, V., Asembaeva, M., Fedorenko, O., & Meirambekuly, E. (2025). Peculiarities of mixing of some multicomponent gas mixtures containing carbon dioxide under the conditions of the diffusion–convection transition in vertical channels. *Heat Transfer Research, 56*(17), 57–66.

14 Marrero, T.R., & Mason, E.A. (1972). Gaseous diffusion coefficients. *Journal of Physical and Chemical Reference Data, 1*, 3–118. https://doi.org/10.1063/1.3253094

15 Asembaeva, M.K., Kosov, V.N., Krasikov, S.A., & Fedorenko, O.V. (2019). Effect of the channel inclination angle on convective mixing caused by instability of mechanical equilibrium of ternary gas mixture at isothermal diffusion. *Technical Physics Letters, 45*(11), 1071–1074. https://doi.org/10.1134/S1063785019110038

16 Vargaftik, N.B. (2014). *Handbook of physical properties of liquids and gases: Pure substances and mixtures* (5th ed.). Springer.

17 Kossov, V.N., Krasikov, S.A., Belov, S.A., Fedorenko, O.V., & Zhaneli, M. (2023). Comparative study of evolution of structured flows at boundary of the regime change "diffusion—concentration convection" in isothermal multicomponent mixing in gases by techniques of visual and numerical analysis. *Bulletin of the University of Karaganda-Physics, 109*(1), 49–58. https://doi.org/10.31489/2023PH1/49–58

Information about the authors

Kossov, Vladimir — Doctor of Physical and Mathematical Sciences, Professor, Academician of the National Academy of Sciences of the Republic of Kazakhstan, Academician of the National Academy of Sciences of the High School of RK, Head of the Physics Department, Physics Department, Abai Kazakh National Pedagogical University, Almaty, Kazakhstan; e-mail: kosov_vlad_nik@list.ru; ORCID ID: https://orcid.org/0000-0002-8001-1644

Krasikov, Sergei — Candidate of Technical Sciences, Leading Research Scientist, Physics Department, Abai Kazakh National Pedagogical University, Almaty, Kazakhstan; e-mail: sa.krassikov@mail.ru; ORCID ID: https://orcid.org/0000-0001-7202-7251

Asembaeva, Mansiya (*contact person*) — Candidate of Physical and Mathematical Sciences, Associate Professor, Department of Thermal Physics and Technical Physics, Al-Farabi Kazakh National University, Almaty, Kazakhstan; e-mail: m.asembaeva@physics.kz; ORCID ID: https://orcid.org/0000-0003-2022-3888

Meirambekuly, Esbol — PhD student, Department of Thermal Physics and Technical Physics, Al-Farabi Kazakh National University, Almaty, Kazakhstan; e-mail: basatar_94@mail.ru